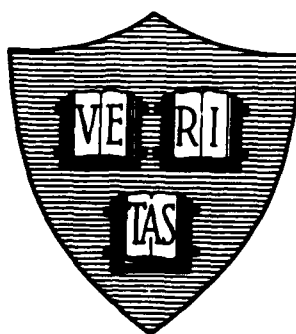


AD-A216 985

Office of Naval Research

Contract N00014-87-K-0511

**TUNNELING MICROSCOPY OF  
SUBMONOLAYER ADSORBATES ON SI(111)**



By

**Peter J. Bedrossian**

**October 1989**

**Technical Report No. 1**

RECEIVED  
OCT 19 1990  
as

This document has been approved for public release and sale; its distribution is unlimited. Reproduction in whole or in part is permitted by the U. S. Government.

**Division of Applied Sciences  
Harvard University, Cambridge, Massachusetts**

90 01 18 081

REPORT DOCUMENTATION PAGE		READ INSTRUCTIONS BEFORE COMPLETING FORM
1. REPORT NUMBER Technical Report No. 1	2. GOVT ACCESSION NO.	3. RECIPIENT'S CATALOG NUMBER
4. TITLE (and Subtitle) Tunneling Microscopy of Submonolayer Adsorbates on Si(111)		5. TYPE OF REPORT & PERIOD COVERED
7. AUTHOR(s) Peter John Bedrossian		6. PERFORMING ORG. REPORT NUMBER
9. PERFORMING ORGANIZATION NAME AND ADDRESS		8. CONTRACT OR GRANT NUMBER(s) N00014-87-K-0511
11. CONTROLLING OFFICE NAME AND ADDRESS Division of Applied Sciences Harvard University Cambridge, MA 02138		10. PROGRAM ELEMENT, PROJECT, TASK AREA & WORK UNIT NUMBERS
14. MONITORING AGENCY NAME & ADDRESS (if different from Controlling Office)		12. REPORT DATE October 1989
		13. NUMBER OF PAGES 221 pages
		15. SECURITY CLASS. (of this report) Unclassified
		16. DECLASSIFICATION/DOWNGRADING SCHEDULE
16. DISTRIBUTION STATEMENT (of this Report) Reproduction in whole or in part is permitted for any purpose of the United States Government. Approved for public release; distribution unlimited.		
17. DISTRIBUTION STATEMENT (of the abstract entered in Block 20, if different from Report)		
18. SUPPLEMENTARY NOTES		
19. KEY WORDS (Continue on reverse side if necessary and identify by block number) tunneling microscopy                      gallium chemisorption surface doping incommensuration boron		
20. ABSTRACT (Continue on reverse side if necessary and identify by block number) We report the first real-space observation of several new types of ordered surface structures induced by submonolayer gallium or boron adsorption on Si(111). Where surface doping concentrations can be controlled, we find that we can identify distinct electronic characteristics, spatially localized on the atomic scale, that reflect both average and local dopant distributions and binding configurations. The experiments make use of a scanning tunneling microscope which we have constructed for vacuum operation.		

(20. Abstract, cont.)

For each known, ordered phase of gallium adsorption, we employ multiple-phase-domain images to identify the respective adsorbate binding configurations. For low ( $<1/3$  monolayer, where  $1\text{ML} = 7.8 \times 10^{14}$  atoms/cm<sup>2</sup>) gallium coverage, this technique leads to the resolution of the long-standing question of the lateral gallium location in the  $\sqrt{3} \times \sqrt{3} R30^\circ$  lattice. At higher Ga coverage ( $<1\text{ML}$ ), we find a previously undetermined incommensurate structure incorporating large, internally ordered supercells that in turn form a lattice with discrete boundaries. This ordered Ga overlayer had previously been identified by diffraction but had not been imaged; indeed this work reports the first real-space observation of this incommensurate superlattice. Our results suggest a graphitelike silicon-gallium top layer that is weakly bonded to the lattice below and stabilized by a periodic array of misfit dislocations. Examination of the material's initial growth stages indicates the relative significance of competing microscopic interactions that lead to incommensuration in this system.

For boron adsorption, we find one ordered surface phase, a  $\sqrt{3} \times \sqrt{3} R30^\circ$  structure, which can accommodate boron concentrations from very low coverage up to  $1/3$  monolayer. Surprisingly, we find that a  $\sqrt{3} \times \sqrt{3} R30^\circ$  structure, composed almost entirely of Si adatoms on a Si outer layer, may be stabilized by boron doping in near-surface layers. Moreover, our results are consistent with a model in which boron atoms occupy a site underneath the adatom, contrasting the pattern of adatom occupation adopted by the other Group III elements on Si(111).

Local tunneling spectroscopy performed over the available range of boron concentration leads to the identification of distinct current-voltage characteristics with the presence or absence of the dopant at individual atomic sites. Under certain systematic conditions, we observe negative differential conductivity in the microscope's tunnel junction, and we identify spatially localized electronic characteristics that enable single atoms to act as isolated tunnel diodes together with the microscope's tunneling tip.

The qualitative corroboration of the results of recent surface energy and stress calculations by our structural and electronic observations suggests that the conceptual approaches behind these computations might eventually offer a substantial predictive capability.

Contract N00014-87-K-0511

By

**A-1**

# Technical Report No. 1

RECEIVED  
COPY  
INSPECTED

A-1

Division of Applied Sciences  
Harvard University • Cambridge, Massachusetts

## Abstract

We report the first real-space observation of several new types of ordered surface structures induced by submonolayer gallium or boron adsorption on Si(111). Where surface doping concentrations can be controlled, we find that we can identify distinct electronic characteristics, spatially localized on the atomic scale, that reflect both average and local dopant distributions and binding configurations. The experiments make use of a scanning tunneling microscope which we have constructed for vacuum operation.

For each known, ordered phase of gallium adsorption, we employ multiple- phase-domain images to identify the respective adsorbate binding configurations. For low ( $<1/3$  monolayer, where  $1\text{ML} = 7.8 \times 10^{14}$  atoms/cm<sup>2</sup>) gallium coverage, this technique leads to the resolution of the long-standing question of the lateral gallium location in the  $\sqrt{3} \times \sqrt{3} R30^\circ$  lattice. At higher Ga coverage ( $\approx 1\text{ML}$ ), we find a previously undetermined incommensurate structure incorporating large, internally ordered supercells that in turn form a lattice with discrete boundaries. This ordered Ga overlayer had previously been identified by diffraction but had not been imaged; indeed this work reports the first real-space observation of this incommensurate superlattice. Our results suggest a graphitelike silicon-gallium top layer that is weakly bonded to the lattice below and stabilized by a periodic array of misfit dislocations. Examination of the material's

initial growth stages indicates the relative significance of competing microscopic interactions that lead to incommensuration in this system.

For boron adsorption, we find one ordered surface phase, a  $\sqrt{3}\times\sqrt{3}R30^\circ$  structure, which can accommodate boron concentrations from very low coverage up to  $1/3$  monolayer. Surprisingly, we find that a  $\sqrt{3}\times\sqrt{3}R30^\circ$  structure, composed almost entirely of Si adatoms on a Si outer layer, may be stabilized by boron doping in near-surface layers. Moreover, our results are consistent with a model in which boron atoms occupy a site underneath the adatom, contrasting the pattern of adatom occupation adopted by the other Group III elements on Si(111).

Local tunneling spectroscopy performed over the available range of boron concentration leads to the identification of distinct current-voltage characteristics with the presence or absence of the dopant at individual atomic sites. Under certain systematic conditions, we observe negative differential conductivity in the microscope's tunnel junction, and we identify spatially localized electronic characteristics that enable single atoms to act as isolated tunnel diodes together with the microscope's tunneling tip.

The qualitative corroboration of the results of recent surface energy and stress calculations by our structural and electronic observations suggests that the conceptual approaches behind these computations might eventually offer a substantial predictive capability.

## Contents

Abstract .....	iii
Contents .....	v
List of Figures.....	vii
List of Tables.....	xvi
I. Introduction.....	1
II. Scanning Tunneling Microscope .....	8
II.1 Essential Theory .....	8
II.2 Apparatus .....	19
II.2.1 Mechanical Design .....	19
II.2.2 Vibration Isolation .....	26
II.3 Electronics and Data Acquisition .....	33
II.4 Vacuum Environment.....	51
II.5 General Operating Procedure .....	61
II.5.1 Preparation, characterization, and imaging.....	61
II.5.2 Tunneling Spectroscopy .....	76
III. Chemisorption on Si(111)--Background.....	78
III.1 Introduction.....	78
III.2 Surface Lattice Structures .....	79
III.3 Surface Band Structure .....	92
III.4 Group III Adatoms--Summary of Previous Work .....	97
IV. Gallium adsorption on Si(111).....	100
IV.1 Coverage below 1/3 ML.....	100
IV.1.1 Sample Preparation .....	100

IV.1.2 Registry from STM .....	104
IV.1.3 Highly inhomogeneous surfaces and electronic contributions .....	113
IV.2 Beyond 1/3 ML--Incommensuration and Superlattices .....	118
IV.2.1 Sample preparation.....	118
IV.2.2 Tunneling results .....	122
IV.2.3 A microscopic picture of incommensuration .....	138
V. Boron Adsorption.....	144
V.1 Preparation and imaging .....	144
V.2 Surface Structure .....	153
V.2.1 Observations .....	153
V.2.2 A picture of surface B doping .....	159
V.3 Local tunneling spectroscopy.....	165
V.3.1 Atom-resolved spectra and surface states .....	165
V.3.2 An atomic-scale tunnel diode.....	179
V.4 Synthesis.....	186
VI. Conclusions.....	190
VI.1 Summary.....	190
VI.2 Outlook .....	193
Appendix Chemical Sample Preparation .....	195
References .....	197
Acknowledgments .....	204



## List of Figures

Fig. 2.1	Schematic of a general STM apparatus, showing the relationships of the principal functionalities. ....	9
Fig. 2.2	Illustration of a one-dimensional tunneling barrier.....	10
Fig. 2.3	Graphical definition of conductivity measurements in tunneling spectroscopy. ....	14
Fig. 2.4	Sketch of the active parts of the STM.....	20
Fig. 2.5	Timing diagram for the walker, which provides the coarse tip positioning. ....	21
Fig. 2.6	Cross-sectional view of the STM as mounted in its operating position in the UHV chamber. ....	23
Fig. 2.7	External vibration isolation system.....	29
Fig. 2.8	Vibration spectra from a vertical geophone on the vacuum chamber, with (a) no vibration isolation, (b) the pistons on the air table raised .....	30
Fig. 2.9	Vibration spectra from (a) a vertical, and (b) a horizontal geophone seated on the vacuum chamber with the pistons floating and the pendulum released.....	31
Fig. 2.10	Spectral analysis of the tip current with vibration isolation.....	32
Fig. 2.11	Circuit diagram for the High Voltage Amplifiers. ....	34
Fig. 2.12	Circuit diagram for the Walker Control.....	36

Fig. 2.13	Circuit diagram for the Scan Driver.....	38
Fig. 2.14	Circuit diagram for the Preamplifier. ....	40
Fig. 2.15	Circuit diagram for the Tip Control/Feedback Subsystem. ....	42
Fig. 2.16	Circuit diagram for the Tip Control/Integrator Subsystem. ....	45
Fig. 2.17	Circuit diagram for the Tip Bias System. ....	46
Fig. 2.18	Schematic summary of the STM Data Acquisition and Control System. ....	48
Fig. 2.19	Cross section of the vacuum chamber, showing equipment for surface preparation and characterization....	52
Fig. 2.20	Internal parts of the oven used for gallium deposition.....	55
Fig. 2.21	Side view of the sample manipulator.....	56
Fig. 2.22	Schematic summary of the Retarding Field Auger system.....	58
Fig. 2.23	Circuit diagram for the Auger Sweep Drive. ....	59
Fig. 2.24	Retarding field Auger spectrum of a Si(111) sample, acquired immediately after a bakeout and 600°C outgassing. ....	63
Fig. 2.25	Retarding field Auger spectrum of a Si(111)7x7 surface following a 1000°C annealing. The crystal had previously been Shiraki-etched.....	64
Fig. 2.26	Retarding field Auger spectrum of an unreconstructed Si(111) surface following 8 min. of Ne ion sputtering at 1keV.....	65

Fig. 2.27	Retarding field Auger spectrum of a Si(111)7x7 surface, following a full sputtering and annealing cycle.....	66
Fig. 2.28	130x130Å tunneling image showing the adatoms of the 7x7 reconstruction of clean Si(111). Tip bias = -2.0V, 1nA. ....	69
Fig. 2.29	A section of the 7x7 reconstruction, acquired at +1.8V tip bias and 1nA. ....	70
Fig. 2.30	A single atomic step in the Si(111)7x7 reconstruction, used to calibrate the vertical tip displacement. The step height is identical to the bulk (111) planar spacing, or 3.2Å.....	71
Fig. 2.31	Moiré effect in a 100x100Å, multiple tip image of the 7x7 reconstruction. Tip bias = -1.4V, 1nA.....	72
Fig. 2.32	As fig. 2.31, but with tip bias = +1.5V.....	73
Fig. 2.33	Model for a multiple-tip image from the superposition of two fully symmetric adatom images. ....	74
Fig. 2.34	The boundary between single- and double-tip regions occurs near an atomic step. ....	75
Fig. 2.35	Tunneling spectrum from the Si(111)7x7 surface.....	77
Fig. 3.1	DAS model for a unit cell in the 7x7 reconstruction.....	80
Fig. 3.2	(Top) Diagram of the outer double layer of an unreconstructed, 1x1 termination, with a 1x1 unit cell outlined. (Center) $\sqrt{3}\times\sqrt{3}$ R30° structure with adatoms occupying the T4 site. (Bottom) As previous case, but with adatoms occupying the H3 binding site.....	83

Fig. 3.3	Topology of Ga adatoms in the T4 site in $\sqrt{3}\times\sqrt{3}R30^\circ$ surface structures. (a) Unrelaxed, and (b) relaxed coordinates. ....	91
Fig. 3.4	Measured and calculated surface bands for Si(111)- $\sqrt{3}\times\sqrt{3}R30^\circ$ -Al, Si(111)- $\sqrt{3}\times\sqrt{3}R30^\circ$ -Ga, Si(111)- $\sqrt{3}\times\sqrt{3}R30^\circ$ -In, and Si(111)-7x7. ....	94
Fig. 4.1	Tunneling image of Si(111)- $\sqrt{3}\times\sqrt{3}R30^\circ$ -Ga, showing adatoms spaced 6.7Å apart. Tip bias = -1.4V, 1nA. ....	101
Fig. 4.2	Reflectivity and fluorescence yield for Ga on Si(111)- $\sqrt{3}\times\sqrt{3}R30^\circ$ , from X-ray standing wave interferometry.....	103
Fig. 4.3	STM image showing a boundary between domains of 7x7 and $\sqrt{3}\times\sqrt{3}R30^\circ$ structure. The line indicates the path of a corrugation trace. Tip bias = -1.14V, 1nA.....	107
Fig. 4.4	Corrugation trace representing tip height vs. lateral distance, along the line in fig. 4.3 spanning the 7x7- $\sqrt{3}\times\sqrt{3}R30^\circ$ interface, demonstrating T4 adatom occupation.....	108
Fig. 4.5	Alternate models for the adatom binding configuration in fig. 4.3.....	109
Fig. 4.6	STM image showing a 5x5- $\sqrt{3}\times\sqrt{3}R30^\circ$ interface. Tip bias = -1.6V, 500pA.....	110
Fig. 4.7	Corrugation trace along the 5x5- $\sqrt{3}\times\sqrt{3}R30^\circ$ interface in fig. 4.7.....	111
Fig. 4.8	Model for the 5x5- $\sqrt{3}\times\sqrt{3}R30^\circ$ interface in the Si(111)-Ga surface of fig. 4.6.....	112

Fig. 4.9	STM image of the 7x7 reconstruction following light deposition of Ga. The arrow indicates a dark, minority species incorporated into the surface lattice. Tip bias = -1.1V, 1nA. ....	114
Fig. 4.10	Top--STM images of Si(111) $\sqrt{3}\times\sqrt{3}$ R30°-Ga at -1V tip bias (left) and -1.5V (right), showing a reversal of adatom shading. Bottom--STM images of Si(111) $\sqrt{3}\times\sqrt{3}$ R30°-Ga at +1V (left) and -0.8V (right), showing consistent shading at low tip bias .....	116
Fig. 4.11	Retarding field Auger spectrum of Si(111) $\sqrt{3}\times\sqrt{3}$ R30°-Ga.....	120
Fig. 4.12	Retarding field Auger spectrum of the incommensurate Ga overlayer. ....	121
Fig. 4.13	470x400Å STM image of the Ga-induced overlayer characteristic of $\approx 0.75$ ML Ga coverage. Tip bias = -3.3V, 800pA.....	123
Fig. 4.14	A portion of the region in the previous figure emphasizing the steps of height 3.2Å.....	125
Fig. 4.15	200x200Å STM image of a Ga-induced overlayer surface, showing a more irregular pattern of supercells than in fig. 4.13. Tip bias = -3.1V, 500pA.A. ....	126
Fig. 4.16	200x200Å STM image showing regions of (a) 7x7, (b) $\sqrt{3}\times\sqrt{3}$ R30°-Ga, (c) nucleation sites, and (d) islands of superlattice material. Tip bias = -1.5V, 1nA.....	128
Fig. 4.17	A picture for the gallium nucleation observed in fig. 4.16.....	129

Fig. 4.18	100x100Å STM image showing a portion of fig. 4.16 in greater detail. The atomic-level structure of the supercells is evident.....	131
Fig. 4.19	Corrugation trace within one supercell in fig. 4.18.....	132
Fig. 4.20	400x400Å STM image following partial Ga desorption from a surface of the type in fig. 4.13. Regions of $\sqrt{3}\times\sqrt{3}R30^\circ$ periodicity form at terrace edges. Tip bias = -2.5V, 1nA. ....	134
Fig. 4.21	100x100Å STM image showing a $\sqrt{3}\times\sqrt{3}R30^\circ$ region at a step edge in greater detail. Tip bias = -2.6V, 1nA.....	135
Fig. 4.22	400x400Å STM image showing a droplet on Si(111) following heavy Ga deposition. Tip bias = +5V, 800pA. ....	136
Fig. 4.23	Reflectivity and fluorescence yield versus angle for the Ga overlayer on Si(111), from X-ray standing-wave interferometry. (Ze88).....	137
Fig. 4.24	Model for the gallium overlayer on Si(111), showing the incommensurate relationship between the overlayer and substrate periodicities.....	140
Fig. 5.1	(Top) 80x60Å STM image of Si(111) $\sqrt{3}\times\sqrt{3}R30^\circ$ -B prepared by annealing heavily B-doped Si(111). Tip bias = -1.25V, 1nA. (Bottom) STM images acquired at +1.1V (left) and -1.4V (right) tip bias, showing the constancy of the relative shading of the two types of adatom sites. ....	145

Fig. 5.2	100x100Å STM image of a surface prepared by sputtering boron onto clean, As-doped Si(111). Tip bias = -2.5V, 1nA.....	147
Fig. 5.3	100x100Å STM image of a surface prepared by evaporating Si onto a B-terminated $\sqrt{3}\times\sqrt{3}$ R30° surface and annealing briefly. Tip bias = -1.0V, 1nA. ....	148
Fig. 5.4	Retarding field Auger spectrum of a surface of the type in fig. 5.1.....	150
Fig. 5.5	Retarding field Auger spectrum of a surface of the type in fig. 5.2.....	151
Fig. 5.6	Retarding field Auger spectrum of a surface of the type in fig. 5.3.....	152
Fig. 5.7	100x100Å STM image showing an interface between 7x7 and $\sqrt{3}\times\sqrt{3}$ R30° domains, where B has been deposited by sputtering. Tip bias = -1.3V, 1nA. ....	154
Fig. 5.8	Corrugation trace across the line in fig. 5.7 spanning the interface between 7x7 and $\sqrt{3}\times\sqrt{3}$ R30° regions. ....	155
Fig. 5.9	Model for the interface in fig. 5.7, showing the adatom registry.....	156
Fig. 5.10	STM image of a region with both 7x7 and 5x5 reconstruction. The larger unit cell indicated corresponds to the former structure. The surface was prepared by annealing a heavily B-doped Si(111) crystal partially. ....	158
Fig. 5.11	Corrugation trace along the long diagonal of $\sqrt{3}\times\sqrt{3}$ R30° unit cells of a B-terminated Si(111)	

	surface, demonstrating the mirror symmetry of the unit cell. ....	160
Fig. 5.12	Two alternative sites for boron occupation consistent with the full symmetries of both the $\sqrt{3}\times\sqrt{3}$ R30° LEED pattern and the STM images. One is strongly favored theoretically. ....	161
Fig. 5.13	Unrelaxed topology for boron substitution in the B5 position .....	162
Fig. 5.14	80x80Å topographic image (left) and dI/dV image (right) showing the effect of an asymmetric tip on conductivity measurements. The arrows indicate a 7 o'clock shadow near bright adatom sites resulting from an asymmetric tip. Tip bias = -1.4V, 1nA. ....	166
Fig. 5.15	Tunneling spectra recorded over (a) bright, B-free, and (b) dark, B-occupied sites on Si(111) $\sqrt{3}\times\sqrt{3}$ R30°-B. ....	169
Fig. 5.16	40x40Å STM topographic image (left) and dI/dV image (right) recorded at -1.5V tip bias and 1nA. ....	171
Fig. 5.17	Line cuts from dI/dV images at -1.4V and -1.7V tip bias, distinguishing topographic and electronic contributions. ....	173
Fig. 5.18	Energy bands for Si(111) $\sqrt{3}\times\sqrt{3}$ R30°-B from photoemission and inverse photoemission.....	177
Fig. 5.19	Tunneling spectra recorded over (a) bright and (b) dark sites on a predominantly bright-adatom covered Si(111) $\sqrt{3}\times\sqrt{3}$ R30° surface, as in fig. 5.3 .....	178



Fig. 5.20	Tunneling spectra recorded over isolated and contiguous B-free sites, showing a transition to negative differential conductivity.....	181
Fig. 5.21	STM topographic image (left) and dI/dV image (right) showing regions of negative differential conductivity (shaded solid white) at -1.4V tip bias.....	182
Fig. 5.22	Tunnel junction I-V characteristics with the tip over different types of atomic sites, showing negative differential conductivity over certain B-free sites. ....	183
Fig. 5.23	Principle of operation of devices that exhibit negative differential conductivity. ....	185

## List of Tables

Table 3.1	Some results of LDA total energy calculations for clean Si(111) .....	88
Table 3.2	Calculated stresses $\sigma_{ij}$ for adsorbed Si(111) surfaces.....	89
Table 3.3	Column III of the periodic chart, with induced Si(111) $\sqrt{3} \times \sqrt{3}$ R30° surfaces.....	98



## **I. Introduction**

Since the discovery of the of the  $7\times 7$  reconstruction of the clean Si(111) surface in 1963 by low-energy electron diffraction (LEED), (La63) a rich variety of novel forms of matter has been found to reside at semiconductor surfaces and interfaces. In the ensuing years, the detection of new structures by LEED has been supplemented by the development of a number of new techniques for the preparation and characterization of atomically clean surfaces. Thus, the emergence of the currently accepted, microscopic model for the  $7\times 7$  reconstruction in 1985 represented a synthesis of contributions from a number of experimental and theoretical efforts. (Ta85)

The time scale alone for the structural determination of the clean Si(111) surface indicated above suggests the enormous challenge of understanding clean, self-terminated semiconductor surfaces. Even greater rewards should accompany the study of impurity-terminated surfaces, where broader possibilities for the control of electronic, chemical, or mechanical properties may be expected. The deeper complexity of adsorbed over clean systems demands that the accumulated repertoire of experimental tools now be brought to bear on their characterization.

The scanning tunneling microscope (STM) has found a special niche within this continually expanding array of tools. The steady development

of imaging techniques with vacuum tunneling since the early work of Young and collaborators, (Yo71) along with improvements in vacuum technology and vibration isolation, culminated in reports of atomic resolution imaging on Si(111) by Binnig, et. al. in 1983. (Bi83) Among experimental tools that make use of wave generation and detection, the STM uniquely probes the local decaying waves at a surface, rather than traveling plane waves. Precise information in the latter form necessarily reveals spatially averaged quantities; any tool that identifies individual atomic sites is therefore a useful complement to traditional techniques. The special role of STM in providing structural and electronic information unattainable by other means has been demonstrated amply for the case of clean Si(111). (Go86, Tr86) For locally inhomogeneous and adsorbate-covered surfaces, spatially localized data may be indispensable.

The present study demonstrates novel applications of the STM in the first atomic-scale examination and determination of several new surface structures, and their associated electronic consequences, induced by submonolayer adsorption of two representative elements, gallium and boron, on the Si(111). These two species present intriguing contrasts, despite their chemical similarities. Elemental Ga and B are both trivalent and are both found in the same column of the periodic table. At  $1/3$  ML coverage on Si(111), both induce the identical  $\sqrt{3} \times \sqrt{3} R30^\circ$  diffraction pattern. (Ka87, Ka88, Hi88)

Despite these common characteristics, further examination reveals startling differences in the adsorption behaviors of these two elements on Si(111). For example, above  $1/3$  monolayer coverage, the gallium-

terminated surface undergoes a transition to an incommensurate phase, which apparently saturates near 1 ML. (Ot85) No analogous phase has been identified for boron adsorption. Even within the  $\sqrt{3}\times\sqrt{3}R30^\circ$  structure, the boron-terminated surface is stable to both prolonged annealing above 1000°C and epitaxial silicon growth, whereas the gallium-terminated surface is disrupted immediately by more moderate temperatures or epitaxy. (He89)

We shall demonstrate that it is now possible to understand the origins of these and other fundamental, macroscopic, physical properties with a determination of surface crystal structure at the atomic scale. In fact, one of the principal undertakings of this work is just such a determination for each ordered phase induced on Si(111) by these adsorbates. By examining inhomogeneous surfaces, we also infer the adsorbate-substrate binding configurations of the observed materials. In each case, it will be shown that the position of the impurity species can be determined by STM along with one additional tool. While the present work primarily concerns the role of STM, the indispensable role of additional tools is emphasized, and their contributions will be identified when appropriate.

Each structure investigated here was previously identified by electron diffraction, but in no case was the structure determined completely by this method alone. For the simple  $\sqrt{3}\times\sqrt{3}R30^\circ$  lattices, the symmetry of the diffraction pattern constrained the structural possibilities to a few, identifiable models. The difficulty of extracting a real-space structure from electron diffraction alone is underscored by the absence, prior to our STM experiments, of any model that accounted for the incommensurate

diffraction patterns associated with the gallium overlayer. The STM reveals the microscopic periodicities within this surface and is therefore an essential analytical tool for the incommensurate system.

Surface structure determination has recently been approached by new, computationally-intensive theoretical methods which predict minimum-energy configurations and total stresses for simple reconstructions and terminations. (Va87b, Pa89) The experimental work therefore also provides an evaluation of the predictive power of these methods. While numerical energies and stresses cannot be verified quantitatively here, we shall find that the experimentally observed structures in each case confirm qualitative trends predicted theoretically.

A full exploitation of the power of local measurements should transcend identification of microscopic origins for macroscopic observables. A second class of observations reported here therefore involves the measurement of local properties that may not result in any clear macroscopic manifestation at all. It has already been demonstrated by STM, for example, that a surface may be prepared to hold many reconstructions, each of such short spatial extent that none assumes sufficient coherence to reveal itself in a macroscopic diffraction pattern. (Be86) On a still smaller scale, tunneling I-V characteristics have identified position-dependent energy band characteristics within one unit cell of clean Si(111). (Be85c, Tr86) Proceeding in this spirit, we demonstrate in this work the distinguishability and assignment of two types of randomly distributed atomic sites on one surface according to the presence or absence of an impurity atom at a specific site.

A recent examination of an aluminum-terminated Si(111) surface revealed distinct tunneling I-V characteristics of individual unit cells according to the presence of an impurity in a particular cell. (Ha88a-c) In attempting to localize conductance characteristics still further, we find that we must first define the measurements as precisely as possible. We can then identify a distinct spectral "fingerprint" for each type of atomic site. Under carefully prescribed conditions, we may identify certain spectral characteristics as manifestations of localized surface states. The random distribution of impurity atoms and associated surface states could not otherwise be detected by a diffraction technique.

With the capability of detecting random impurity locations established, we investigate next the possibility of deliberate modification of surface structure, with the aim of controlling measurable microscopic properties. We have found that a particular reconstruction of Si(111) admits alloying of boron with silicon over a wide range of relative concentrations, and is therefore a suitable candidate for such investigations. Accordingly, we have followed both the surface impurity distribution and associated local tunneling electronic characteristics over the available ranges of both the average concentration and local distribution of boron. Such a procedure reveals a strong interdependence of structural and electronic properties at the microscopic scale, to an extent heretofore unanticipated. For example, we find that a large, subsurface concentration of boron can stabilize an otherwise unfavorable  $\sqrt{3}\times\sqrt{3}R30^\circ$  structure of Si atoms on a Si double-layer.



The practical exploitation of semiconductor surfaces at the atomic level will surely follow refinements in techniques for measurement and structural control at that level. The present work, with its primary emphasis on physical foundations, necessarily deals with such abstractions as surface states and stress. In order to indicate how these constructs may ultimately be translated into more concrete, and one day useful, parameters, we close by demonstrating how a synthesis of observations leads to the realization of a tunnel diode of atomic dimension.

This work is organized in six chapters. Chapter II opens by presenting those aspects of the formal description of tunneling microscopy which will be required for subsequent data analysis. Because the assembly of the STM and associated hardware, to which the author had the special privilege of contributing from the outset, was undertaken at Harvard for these experiments, the details of the instrument and the control electronics also appear in Chapter II. The exploitation of the STM to the ends set forth above requires the integration of the microscope in an ultra-high vacuum (UHV) environment along with facilities for clean sample preparation, for deposition of impurities on clean surfaces, and for characterization of such surfaces prior to examination. The use of each of these ancillary tools will be discussed following the details of the construction and operation of the STM. Chapter II closes with a description of the operation of the STM by way of an example, the preparation and imaging of the  $7\times 7$  reconstruction of clean Si(111).

The remainder of the text treats particular systems. Chapter III outlines the theoretical and experimental status of trivalent metal adsorption

on Si(111) that existed prior to our experiments. Chapters IV and V present our own investigations of the gallium- and boron-terminated systems, respectively. A summary and outlook appear in the final chapter.

The crystallographic notation in the present work follows the convention of a number of elementary texts. (Ki86)

## II. Scanning Tunneling Microscope

### II.1 Essential Theory

A schematic illustration of a generalized STM apparatus is shown in Fig. 2.1. Each of the experiments described below utilizes the tunneling microscope in the "constant-current" mode, in which a finely sharpened tungsten needle, the "tip," is positioned close enough to a surface that a tunneling current of the order of 1nA occurs with a bias of 100mV-3V applied to the tip. The current is measured from the sample, which is held at a virtual ground. All tip displacements are accomplished by piezoelectric transducers. As the tip is rastered along the surface (x and y motion in the figure), a feedback network adjusts the vertical position of the tip (z motion) in order to maintain a constant tunneling current. The topographic image then consists of a record of the tip height as a function of lateral tip position.

The sensitivity of the STM to individual atoms in the surface layer of a crystal arises in large part from the exponential drop of tunneling current with distance  $s$ , roughly approximated as

$$I \propto \exp(-2s\hbar^{-1}\sqrt{2m\phi}). \quad (2.1)$$

For a sample work function  $\phi$  of 4eV, eqn. 2.1 suggests that the tunnel current falls by an order of magnitude for each 1Å change in

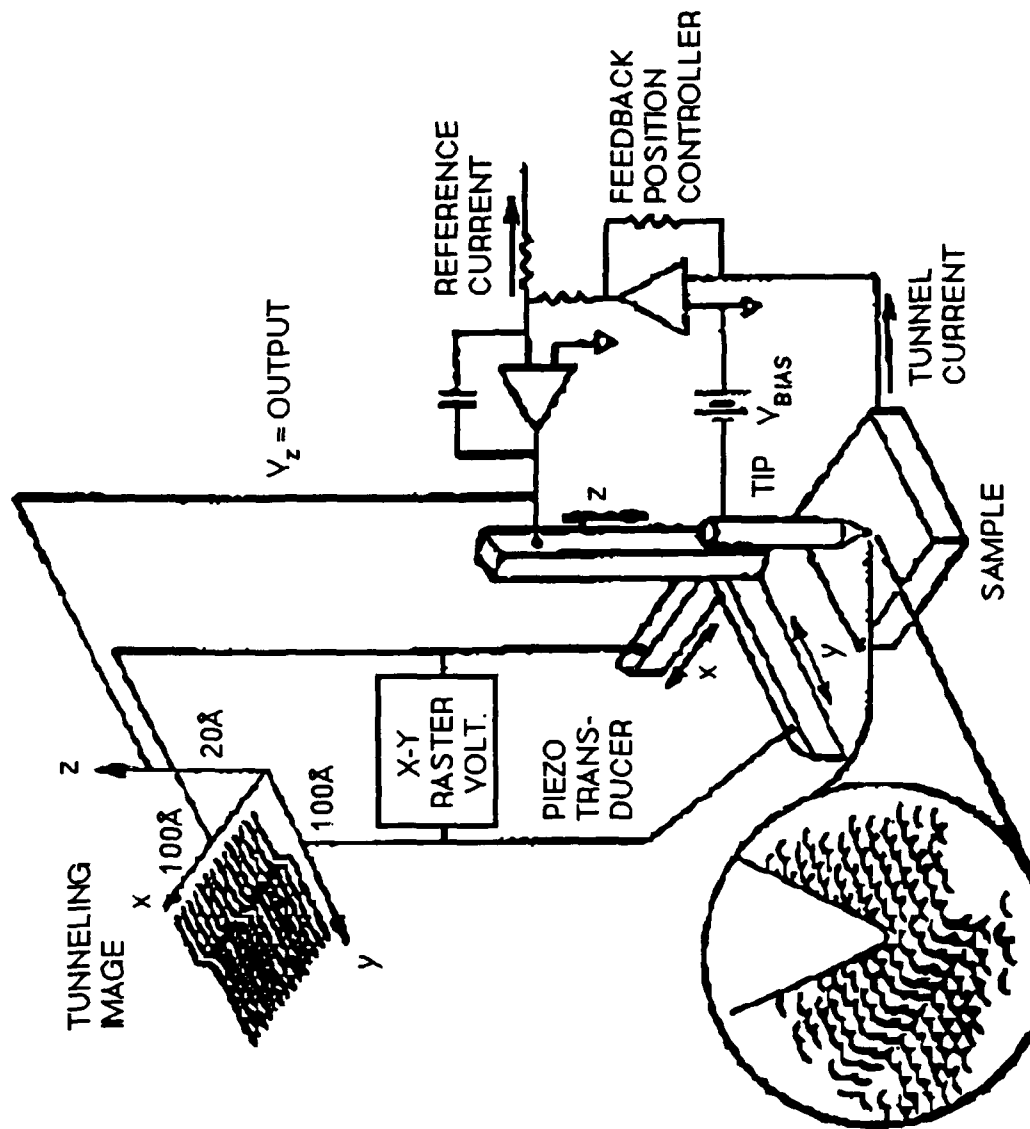


Fig. 2.1: Schematic of a general STM apparatus, showing the relationships of the principal functionalities. (After Go86)

## Tunneling Barriers and Spectroscopy

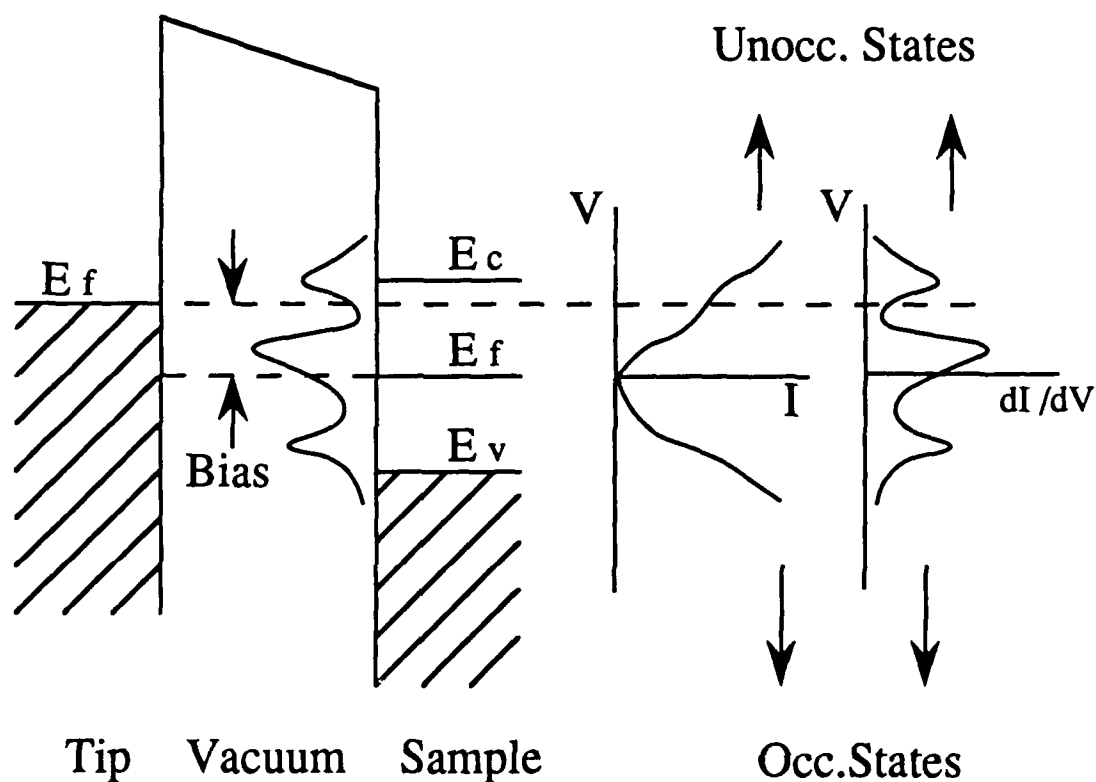


Fig. 2.2: Illustration of a one-dimensional tunneling barrier for the case of negative tip bias. An idealized surface state dispersion is shown on the sample, while the tip is treated as a fermi gas. As the tip bias passes through a surface state, an enhancement is expected in the junction's I-V characteristic, with a corresponding feature in the  $dI/dV$  spectrum.

distance. The tunneling current is then generally dominated by contributions from a single tip atom and the nearest surface atom. Yet this picture is inadequate in the regime of angström-scale corrugations probed by the STM, for the identification of a distance applicable in eqn. 2.1 is complicated by the tunneling contributions of various states near the fermi levels of both electrodes, each with its own spatial structure. Thus, while the surface structures imaged by STM can be identified with particular periodicities observed in LEED, the detailed interpretation of the corrugations in such images may require some understanding of the surface band structure.

The microscopic theory of tunneling (Ba61) is symmetric in surface and tip wavefunctions; therefore the tunneling images must reflect contributions from both. However, it has been convenient and customary in work that employs a metallic tunneling tip and semiconducting sample, as in the present study, to approximate the tip band structure as that of a fermi gas. Tunneling images at negative tip bias are then interpreted to reflect contributions from unoccupied sample states up to the bias voltage; likewise, images acquired at positive tip bias are assumed to reflect contributions from tunneling channels from the bias voltage up to the surface fermi level. (See fig. 2.2.) More thorough discussions of tunneling applications and formalism are found in a number of reviews. (Ha87, Ku89)

Because of the the dominant contribution of the first atomic layer in vacuum tunneling, the surface states associated with the reconstruction under examination are assumed take part in the tunneling process. Just as bulk bands arise through hybridization and broadening of atomic orbitals, bands are formed at a semiconductor surface from dangling bonds, but the bond hybridizations, and hence the band dispersions, naturally depend on

the topology of the reconstruction. That such states may generally fall in the band gap is clear at least in the case of nearly free electron (NFE) levels, for the NFE equations admit alternating bands of periodic and decaying solutions. While the latter are forbidden in the bulk by translational symmetry considerations, wavefunctions that decay into the vacuum are valid solutions at a crystal surface. Similarly, one may argue on general grounds that the energies of tight-binding-derived surface states may lie between bulk bands. (Za88) The proximity of these surface states to the fermi level underlies their dominant contribution to tunneling images. We note that these electronic levels are different from those normally probed by surface analysis tools such as Auger and ESCA, which yield chemical information precisely because they are sensitive to core levels that depend more weakly on bonding topology.

Apart from topographic scanning, the present work also exploits the capability of the STM to perform local tunneling spectroscopy by holding the lateral tip position momentarily, sweeping the voltage bias, and recording the quantities that change in the process. Spectra displayed in the present work were acquired by gating the feedback as the bias was swept, in order to freeze the vertical position of the tip. According to this procedure, spectroscopic measurements record both  $I$  vs.  $V$  and  $dI/dV$  vs.  $V$ .

The extraction of surface state information from such spectra is tricky. If the tip is approximated as a free-electron gas as above, the resulting expression for the tunneling current is

$$I \propto \int_0^{eV} \rho(E) T(E, eV, s) dE, \quad (2.2)$$

where  $\rho$  is the surface density of states (DOS), and  $T$  represents the transmission probability of an electron of energy  $E$  away from the fermi level, with a tip bias of  $V$ , and tip distance  $s$ . The quantity measured by  $dI/dV$  is illustrated in fig. 2.3. In general, we may write  $I = I(s,V)$ , so that

$$dI = \left( \frac{\partial I}{\partial V} \right)_s dV + \left( \frac{\partial I}{\partial s} \right)_V ds, \quad (2.3)$$

$$\frac{dI}{dV} = \left( \frac{\partial I}{\partial V} \right)_s + \left( \frac{\partial I}{\partial s} \right)_V \left( \frac{\partial s}{\partial V} \right)_I.$$

When the feedback is gated,  $ds=0$  so that the differential conductivity spectrum measures the slope of one of the I-V curves in fig. 2.3. We note that if, during spectroscopic measurements, the feedback is allowed to operate such that  $dI=0$ , then  $s=s(V,I)$ , and the measurement samples the slopes of a number of I-V curves along an iso-current line. In that case, the measured quantity would be  $(\partial I(V)/\partial V)|_{s=s(V,I)}$ . The fact that each of the three variables in  $(s,V,I)$  space may be written as a function of the other two on the domain  $\{s>0, I \times V > 0\}$  imposes the Euler relation,

$$\left( \frac{\partial I}{\partial V} \right)_s = - \left( \frac{\partial I}{\partial s} \right)_V \left( \frac{\partial s}{\partial V} \right)_I, \quad (2.4)$$

on the path followed in this domain.

The shape of a differential conductivity spectrum depends strongly on the tip-sample separation, rising more sharply at smaller distances. It is therefore desirable to "normalize" a spectrum so that its shape is independent of the initial conditions of the measurement. The goal of such



## Conductivity Measurements

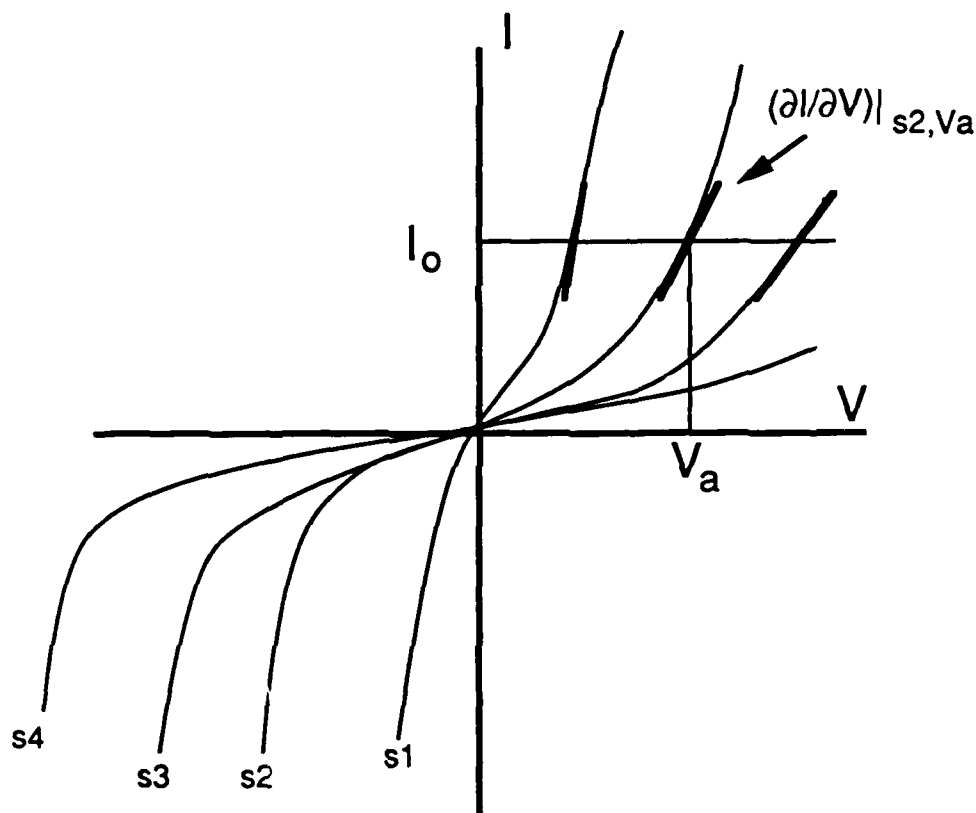


Fig. 2.3: Definition of conductivity measurements in tunneling spectroscopy. Each lateral position is associated with a sequence of I-V curves according to the tip height  $s$ , which is fixed by  $I$  and  $V$ . If a 2d scan acquired under bias conditions  $(I_0, V_a)$  is interrupted at a lateral position where the tip height =  $s_2$  and the feedback gated at that point, then sweeping the bias voltage would result in the I-V curve labeled "s2." If the feedback were not gated during the bias sweep, then a differential conductivity measurement would sample each of the tangents of the I-V curves along the line  $I=I_0$ . These slopes are represented by the heavy lines.

a normalization scheme is to remove from the recorded spectrum the strong exponential dependence of the transition probability  $T$  on tip-sample separation  $s$  and bias  $V$ . This exponential behavior is manifest, for example, in the WKB approximation to  $T$  for the trapezoidal barrier of fig. 2.2, given by

$$\begin{aligned}
 T(E, eV, s) &\propto \exp \left\{ -2 \int_0^s dx \sqrt{\left( \frac{2m}{\hbar^2} \right) (\phi - E + eV(1 - \frac{x}{s}))} \right\} \\
 &= \exp \left\{ \frac{4s\sqrt{2m}}{3\hbar eV} ((\phi - E)^{3/2} - (\phi - E + eV)^{3/2}) \right\} \quad (2.5)
 \end{aligned}$$

A natural first attempt at normalization might be to record  $d(\ln I)/dV$  vs.  $V$ , but this quantity diverges as  $V \rightarrow 0$ . The divergence is removed by recording instead the dimensionless quantity  $d(\ln I)/d(\ln V)$  vs.  $V$ , which automatically equals unity at  $V=0$ . (Fe87) The usual justification is based on dimensional analysis.

Differentiating eqn. 2.2 above yields the measured quantity

$$\left( \frac{\partial I}{\partial V} \right)_s \propto e \rho(eV) T(eV, eV, s) + e \int_0^{eV} dE \rho(E) \left( \frac{\partial}{\partial (eV)} [T(E, eV, s)] \right)_s. \quad (2.6)$$

The normalization of the differential conductivity then leads to

$$\frac{(\partial I / \partial V)_s}{I/V} = \frac{\rho(eV) + \int_0^{eV} dE \frac{\rho(E)}{T(eV, eV, s)} \left( \frac{\partial}{\partial(eV)} [T(E, eV, s)] \right) s}{\frac{1}{eV} \int_0^{eV} dE \rho(E) \frac{T(E, eV, s)}{T(eV, eV, s)}} \quad (2.7)$$

Now both the numerator and denominator have the transmission probability  $T$  appearing in a ratio in order to remove its strong exponential dependence on  $s$  and  $V$ , leaving an average DOS in the denominator. The appearance of  $\rho$  in the numerator suggests that a DOS spectrum may be extracted from a measurement of the normalized quantity of eqn. 2.7.

The second term in the numerator reflects the effect of the electric field in the barrier region of the junction. To appreciate the effect of this term, we note first that in the general tunneling situation depicted in fig. 2.2, the transmission probability is a maximum for states near the Fermi level of the negatively biased electrode. For negative tip bias,  $T$  is peaked at  $E=eV$  above the surface fermi level of the sample, so all terms in eqn. 2.7 have the same order of magnitude, and a measurement of the normalized differential conductivity should reflect closely the surface DOS. If, however, the tip is positively biased with respect to the sample, then  $T(E, eV, s) > T(eV, eV, s)$  for states with  $|E| < eV$ . Then both the denominator and the second term of the numerator of eqn. 2.7 are larger than the DOS term by the factor  $T(0, eV, s)/T(eV, eV, s)$ , and an attempt at extraction of occupied DOS information from the background in such spectra may be less conclusive. In both cases, the DOS term in the numerator of eqn. 2.7 is at most comparable in magnitude to the other terms, so the barrier field term cannot be neglected in the interpretation of

spectra. Even in the case of negative tip bias, we shall see that it can give rise to the dramatic phenomenon of negative differential conductivity.

Combining the scanning and spectroscopic capabilities of the STM, two-dimensional energy-resolved images have previously been acquired either by imaging the differential conductivity,  $dI/dV$ , directly (Be85c) or by subtracting individual total conductivity ( $I/V$ ) measurements recorded at each point in a topographic image. (Tr85) The present work utilizes the former technique exclusively. It is argued below on general grounds (St88) that constraints on the applicability of the latter technique, often called the CITS method, preclude its use here. As with individual spectroscopic scans discussed above, the problem is the extraction of DOS information from the background.

Consider a semiconductor surface with two types of atoms,  $a$  and  $b$ , and with a surface state localized on atom  $a$ , so that the tip-sample separation is larger with the tip above atom  $a$ , at the scanning bias  $V_0$  and tunnel current  $I_0$ . As a gated  $I/V$  spectrum is recorded, a constant tip-sample separation is maintained while the magnitude of the bias voltage is reduced. The tunnel current  $I$  is determined entirely by the bias  $V$  and the fixed separations,  $s(a)$  and  $s(b)$ . In order to compare the differential conductivities at the two sites, first take  $(\partial I/\partial s)_{a,V_0} \approx (\partial I/\partial s)_{b,V_0}$  with the scanning conditions,  $V=V_0$  and  $I=I_0$ , in effect. Now consider  $V \rightarrow V_0 - \Delta V$ . From eqn. 2.5, the decay of the transmission probability with distance increases as the bias is reduced below  $V_0$ , so  $|(\partial I/\partial s)_{V_0-\Delta V}| > |(\partial I/\partial s)_{V_0}|$ . Now, since  $s(a) > s(b)$ , the previous statement implies that  $|(\partial s/\partial V)_{I,a,V_0-\Delta V}| > |(\partial s/\partial V)_{I,b,V_0-\Delta V}|$ . Using eqn. 2.4,  $|(\partial I/\partial V)_{s,a,V_0}| > |(\partial I/\partial V)_{s,b,V_0}|$ . While  $I_a = I_b = I_0$  at  $V=V_0$ , from the preceding considerations we find  $I_b > I_a$  for  $V < V_0$ . Thus, while  $|\partial I/\partial V|_s$  is larger on atom  $a$  at  $V=V_0$ , there must be some

bias  $V_1(<V_0)$  below which  $|\partial I/\partial V|_s$  is greater on atom  $b$ . Therefore, the background due to barrier transmission effects falls out of phase with the topography in the CITS technique at low biases. This reversal has been reported for the Si(111)2x1 surface, a model reconstruction with two electronically inequivalent atomic sites. (St88)

Here again, then, some normalization is required to suppress the prominence of the background from changes in the transmission probability, and images of the differential conductivity normalized as in eqn. 2.7 have been shown to display a consistent phase relationship with corresponding topographs in an impressive number of cases. (St88) In fact, a direct image of  $dI/dV$  acquired with the feedback operating is automatically an image of  $(dI/dV)(V/I)$ , the normalized differential conductivity, because of the feedback-imposed constancy of  $I$  and  $V$  during imaging. As many of the surfaces examined in this study do incorporate multiple atomic species, the direct acquisition of images of  $dI/dV$  at the voltage used for constant-current tunneling is evidently to be the preferred method of generating energy-resolved pictures that contrast the two species. Consequently, this is the procedure employed in the present study.

We emphasize, however, that even this acquisition scheme does not automatically yield pictures that can be interpreted unambiguously in terms of a density-of-states distribution, for there inevitably remains a background that appears as the *reverse* of the topography. In the preceding discussion, which focused on the influence of surface states, the variation in  $(\partial I/\partial s)$  among the *lateral* positions that fall directly above different atomic sites was neglected. However, a different set of considerations applies when a topographic maximum that coincides with an atomic position is contrasted with its own, local, *interatomic* environment. In this case, it is clear that a

local maximum in  $|(\partial I/\partial s)_V|$  occurs directly on the atomic site as a result of a non-zero radius for tunneling. This derivative can be related to the differential conductivity by the Euler relation (eqn. 2.4) if the behavior of  $(\partial s/\partial V)_I$  is known. Eqn. 2.1, which reflects only topography, suggests that  $(\partial s/\partial V)_I \propto ((\partial I/\partial s)_V)^{-3}$ . Eqn 2.4 then leads to the conclusion that when surface states are neglected, purely topographical considerations force the contrast in the differential conductivity between the atom and its surroundings to fall out of phase with the local topography when the  $dI/dV$  image is acquired with the tip following a constant-current contour. This effect was observed by Becker, et. al. (Be85c) on Si(111)7×7, and was later confirmed by Binnig and Rohrer. (Bi86)

In adherence to this constraint on the interpretation of differential conductivity images, we employ such images to highlight the contrast in the electronic structure associated with *different types of atomic sites*. As we have seen above, inevitable topographic background effects may obscure further localization of surface state information. We therefore do not attempt to use  $dI/dV$  images to infer *interatomic* LDOS information .

## II.2 Apparatus

### II.2.1 Mechanical Design

The coarse positioning of the tip is accomplished with a rigid MACOR tripod, or "louse." (Fig. 2.4) A piezo scanning tube and its electrical connections are fixed to the tripod, which in turn sits on a square piezo plate that expands 5μm with 1kV applied between the two faces. Alternate expansion of the plate and capacitive clamping of the tripod's feet to the plate accomplish the motion, according to the timing in fig. 2.5.

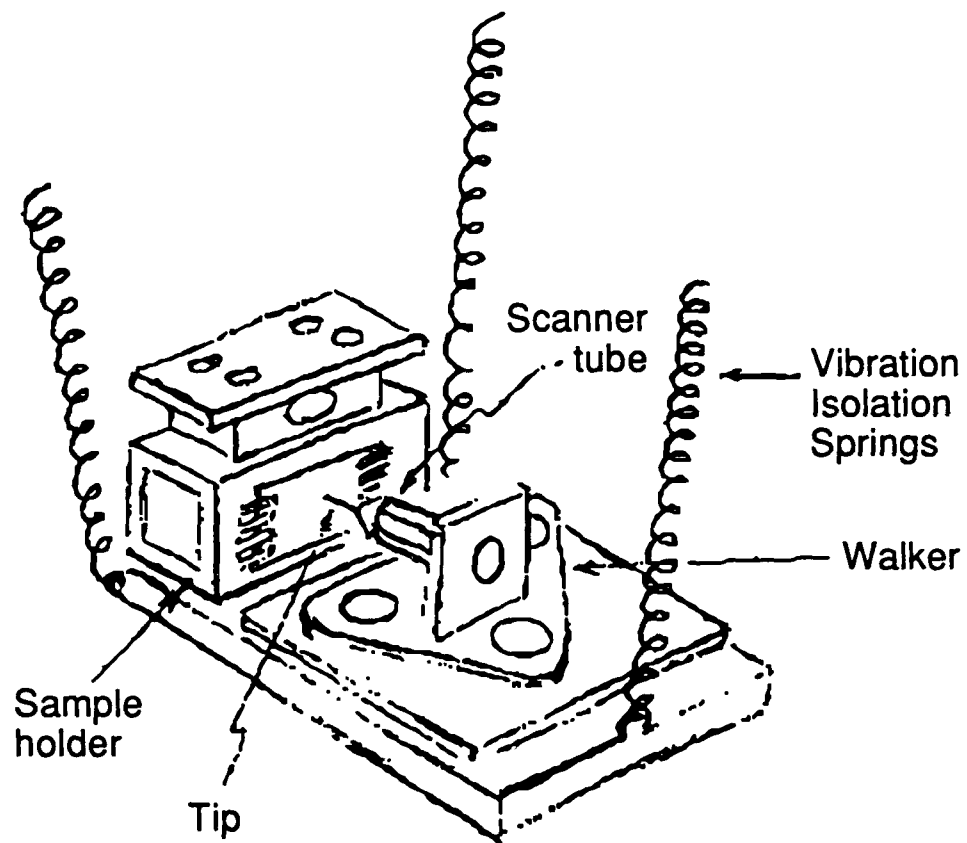


Fig. 2.4: Sketch of the working parts of the STM. The louse and piezo plate are collectively called the "walker."

## Walker Timing

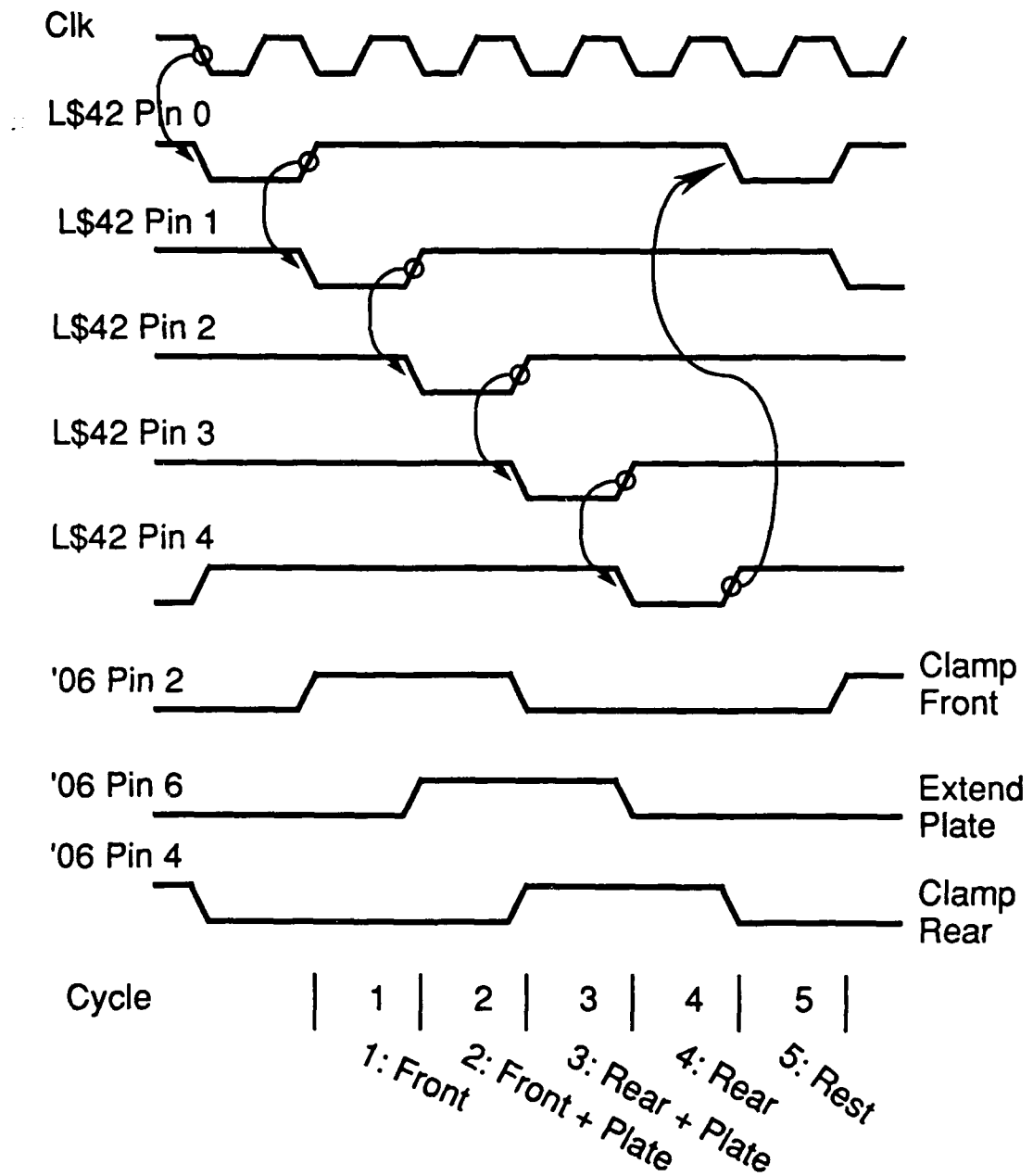


Fig. 2.5: Timing diagram for the walker, consisting of the louse, or tripod, and the piezo plate. The walker provides the coarse tip positioning. The feet are clamped by applying 600V, and the plate contracts with 1kV applied.



Any of the three clamps may lead, so both a direct approach to the sample and lateral motion are possible.

The electrodes of the piezo plate are formed by evaporating 500Å of chromium and 1000Å of platinum on each face. The transducer must then be poled by immersing it in tetrachloroethane and applying 2kV across it. A series of screws clamp two opposite edges of the plate to the microscope stage. The plate and tripod together are referred to as the "walker."

The tripod's three "feet" are 1/2 in. aluminum half-spheres milled down to a flat face, polished, and fixed to the tripod by Torr-Seal™, a vacuum-compatible epoxy. Sapphire disks, 3-4 mil. thick, prepared and polished by Crystal Systems of Salem, MA, are affixed to the face of each half-sphere with Epo-Tek H31 conducting epoxy. These disks form the insulator between each foot and the upper electrode of the piezo plate, which is electrically grounded in normal operation. Individual feet are clamped in vacuum by applying up to 600V, and the step size can be adjusted continuously by varying the voltage applied to the electrode on the underside of the plate up to 1kV.

The essential parts of the STM are drawn in figs. 2.4 and 2.6. The louse and plate together sit on the translation stage of a Princeton Research Instruments UHV stepping motor, which itself serves as an alternate mechanism for normal approach to the sample. The motor provides step increments down to 1/3  $\mu\text{m}$  without measurable overshoot and has been found to reproduce the number of steps for a given displacement very reliably. Caution must be exercised if the motor is used immediately before tunneling, for then the heat it generates must be dissipated entirely if thermal drifts are to be avoided.

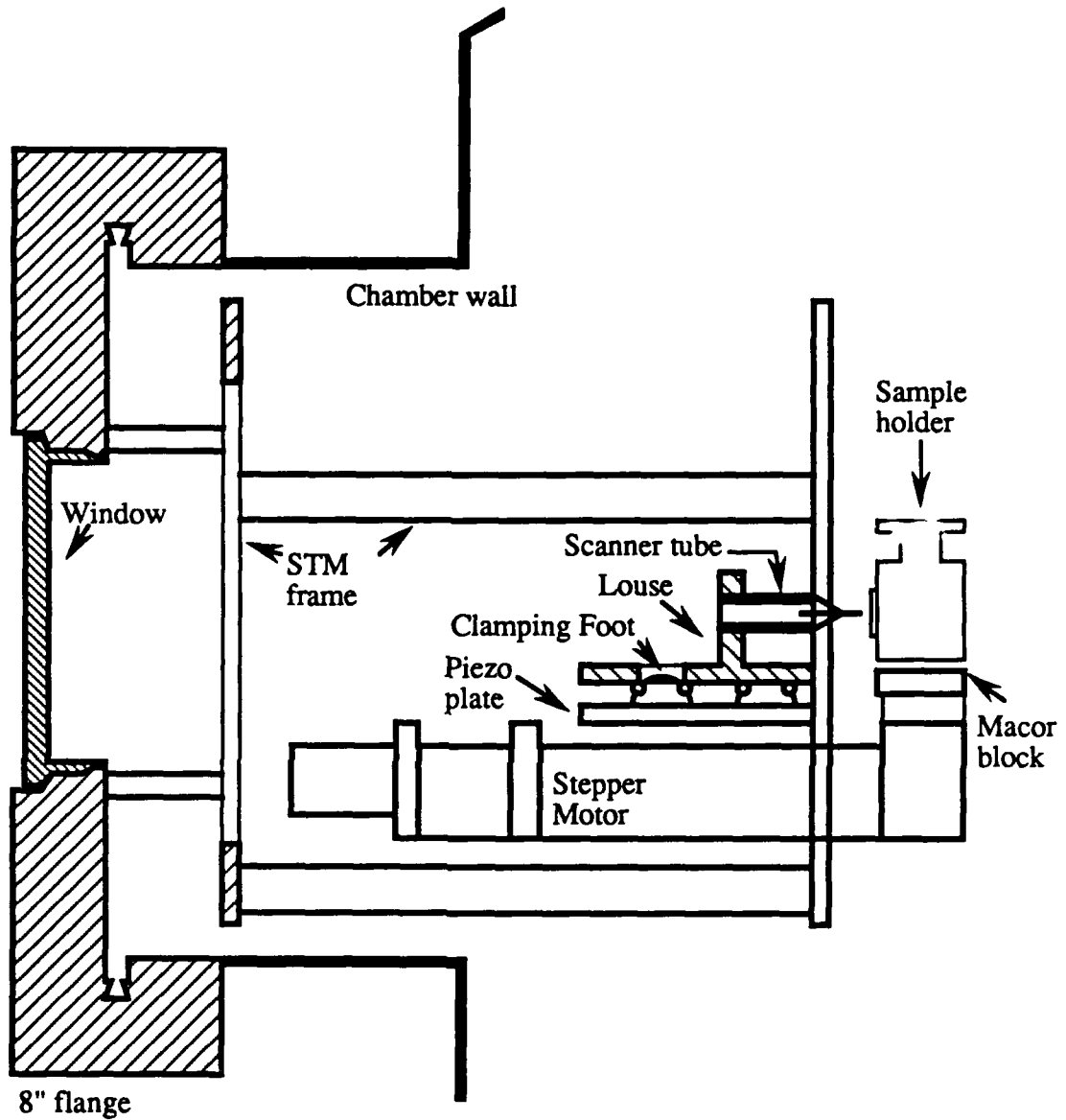


Fig. 2.6: Cross-sectional view of the STM as mounted in its operating position in the UHV chamber. Only the principal parts are shown. Springs, electrical leads, and connections, and feedthroughs are omitted. The picture is drawn to scale, with 1.75"=1".

Fine tip adjustments utilize the scanner tube, a 1/2 in. long, 1/4 in. diameter PZT cylinder from EDO of Salt Lake City, UT, which had been shipped poled. One end of the cylinder was affixed with Torr-Seal to a vertical wall on the louse, and on the other end was glued a steel cone which holds the tip. A 3/8 in. long, 20 mil. diameter, replaceable tungsten tip is accommodated through a hole at the apex of the cone and is clamped in place by a set screw. The inner electrode of the scanner tube is used for normal ( $z$ ) displacement; the outer electrode was etched into four quadrants, which provide complementary deflections in two orthogonal, lateral directions ( $x$  and  $y$ ). Opposite pairs of electrodes are always biased symmetrically about 500V, and displacement is accomplished by separating the voltages of each electrode in the pair in opposite directions, away from 500V. Application of 1kV to the inner,  $z$  electrode would shorten the tube by 1.6  $\mu\text{m}$ , while a full 1kV differential between opposite  $x$  or  $y$  electrodes resulted in a 5 $\mu\text{m}$  lateral displacement as measured by a Federal (Livonia, MI) indicator unit.

The copper sample block accommodates 10-20 mil. wafers cut to .5 $\times$ .6 in. Fashioned tantalum clips both clamp the sample to the holder and provide a conducting path for the sample current. An alumina spacer insulates the sample from the block. The block is clamped to the MACOR slab on which it sits during tunneling by an internal compression spring. The block does not actually contact the ceramic; instead, it rests on a tripod of steel balls glued to the block by Torr-Seal. These balls make contact with electrodes underneath the sample block. One conducts the sample current, and one provides a ground path to the return shield of the current line. While the block is grounded to this latter ball, a copper electrode underneath the sample block and electrically isolated from it by sapphire

spheres connects to the sample current lead. The block's upper face also provides connections to each of the tantalum clips and to a thermocouple, in order to contact leads on the sample manipulator during sample annealing.

The stepping motor, on which the microscope is constructed, hangs from two aluminum bars by three stainless-steel springs, each attached at either end by viton O-rings. The frame, consisting of three aluminum bars running the length of the STM, is fixed to an 8" Con-flat™ flange custom manufactured by Princeton Research Instruments. The flange includes a window, sixteen BNC connections, and four mini-Con-flat ports. A linear feedthrough attached to the lowest mini port can clamp the microscope during sample mounting and removal.

Electrical leads of solid copper wire run from BNC connectors, along the aluminum bars, to the microscope stage. These leads are insulated from one another by fiberglass sleeving. For the triaxial leads to the tip and the sample, the internal insulator consists of alumina "fish-spines." Each lead is attached to one of the spring posts mounted in a row on a MACOR bar on either side of the stepper motor assembly or behind the sample block. From each such post, a three mil. copper wire, wound into a spring, jumps to another spring post on the microscope stage. Individual 3 mil. copper wires connect these posts to their destination. Connections to the five electrodes on the scanner tube and to each face of the piezo plate are soldered. A gold wire passes through an alumina insulator inside the scanner tube and reemerges through the hole at the apex of the cone that holds the tip. The wire is then wound around the tip to make electrical contact. The sample current lead alone is connected to a triaxial Ceram-a-seal™ feedthrough on one of the mini ports. The stepping motor leads emerge via a multi-pin connector on another mini port.

The entire microscope is encased in a tantalum thermal shield. The cylinder that runs the length of the microscope includes holes for illumination and for viewing the tip approach. A shutter on the vacuum end is opened for sample mounting and removal but closed during sample preparation and is controlled by a rotary feedthrough on one of the flange's mini ports. The materials used are UHV-compatible and selected to withstand routine baking at 125°C. The copper sample block and solid wires are OFHC material, the insulators are ceramic, and the nuts, bolts, washers, and springs are stainless steel.

### II.2.2 Vibration Isolation

The successful integration of the STM into its working environment necessitates careful vibration isolation. Vibrations that interfere with imaging arise from both building resonances transmitted through the floor and from acoustic coupling. To suppress the latter source, we have simply relied on tightly disciplined restraint during data acquisition. The former cannot in general be dismissed by behavior modification and must be confronted. The resonant frequency of the instrument must be pushed below the frequencies present in the floor, which are typically 4-10Hz.

We have employed both internal and external isolation. Inside the chamber, the microscope stage is suspended by three stainless steel springs from the frame, which consists of three bars, rigidly attached to the 8 in. flange and running across the length of the instrument, with two supporting rings on either end. Collectively, the spring system resonates at 5 Hz. In addition, a viton O-ring attached to one of the supporting rings pushes inward on the microscope stage, providing lateral damping. All electrical

connections to the STM stage employ soft, thin wire wound into spring coils.

The number of connections from the chamber to any other instrument must be kept to a minimum. Individual RG-58 coaxial cables carrying the STM control signals from the instrument racks run along the floor to a patch panel adjacent to the chamber, from which the softer, RG-174 coaxial cables complete the connections to the BNC inputs on the STM flange. The only other connections to the chamber that remain are the ion pump's high voltage and grounding lines, and a copper braid connecting the chamber with the instrument ground at the patch panel. Because of its lack of moving parts, only the ion pump may continue to operate simultaneously with the STM.

External to the chamber, vertical vibrations are damped by floating the whole apparatus on four pistons, constructed from 1m aluminum cylinders. These pistons in turn sit on a stage that swings as a pendulum, supported by four 1m steel cords. The combination of the pistons and pendula isolate the chamber mechanically from the floor. (See fig. 2.7) The orders of magnitude of the excitations in the isolation system may be estimated as follows. The resonant frequency  $\omega$  of an air column of length  $l$  follows the form,

$$\omega = \sqrt{g/l}.$$

For four cylinders of height 1m, used on our air table, the overall resonant frequency should fall near 2Hz, neglecting the effect of the gaskets on the tops of the cylinders. The pendulum resonance should be comparable.

The effects of various isolation components are best illustrated by example. The low-frequency floor and table vibration measurements of figs. 2.8 - 2.10 were acquired with geophones, from Mark Products, connected directly to a spectrum analyzer. With no isolation (fig. 2.8a), a strong floor resonance at 7.6 Hz is evident. When the pistons are raised, the floor vibrations are suppressed (fig. 2.8b, note the change in scale), but several piston resonances appear. Once the pendulum is released, the vertical geophone reveals only one strong component at 1.725Hz (2.9a). The horizontal geophone still detects the floor vibration, now strongly attenuated, at 8.65Hz, and a component at 1.2Hz (2.9b). Without the external isolation in effect, stable tip positioning for tunneling could not be accomplished at all.

After the external isolation is put into effect, internal resonances can be observed by analyzing the tip response during tunneling. The low-frequency spectrum thus acquired (fig. 2.10a) shows the persistence of the 8.65Hz floor vibration, now attenuated to a level that corresponds to  $<0.15\text{\AA}$  p-p normal displacement, acceptable for the present work. A spectrum that covers a wider range (fig. 2.10b) reveals the STM's internal resonances at 167 and 551Hz. These two frequencies breed persistent instability, and in a particularly dramatic display, the lower component can be driven substantially by activating the stepping motor once (fig. 2.10c).

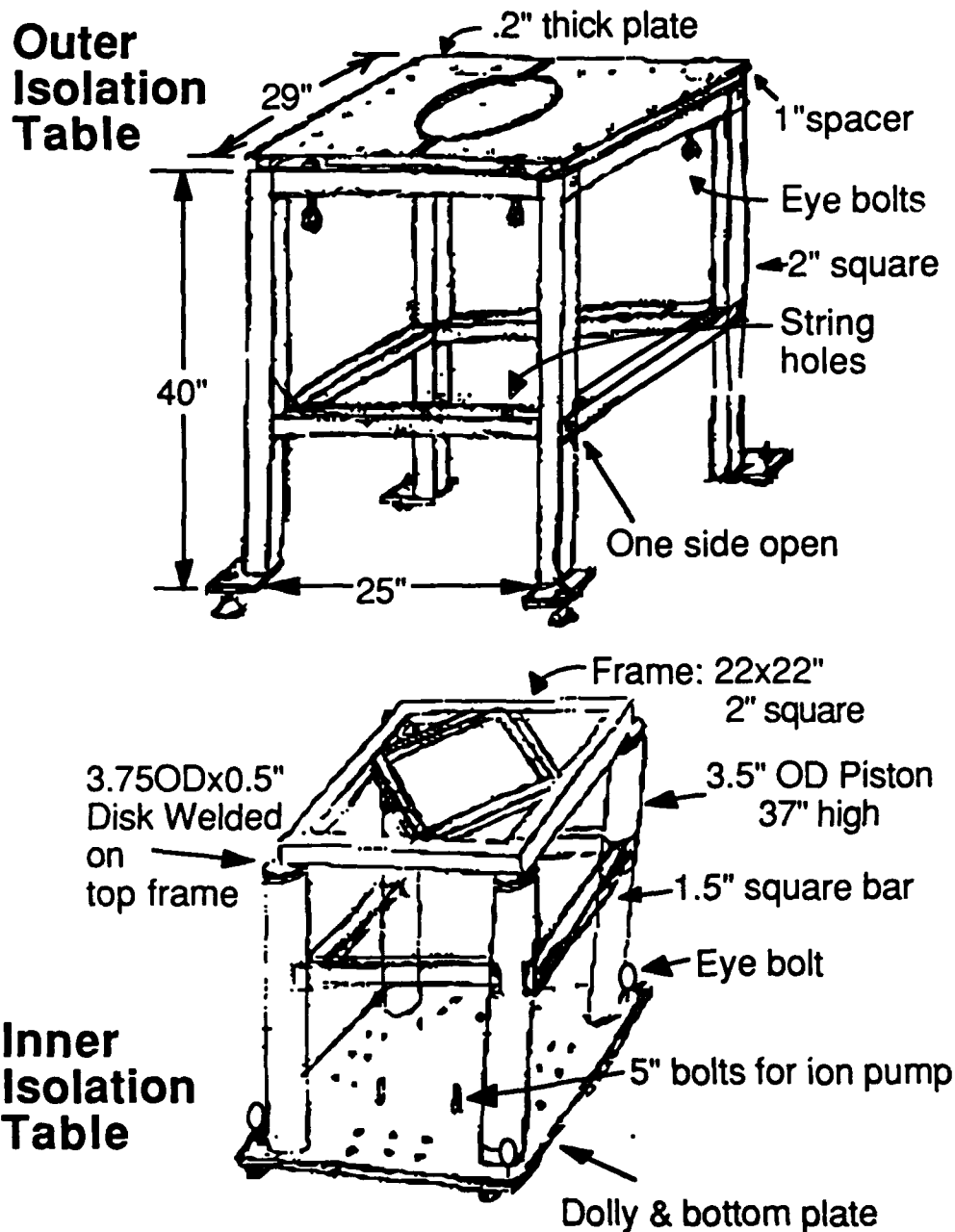


Fig. 2.7: External vibration isolation. The chamber is mounted on the top frame of the inner table, which is suspended from its eye bolts by cables originating at the eye bolts of the outer table. During sample preparation the two tables are rigidly attached. During tunneling, the inner table does not touch the floor.



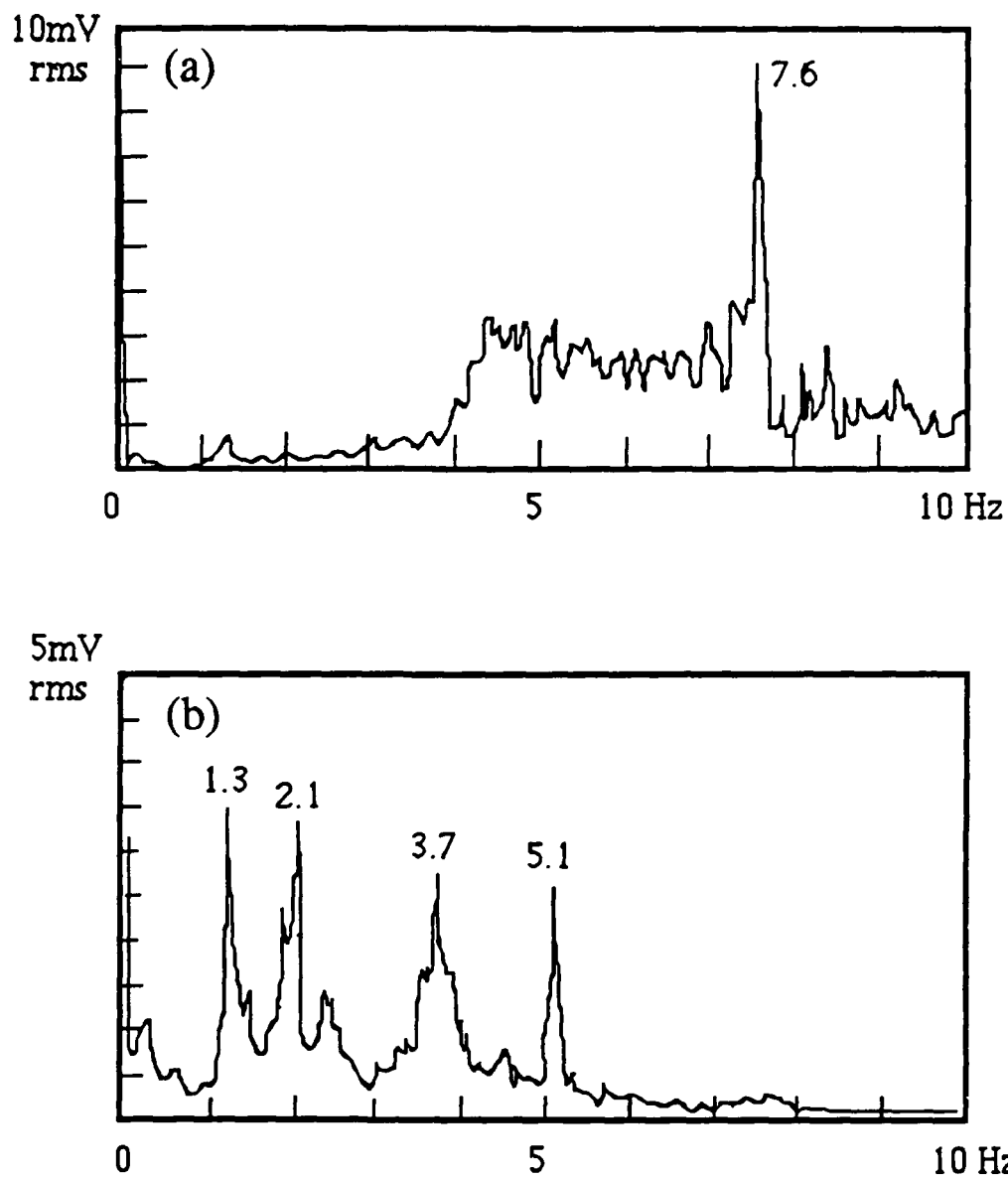


Fig. 2.8: Vibration spectra from a vertical geophone on the vacuum chamber, with (a) no vibration isolation; (b) the pistons on the air table raised. Note the change in vertical scale.

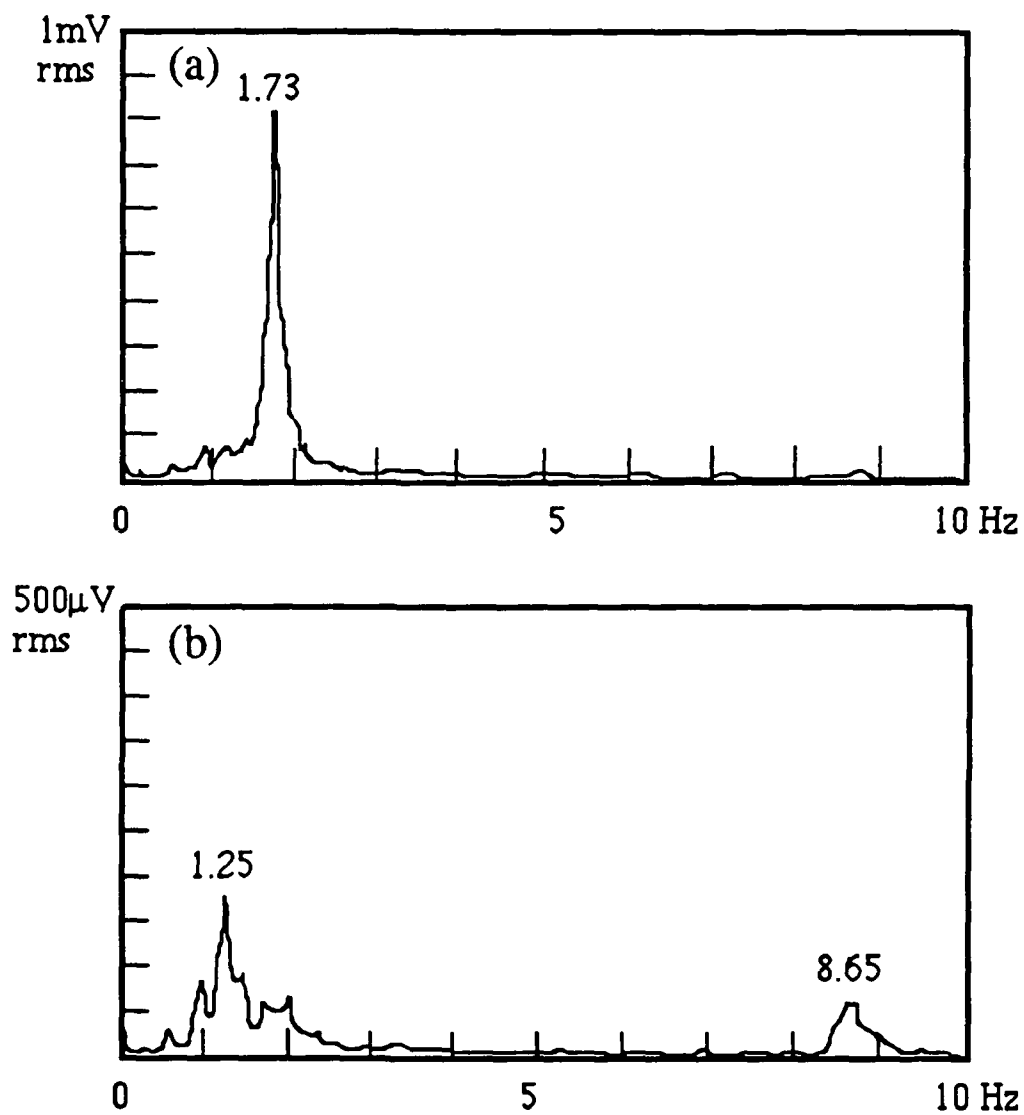


Fig. 2.9: (a) Vertical, and (b) horizontal geophones seated on the vacuum chamber with the pistons floating and the pendulum released.

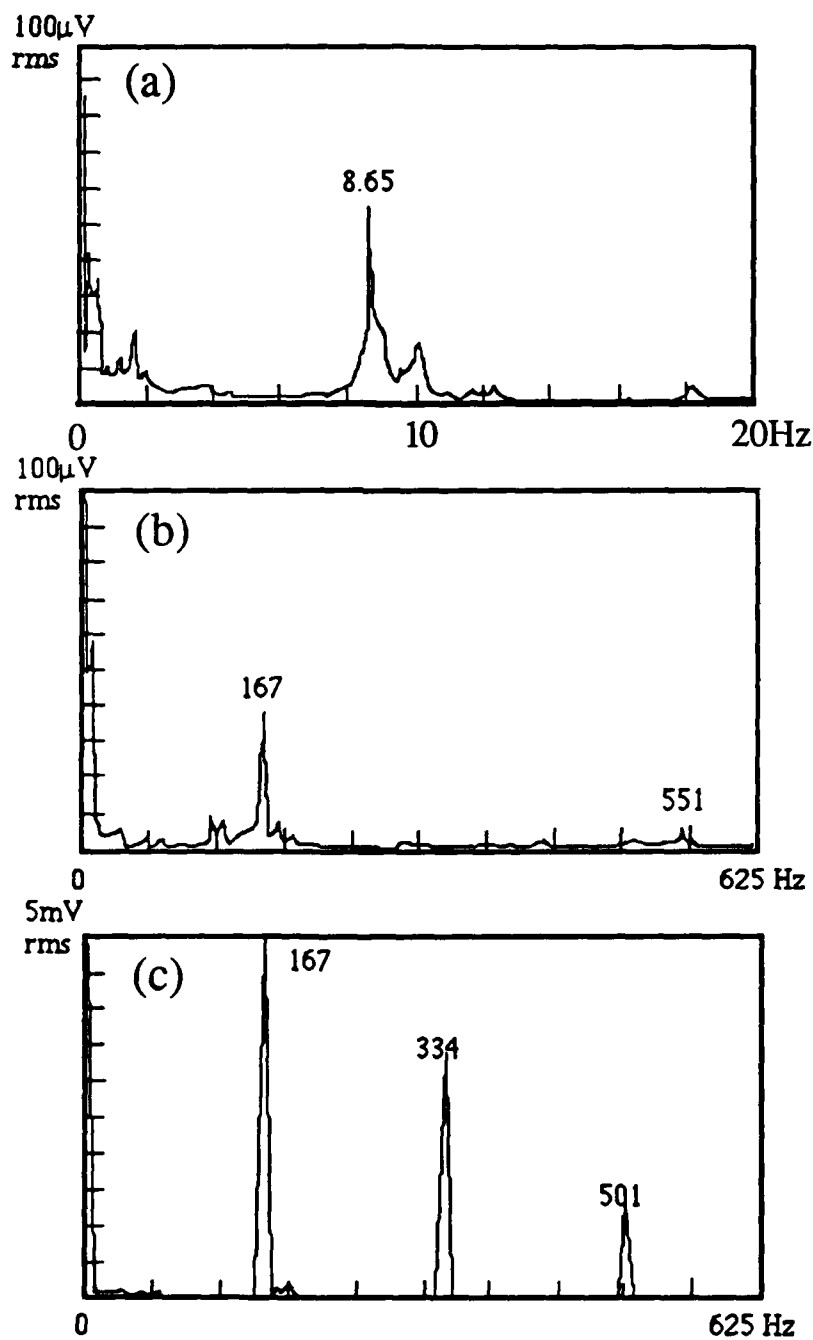


Fig. 2.10: (a,b) Spectral analysis of tip current with vibration isolation. (c) Similar spectrum after pulsing the stepper motor once.

### II.3 Electronics and Data Acquisition

The STM control electronics, like the hardware, were designed and built in their entirety in-house at Harvard. A thorough explanation of each of the circuits below is followed by a description of their integration.

Each electrode on the piezo tube, the piezo plate, and the three loose feet is driven by its own high voltage amplifier, depicted in fig. 2.11. The gain of each amplifier is 100 for positive signals in the range 0-10V, as provided by the outputs of each of the low-voltage control circuits. The frequency at which the amplifier's gain falls by 3dB from its dc value of 100 is 16kHz. The two BUZ-50B n-channel MOSFETs have a drain-source breakdown voltage of 1000V. The first inverts the signal from the 748 and the second serves as a source follower. The voltage gain of 100 is determined by the divider network from which the feedback to the 748 is taken. The sampling of the output by the non-inverting input of the 748 provides the additional 180° phase shift that makes the amplifier non-inverting overall. Thus, a rising input signal lowers the gate bias of the first MOSFET, lowering that transistor's drain current and raising the gate bias of the second MOSFET. The resulting higher source current raises the output voltage.

A 10 $\Omega$  resistor from the neutral input to the circuit common breaks the ground loop that would otherwise result in unacceptable levels of ripple. An uncompensated op-amp, the 748, was selected in order to boost the amplifier's overall frequency response, and the npn transistor (2N3904) from its non-inverting input to its output suppresses ringing for signals that fall near 0 V. Output current limiting is provided by the second npn transistor, which robs current from the MOSFET follower's gate drive when

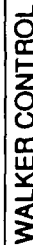


the current through the  $39\Omega$  resistor raises the voltage across the base-emitter junction above the threshold for conduction. Because the output is not a true push-pull stage, a return path must be provided for the transducer's discharge when the drive is removed. The path to ground realized here leads across the signal diode that shunts the current-limiting transistor's collector-emitter path, through the  $180\Omega$  gate bias resistor to the drain of the first MOSFET, and then to ground, since that FET is by then biased into conduction.

Because the first MOSFET conducts when no bias is applied, there is a 3mA quiescent current from the high voltage line through that transistor's drain resistors. The 1kV dc level is supplied externally. The components indicated on the schematic were chosen to provide stable ac swings for a transducer with a capacitance below 10,000pf. The 1/2 in. long scanner tube has an overall capacitance of 3nf, and each louse clamp presents 80-110pf. The piezo plate presents 17nf, but the amplifier in that case is used switching, where the waveform is not critical. The heat sinks dissipate the .25W maximum generated by the MOSFETS.

A total of nine amplifiers are required: five for the scanner tube, one for each capacitive clamp, and one for the piezo plate. Each amplifier was constructed on a printed circuit board, and the set of boards is housed in a card cage which also contains the small, modular  $\pm 15V$  power supply required. The amplifier outputs are passed directly to the transducers in the case of the piezo tube, or through  $1M\Omega$ , 1W resistors to the louse clamps and plate. Each of the control circuits provides outputs scaled to the 0-10V range required by the high voltage amplifier inputs.

The circuit that controls the coarse tip positioning is displayed in fig. 2.12. Four timing options are provided. Automatic operation is available



36

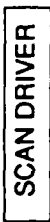
with the 555 timer unit and the front-panel frequency control shown. Alternatively, a front-panel switch connected to the flip-flops offers manual timing. The input at the upper left of the schematic can accept an external TTL clock signal. Finally, the whole operation can be software-controlled by turning the "leading clamp" switch to the "computer" position as indicated, where the circuit will accept TTL signals on lines C1-C5.

After the input source is chosen by the gate as shown, several logic operations generate the timing sequence of fig. 2.5 from the input pulse train. The two switches that follow determine the direction of motion. Once the destination has been reached, the louse can be clamped by placing the "leading clamp" switch in the "All" position indicated. The LEDs indicate the status of each signal line, and the final open collector outputs allow continuous adjustment of the clamping voltages by individual front-panel controls, as displayed in the inset. *Front panel meters display the clamping voltages at this point, and RC networks on the outputs prevent sudden transducer charging or discharging. The charging currents of the amplified signals are also displayed as shown to warn of any shorts at the capacitive clamps.*

The fine, lateral tip positioning is controlled by a Metra-Byte CTM05 counter-timer card in the PC, which in turn drives the Scan Driver circuit shown in fig. 2.13. For each channel, 'x' or 'y', one counter generates a train of pulses according to the scanning speed prescribed by the user, and a second counter, clocked from the first, triggers the A/D conversion when the tip reaches the end of the interval between conversions, again prescribed by the user.

In the circuit of fig. 2.13, the four 74HC191 binary up/down synchronous counters convert the incoming pulse train to a digitally



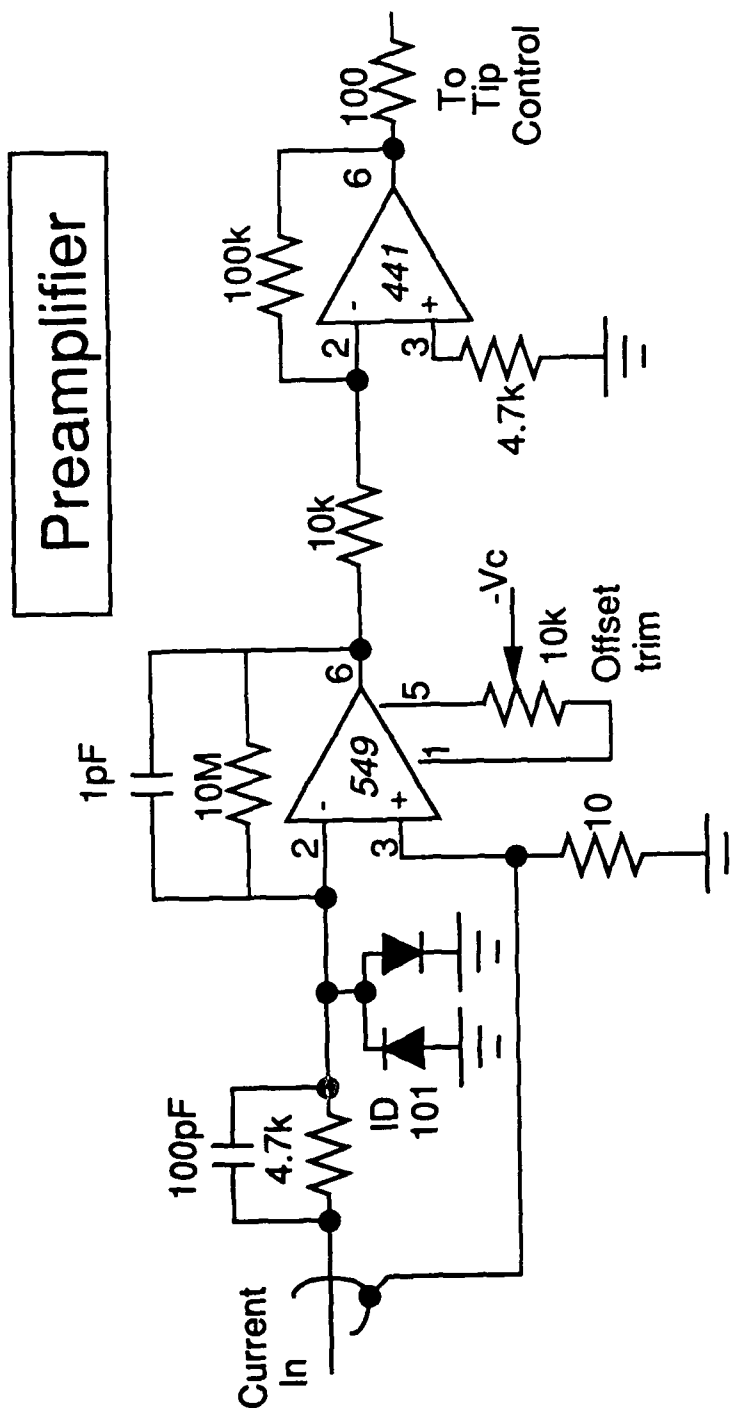


**AD581**  
**Bottom View**

encoded position. The direction of counting is determined by a software-controlled TTL input, as shown. A second pulse input provides control of the tip displacement independently of the counter-timer unit. A reset input is used to null the binary counter outputs, returning the tip to the center of its 'x' (or 'y') range. The PCM53KP-V, a 16-bit D/A chip, then generates an analog signal, which is deglitched by the 585, a sample/hold amplifier. The subsequent amplifiers rescale the outputs to positive polarity, as required by the high-voltage amplifiers. The two outputs are symmetric about +5V. A fine manual offset covering 10% of the full displacement is provided via a front-panel control, as shown.

The full lateral range of the piezo scanner used here is 5  $\mu\text{m}$  for 1kV applied. In order to keep lateral displacements below 1 $\mu\text{m}$ , a 5:1 resistive voltage divider was placed between each Scan Driver output and the corresponding high voltage amplifier input. At these levels, one input pulse results in a 1/6 $\text{\AA}$  tip displacement and a 305 $\mu\text{V}$  change in the D/A output level. The low signal levels involved in fine displacements and the mixing of analog and digital signals on one board necessitate certain precautions in circuit construction. The considerations reviewed elsewhere (Pi87) have been observed here. Two copies of the circuit in fig. 2.13 were constructed (one each for 'x' and 'y' channels) on solder breadboards with a ground plane and were mounted in a single chassis. Front panel meters for each channel indicated 'x' and 'y' displacements.

The sample current was sensed by a battery-operated current preamp, shown in fig. 2.14, that was mounted directly on the STM flange. The overall gain of the preamp is .1V/nA. Because the current levels sensed may fall well below the leakage currents of the printed-circuit boards employed, all connections to the amplifier's summing junction are isolated



**Notes:**

- Operates from two 9v batteries.
- All connections to the summing junction of the AD549 are via a teflon standoff post isolated from the circuit board

Figure 2.14

from the board with a teflon stand-off. The input clamping diodes are accordingly the low-leakage ID101 pair, for the leakage current of signal diodes would be unacceptable here. The first-stage amplifier, the 549, has been chosen for its compensation of the offset voltage as indicated is crucial to the acquisition of low-bias data in tunneling spectra. The  $10\Omega$  resistor from the input to common breaks the ground current path that would otherwise result in the appearance of unacceptable levels of ripple at the output.

The  $10M\Omega$  feedback resistor of this first stage produces a gain of  $10\text{mV/nA}$ , with a 3dB rolloff at 8.5kHz. The second stage provides an additional factor of 10 amplification. While it is possible to realize the full preamp gain with one amplifier by placing a  $100M\Omega$  resistor in the 549's feedback loop, the roll-off frequency would then be reduced by a factor of 10, too low to detect the 6kHz modulation in spectroscopic data acquisition.

The preamp output runs directly to the input of the feedback circuit of fig. 2.15, which controls the vertical displacement of the tip. The front end of this circuit provides a buffered output following IC16 to read the tunnel current directly, as in the spectroscopic mode. IC1 is configured here as an absolute value circuit to present the logarithmic amplifier's input (IC3) with the proper polarity. The 759 is used to linearize the feedback loop, which includes the tunnel junction with its exponential characteristic. A differential amplifier (IC6) compares the 759 output with a reference level which is derived from a voltage reference (IC15), rescaled to the appropriate dc level by ICs 7 and 8, and adjustable by a front panel control. The error signal at IC6's output is integrated by IC13 for maximum dc gain, and a front panel control that adjusts the level of the error signal sets the

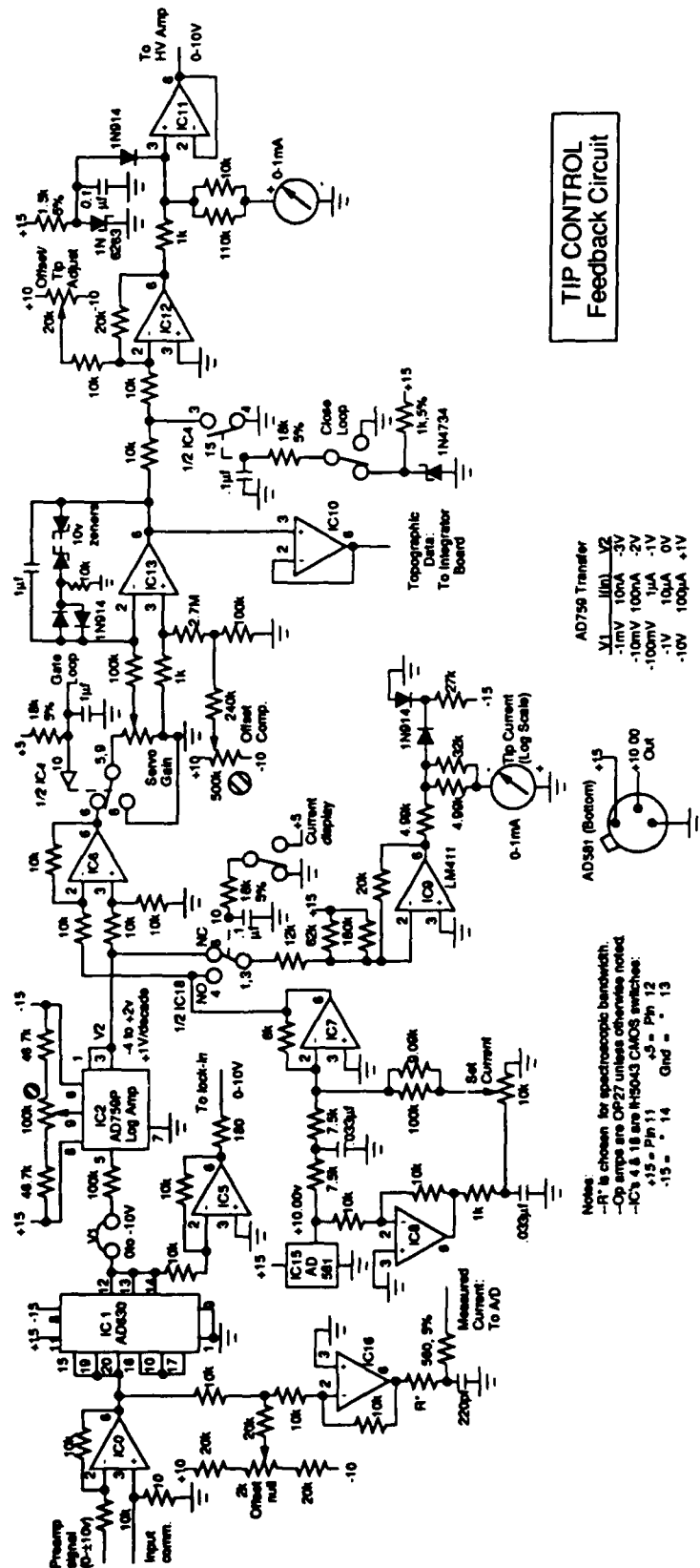


Figure 2.15

overall loop gain. A front-panel meter following IC9 displays either the set current or the actual current, depending on the switch position.

When the feedback is gated during spectroscopic scans, it is necessary to maintain the tip position within  $.01\text{\AA}$  for 100mS, which is an upper limit on software-controlled switch at IC6's output. With the input differential to IC13 removed, the output signal is fixed by the charge stored on the feedback capacitor. The compensation network on IC13 cancels that amplifier's input offset voltage, which would otherwise result in unacceptable output drift during the acquisition cycle.

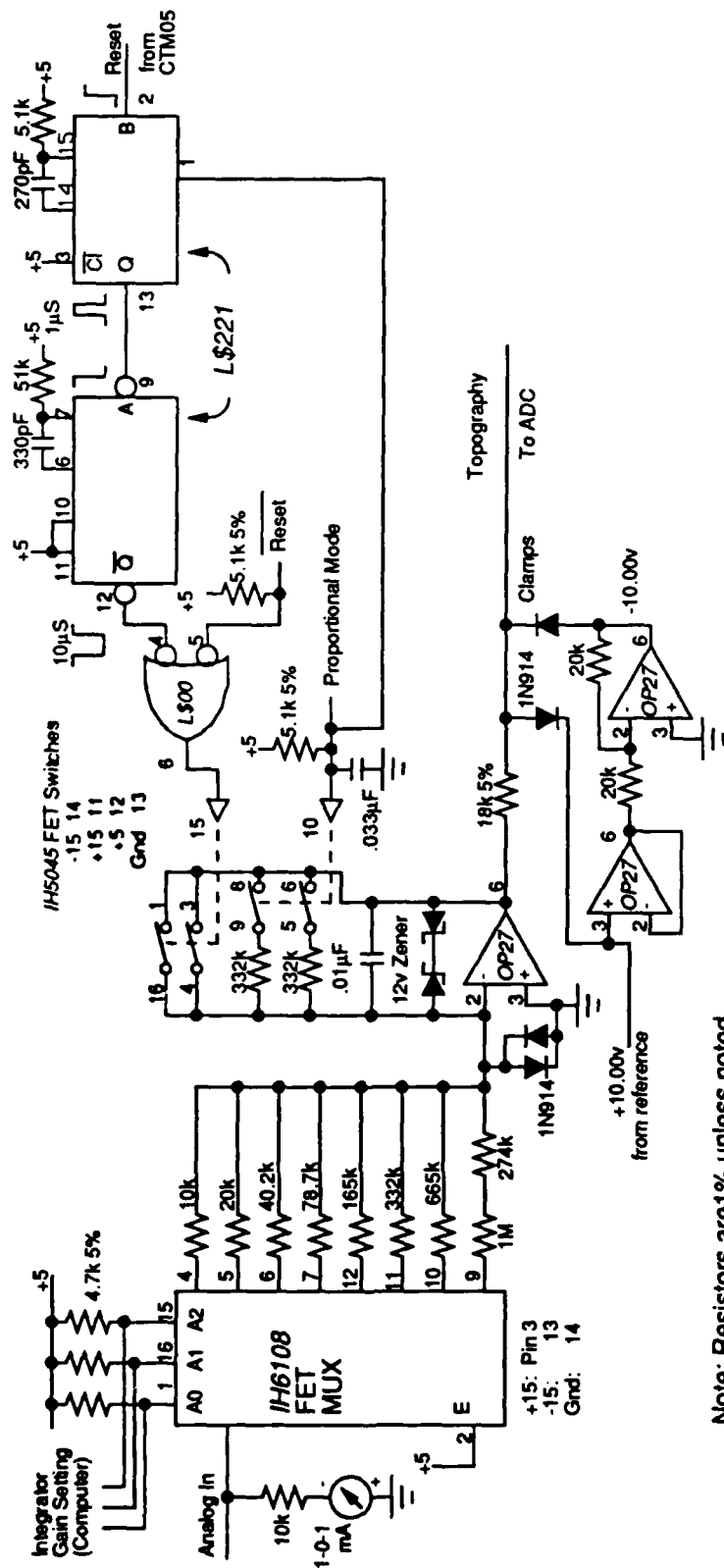
The topographic data are taken from the output of IC13 and buffered by IC10 before further processing and conversion in the PC. The tip adjustment signal itself must be offset before it is amplified. When the feedback loop is operating, the front panel offset control at IC12's summing junction is used to change the signal level at the output of IC13, which should be kept near ground for subsequent amplification of the recorded data. This control also serves as a manual tip adjustment when the feedback is opened, as during the tip approach. The capacitor in the feedback loop of IC12 rolls off the loop response for stability. A front-panel switch opens the loop in that case by removing the adjustment signal from the input to IC12. The tip displacement is displayed on a front-panel meter that senses the output from IC12. Finally, the clamps before the output buffer (IC11) enforce a positive-polarity signal for the high voltage amplifier.

The feedback circuit was designed according to specific requirements of overall stability, and it employs the high dc gain of an integrator. Within the STM's servo loop, the overall gain is the product of contributions from the log amp (1V/decade), the integrator ( $\leq 10/(2\pi f)$ ), the high-voltage

amplifier (100V/V), the transducer (16Å/V), and the junction ( $\approx 1$  decade/Å in idealized picture). Thus, the gain falls to unity at  $f = 2.5\text{kHz}$ . The dominant pole is clearly the integrator; a  $180^\circ$  phase shift therefore occurs at 8.5kHz, the preamp's 3dB point, which lies well above unity-gain point. The unity-gain frequency easily permits the typical scanning rates of  $\approx 350\text{Å/S}$ .

Sharing the same chassis as the feedback board is the integrator circuit of fig. 2.16, the analog input of which is the topographic data signal. A front-panel meter displays the level of this signal, which should be near zero when the feedback is operating and the tip offset is adjusted properly. The analog signal is passed through an integrator, which both amplifies and averages the signal. Three software-controlled bits set the gain by directing the signal through one of the resistors between the multiplexer (6108) and the integrator. The gain is then computed as the ratio of the integration time to the selected RC product. The amplified tip height signal is sent to an A to D converter in the PC, which is protected by clamps at the integrator output.

The integration time is naturally the interval between pixel readings, as determined by the counter-timer unit that drives the raster. Accordingly, the pair of one-shots (74LS221) shown generates a  $10\mu\text{S}$  reset pulse following a trigger from the counters. An alternate reset line is provided to prevent the integrator from railing when the tip is not scanning. The integrator may also be bypassed and the signal amplified proportionally when tip height data are acquired with the counters interrupted, as during spectroscopic scans. The change to proportional amplification is automatically handled under software control.



TIP CONTROL, INTEGRATOR CIRCUIT

Figure 2.16





The final circuit function required for STM control is the tip voltage bias, displayed in fig. 2.17. The dc bias is derived from a voltage reference, the 581, and is manually adjusted with a front-panel control. Front-panel switches fix the bias polarity, the output range, (1V or 10V f.s.), and the scale of the digital front-panel display. Two inputs permit the simultaneous addition of both a small modulation, usually derived from a lock-in amplifier, and a voltage ramp, taken from a D/A converter resident in the PC. These external signals are required for spectroscopic scans.

During the tip approach, it is necessary to bias the tip up to 1kV. Thus, it is critical to change smoothly from the high-voltage bias supply, provided here by the LEED unit, to the Tip Bias circuit. This is accomplished by connecting the wiper of the pot shown to the tip. To change supplies, the control is simply turned from one end of its range to the other.

Each circuit above was housed in its own chassis, unless otherwise noted. The units were mounted on one rack, together with power supplies, a lock-in amplifier, and an oscilloscope which displayed both the sample current and tip height signals continuously. "Solder breadboards" with ground planes, available from Douglas Electronics, were used throughout, and connections to these boards were made via 44-pin card edge connectors. Each chassis was equipped with a modular dc supply and could be powered from either the ac line for convenience during testing, or an external dc supply to suppress magnetic transformer coupling during tunneling.

Digital signals from the PC passed via ribbon cable to a panel at the bottom of the instrument rack, where they were redirected to their respective destinations. Analog signals from the instrument rack were



connected by coaxial cable directly to a box in which the common lines were connected to the analog common through  $10k\Omega$ . Six inches of ribbon cable carried the signals from this box to the analog interface board in the PC.

The block diagram in fig. 2.18 summarizes the interconnections of the control circuits described above. The PC/AT type CPU at the lower right of the schematic both coordinates the various scanning operations and stores the acquired data. Analog and digital interface signals are handled by a Metra-Byte CTM05 counter-timer board and a Data Translations DT2827 analog interface board, which provides four "16-bit" differential-input A/D channels. Both boards sit in the PC's expansion slots and also provide digital ports which are used as the control lines indicated above in the individual circuit descriptions.

The CTM05 board is programmed to displace the tip laterally at the user-specified speed, and to issue a clock signal to the DT2827 board when data is ready. During scans, the 'x' and 'y' clocks originating in the CTM05 card set the scanning speed. From these two clocks are derived two additional clocks, one of which is selected to trigger an A/D conversion for each pixel according to the user-specified spacing of data points and, after a  $1\mu S$  delay, to reset the integrator circuit in preparation for the subsequent pixel. The deflection of the tip by the four raster control signals (x, -x, y, -y) proceeds as indicated in the individual circuit descriptions above. When the DT2827 board has performed its A/D conversion, it issues an interrupt to the computer. The interrupt handler then processes the data and resets the A/D card for another conversion. The role of software in the data acquisition is therefore reduced to starting the scans. By operating the scans and taking data in the background in this way, continuous, powerful

foreground user control can be implemented without sacrificing timing precision.

When spectroscopic scans are acquired, the timers are suspended, and the voltage bias ramp is software-driven through one of the DT2827's analog output ports. An ac modulation from the lock-in's reference output, typically 6kHz and <100mV p-p, is added to the tip bias. The lock-in then detects the tunneling signal component at its reference frequency, which is proportional to the tunnel junction's differential conductivity. An analog input channel on the DT2827 board reads this  $dI/dV$  signal as a function of dc bias on the tip. A third analog channel reads the current signal from the preamp's output. During gated spectral scans, the CPU records both  $I$  and  $dI/dV$  vs.  $V$ , but during non-gated scans it can still record  $I$  (from the integrator circuit, set to proportional amplification) and  $dI/dV$  vs.  $V$ . The two-dimensional differential conductivity images shown in this work are acquired with the feedback and counters operating as with topographic scans, but with the display derived from the output of the lock-in rather than the tip height signal.

The number of controls and switches mounted on the circuit modules has been kept to a minimum. Most operations are under CPU control and are directed by the operator through the SCAN program, which was developed at Harvard. The program provides line scanning capability and arbitrary tip placement over the  $1\mu\text{m}^2$  lateral range of the scanning tube, so the topography of large regions can be sampled rapidly before two-dimensional images are acquired. In both line- and two-dimensional scans, the program presents the user with menus from which he selects such parameters as scan speed, size, and angle, data acquisition rate, and integrating amplifier gain. Tunneling spectra can be acquired individually

or by interrupting two-dimensional scans. The spectra can be acquired repeatedly and averaged, with the loop closed for  $\approx 2\text{mS}$  between individual scans.

Topographs are displayed on a 512x512-pixel gray-scale monitor driven by the Revolution Number Nine graphics board, which resides in the PC. Rudimentary image enhancement, including plane removal, contrast adjustment, and division into forward and reverse scans, is available for routine use before storage of images. When topographs are interrupted to acquire tunneling spectra, the program stores the location of each interruption together with the topographic and spectral data. A detailed description of the low-level control of the STM by the SCAN program is provided in the program's documentation. (Av87)

#### II.4 Vacuum Environment

The examination of atomically clean surfaces requires that each of the steps of sample preparation take place in the same vacuum chamber in which the STM resides, and all of the work described below employed a single Perkin-Elmer UHV chamber. (Fig. 2.19) A 300 l/s Balzers turbomolecular pump (TPU 330) was used for both roughing and removing the noble gases used in sputtering. Below the chamber were attached a titanium sublimator and a 500 l/s ion pump, both products of Perkin-Elmer. Viton-sealed, Series 10 VAT gate valves with bellows-sealed stems and metal seals to atmosphere isolated both the ion and turbo pumps.

Starting from atmosphere, the chamber was roughed through the turbo pump, with the ion pump sealed off. Baking, which would commence when the pressure reached  $10^{-6}\text{t}$ , was accomplished with Watlow heating tapes affixed permanently to the chamber with GE silicone RTV,

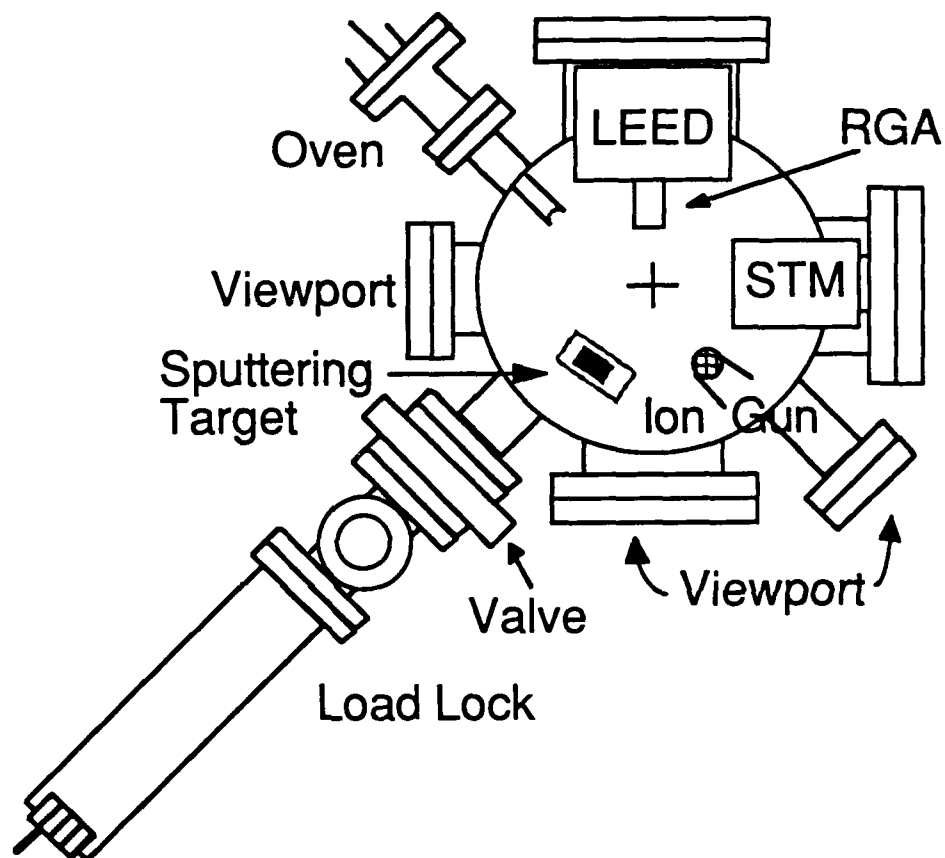


Fig. 2.19: Cross section of the vacuum chamber (Perkin Elmer Standard 21") with equipment for surface preparation and characterization. All components shown except the RGA and ion gun are in one plane, and the sample could be rotated in that plane. The manipulator shaft is normal to the cross.

and their temperatures were adjusted with Variacs. With the chamber covered by aluminum foil, the temperature was allowed to reach 125°C; higher baking temperatures were avoided because of possible damage to elastomer components in the STM. The ion pump was baked along with the chamber only if that pump's cleanliness was questioned; the disadvantage of including the ion pump in a bake was the longer time required for the chamber to cool to room temperature afterward. If only the turbo pump was baked with the chamber, then an 18-hour bakeout followed by 12 hrs. for temperature recovery were ordinarily sufficient to attain a pressure in the high  $10^{-11}$  range.

During roughing, the chamber pressure was initially measured by a Granville-Philips Convectron™ gauge. Pressures below 1  $\mu$ m were measured by a nude Bayard-Alpert type ionization gauge from Electronic Technologies. Contamination levels were displayed by a Leybold Quadrex 100™ residual gas analyzer with an electron-multiplier head. Detailed explanations of general vacuum practice and instrumentation are contained in a number of fine handbooks. (We79)

A load-lock system with a Thermionics bellows-sealed manipulator arm and a 50 l/s turbo pump allowed the introduction of samples without breaking the vacuum. Sample replacement could also accompany periodic removal of the STM to replace a tip.

A PHI ion gun was mounted pointing downward from one of the chamber's top ports for glancing-angle sputter cleaning of the samples. Following cleaning, the samples could be annealed resistively utilizing a 15A Ceram-a-Seal feedthrough mounted on a mini-port on the sample manipulator. The source of current was either a 10A dc regulated supply, or, when this power was insufficient, a Variac and a 10:1 step-down

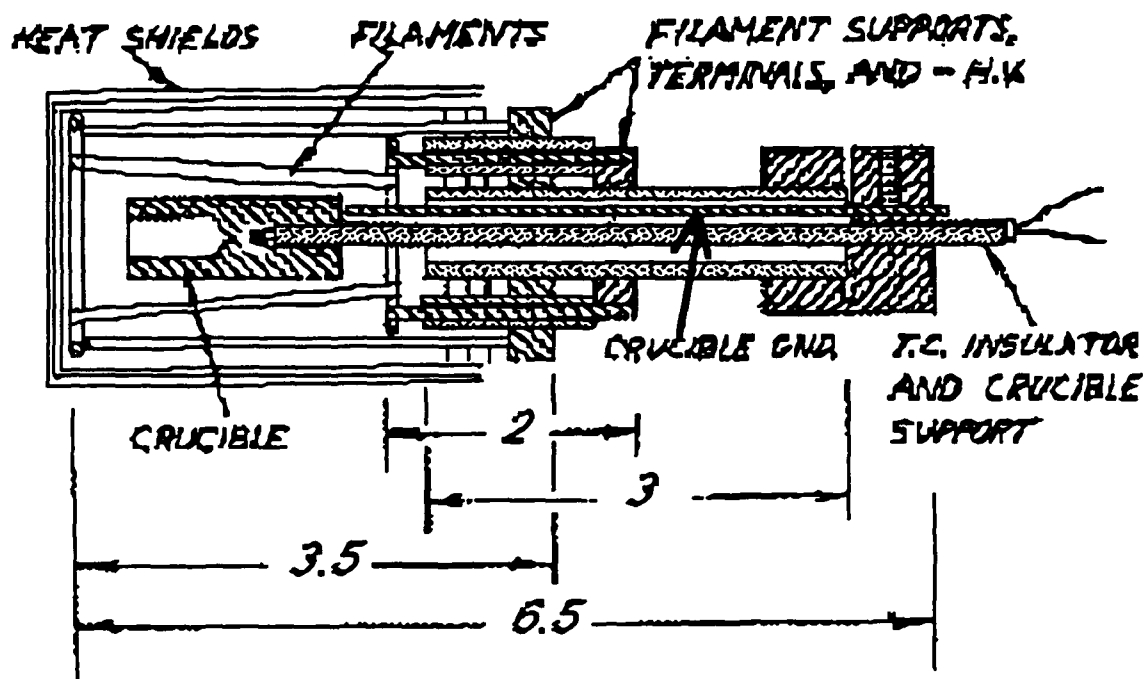


transformer. Current regulation offered stable biasing by preventing thermal runaway. Sample temperatures during annealing were measured by an Ircon Mod-Line™ infrared pyrometer, which covered the range of 500-1500°C.

The surface preparations of these studies required the capability of depositing gallium, boron, and silicon in vacuum. The first was accomplished with an oven on loan from AT&T Bell Laboratories, horizontally mounted on one of the chamber's 2.75" ports. Inside the chamber, the gallium vapor was confined to the sample's cross-section by a 6" copper pinch-off tube between port and sample. Within the oven, heating was accomplished with three tungsten filaments, and a small liquid N<sub>2</sub> trap maintained a stable pressure. (See fig. 2.20) The temperature of the oven was measured by a tungsten-5%-rhenium vs. tungsten-26%-rhenium thermocouple mounted behind the gallium crucible. Gallium was evaporated at 800°C, with  $\approx 10$ A filament current.

The boron sputtering target was mounted with tantalum clips on a platform that could be positioned in the path of the ion gun by a rotary feed-through. The platform also held a 10-25 mil. silicon wafer, cut .6x.2", which could be heated resistively as a simple evaporation source using a Variac, wired in series with five 3 $\Omega$ , 175W resistors to provide stable current biasing. A current of 4A was sufficient to heat the wafer to 1200°C for evaporation, as measured by the pyrometer.

A Huntington sample manipulator with secondary vertical adjustment was mounted on the top of the chamber, and the sample block could sit on copper arms mounted at the bottom of the manipulator tube. Two pairs of spring-loaded electrodes, one leading to a thermocouple and one to the sample, could be pressed tightly against connections on top of the block by



Dimensions in cm.

-  Ta
-  Stainless steel
-  Alumina

Fig. 2.20: Internal parts of the oven used for gallium deposition. The heat shields are Ta foil. (AT&T Bell Laboratories)

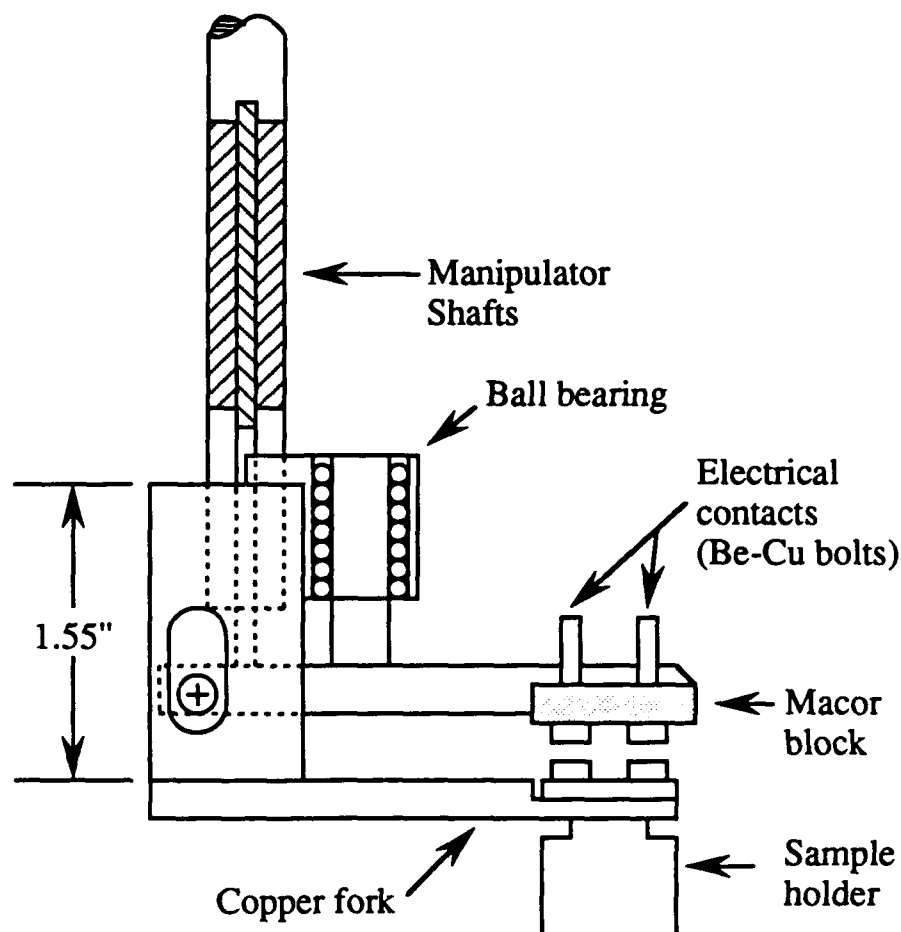
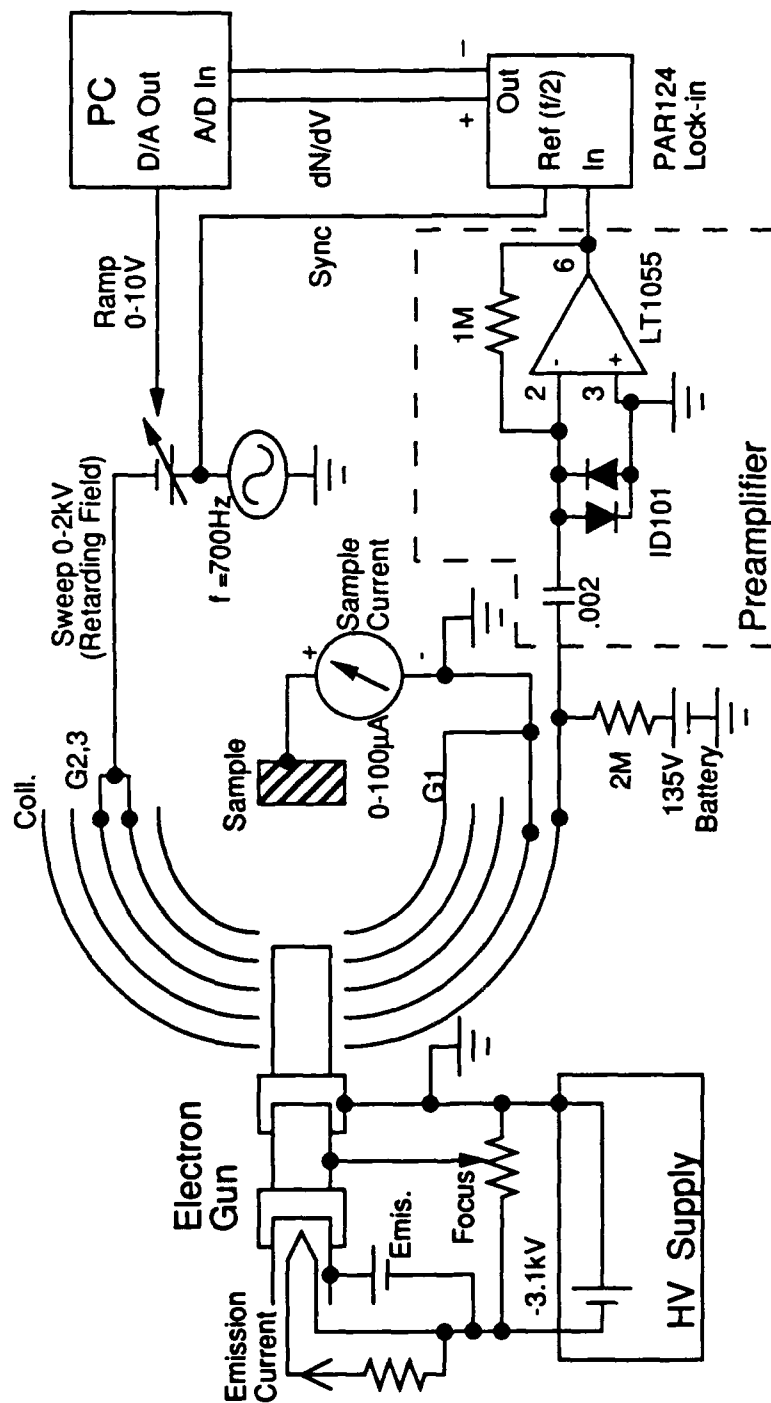


Fig. 2.21: Side view of the sample manipulator. The sample block was clamped by depressing the macor block through the secondary vertical motion in the shaft. The apparatus pictured could be rotated about the long axis of the shaft. Electrical leads and attachments for the cooling apparatus are omitted to emphasize the sample transport mechanism.

the manipulator's secondary 'z' motion. (See fig. 2.21) The pair of electrodes connected to the sample could be used for sample heating and for reading sample currents during sputtering, LEED, or Auger spectroscopy. Leads from both pairs of electrodes to feedthroughs on the manipulator were insulated by fiberglass sleeving and wrapped around the manipulator shaft. A liquid N<sub>2</sub> cooling coil from Vacuum Generators was also mounted on the manipulator and was filled during sample annealing to inhibit radiative heating of other elements of the chamber and accelerate sample cooling following preparation.

A PHI LEED unit was mounted on an 8" port to provide the essential determination of surface lattice periodicity before tunneling. The LEED, STM, oven, and sputtering target were all located in the same horizontal plane and could each be accessed simply by rotating the sample manipulator. In order to check for surface contamination following cleaning, the LEED optics were also employed as a retarding field Auger analyzer, as shown schematically in fig. 2.22. In this mode, the electron gun bias leads were still connected to the PHI LEED Electronics unit, but the filament bias was taken from a fixed, external 3.1kV supply as shown rather than the LEED unit's own variable bias. The beam was then controlled entirely with the emission and focus controls on the LEED chassis. Optimizing these controls generally resulted in a dc sample current of  $\approx 40\mu\text{A}$  through the meter shown.

Apart from two modifications, connections to the optics remained as for LEED. First, the Collector was connected to a preamplifier box, which contained the 135V battery. Second, the retarding voltage was applied to Grids 2 and 3. The battery prevents collector charging, and the preamp functions much as the tunneling preamp described in §II.3. As in the



## RETARDING FIELD AUGER SCHEMATIC

Figure 2.22

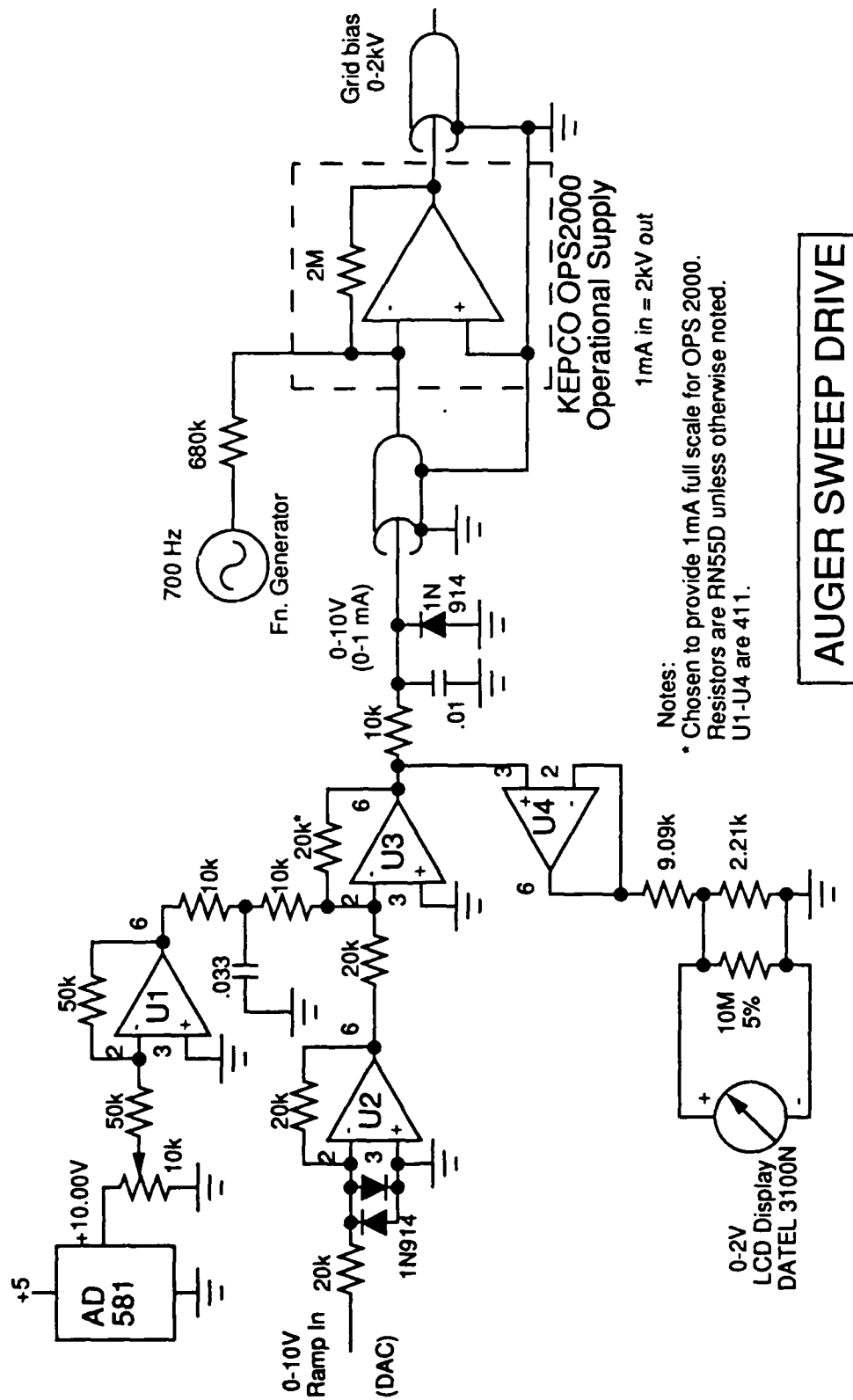


Figure 2.23

tunneling preamp, an additional  $\times 10$  stage follows the front end stage, so that the overall gain here is 10mV/nA (ac).

The range of practical retarding voltages extends to -1kV, though the electronics can drive a much higher range. The dc sweep is driven by one of the D/As on the DT2827 board in the PC, and superimposed on the sweep bias is a small modulation, typically 3V p-p. The spectra must reflect the second derivative of the signal; one derivative removes the secondary electron background, and a second is needed for any retarding field spectroscopy, which automatically produces an integrated signal. Accordingly, the lock-in detects the first harmonic of the modulation signal. With these parameters, the amplitude of the detected signal at the 92eV typically corresponded to 10nA rms. The noise level represented 10pA rms, so that the silicon peak to noise ratio was 1000:1.

The PC records and plots the lock-in output. Noise can be reduced from the spectra either by averaging repeated scans or by using the lock-in's output filters and scanning as slowly as .3V/s. The reliability of such slow scans is limited by the stability of gun current and focusing during the acquisition time.

The grid biasing circuit is shown in fig. 2.23. On the low-voltage side, the ramp generated by the PC is superimposed at U3's summing junction with a manual offset derived from a precision voltage reference. The instantaneous bias voltage is displayed on a digital panel meter driven by U4. The resulting 0-10V signal is amplified and inverted by a Kepco operational power supply to -2kV f.s., though in practice only the lower half of this range is used. The ac modulation is added at the supply's summing junction as shown.

We note that the low-voltage end of this circuit was designed for use with an arbitrary high voltage amplifier, before the OPS2000 was acquired. If that amplifier is used, most of the low-voltage circuitry shown becomes unnecessary, for the OPS2000 incorporates an internal reference. Thus, the computer-generated ramp can be fed directly into the OPS2000's summing junction, together with a variable offset produced simply by trimming the reference voltage with a pot.

## II.5 General Operating Procedure

### II.5.1 Preparation, characterization, and imaging

Samples are cut from 10-25 mil. Si(111) wafers with a diamond saw to fit the .5x.6" dimensions required by the sample holder. The first stage of cleaning is thorough degreasing by ultrasonic agitation in trichloroethylene, acetone, and methanol, in that order. Next, a controlled oxide is grown on the polished surface according to the chemical recipe in the appendix. The sample may then be mounted in the vacuum.

Tips were prepared by electrochemical etching of a .020" tungsten wire, with 15-30Vac applied between the wire and a copper braid in a 10% KOH solution. The technique established for field-ion microscope tip preparation is applied here. (Mu69)

Following a bakeout, the sample must be outgassed thoroughly at  $\approx 500^{\circ}\text{C}$ . Afterward, it can be heated to  $1050^{\circ}\text{C}$  for 2-3 minutes to remove the protective oxide and produce the  $7\times 7$  reconstruction. Highly doped, low-resistivity samples were used because of their reasonable voltage demand for resistive heating. Thus, for  $.04\Omega\text{-cm}$  wafers, the annealing temperature was reached with 10Adc at 60W. During sample preparation, the shutter to the STM is kept closed to minimize radiative heat transfer.



A sample could be recleaned any number of times in vacuum by ion sputtering. Ordinarily, 5-8 minutes of 1keV neon bombardment at  $5 \times 10^{-5} \text{t}$  sufficed. Neon was used because it would not contaminate the cold surface of the titanium pump.

After cleaning, the unreconstructed surfaces were checked for surface contamination with retarding-field Auger spectroscopy (§II.4). Fig. 2.24 displays an Auger spectrum acquired before any cleaning, immediately after shutting off a bakeout. Both C and O peaks are prominent, while the Si appears only as the oxide. Fig. 2.25, a spectrum acquired after a  $1000^\circ$  annealing, shows a pronounced, clean Si peak and greatly reduced C and O peaks. Subsequent sample cleanings in the same vacuum run must employ sputtering, and the spectrum of fig. 2.26 shows that after sputtering, the surface contamination level is comparable to that of fig. 2.25. We have obtained tunneling images reliably from surfaces estimated from such spectra to hold  $<2\%$  carbon, taking into account the Auger cross sections for each element. (Da76) A surface considered to be sufficiently clean could then be annealed as above to produce the  $7 \times 7$  diffraction pattern on the LEED apparatus. Fig. 2.27 displays an Auger spectrum acquired from such a reconstructed surface, showing distinctly lower contamination levels from the previous spectra. Deposition, as necessary, would take place at this point.

With liquid nitrogen flowing through the cooling coils, the sample block could be expected to reach room temperature within  $1/2$  hr. after annealing, after which it could be loaded on the STM and the coarse tip approach could commence. Tunneling with negligible thermal drift could typically begin six hours later.

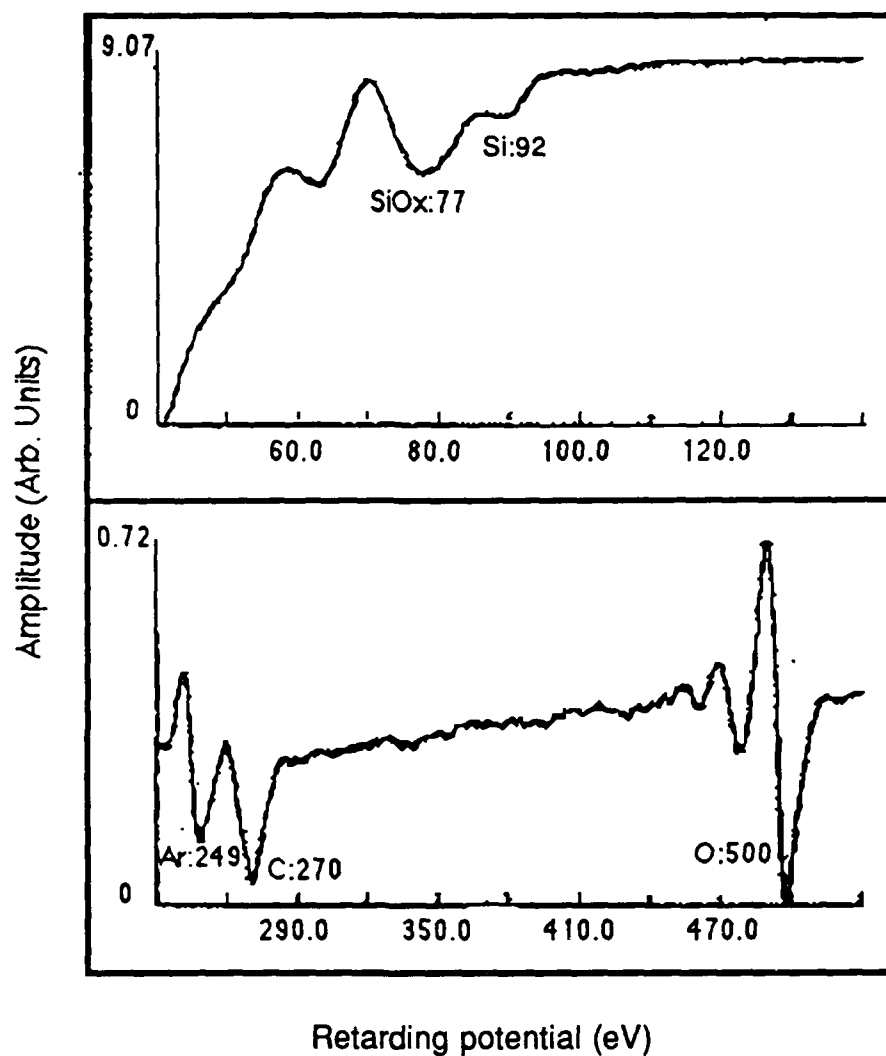


Fig. 2.24: Retarding field Auger spectrum of a Si(111) sample, acquired immediately after a bakeout and 600°C outgassing. The sample had previously been Shiraki-etched. The peak height ratio is Si(in SiOx):C:O:Ar:Si = 2.34:0.22:0.58:0.27:0.08

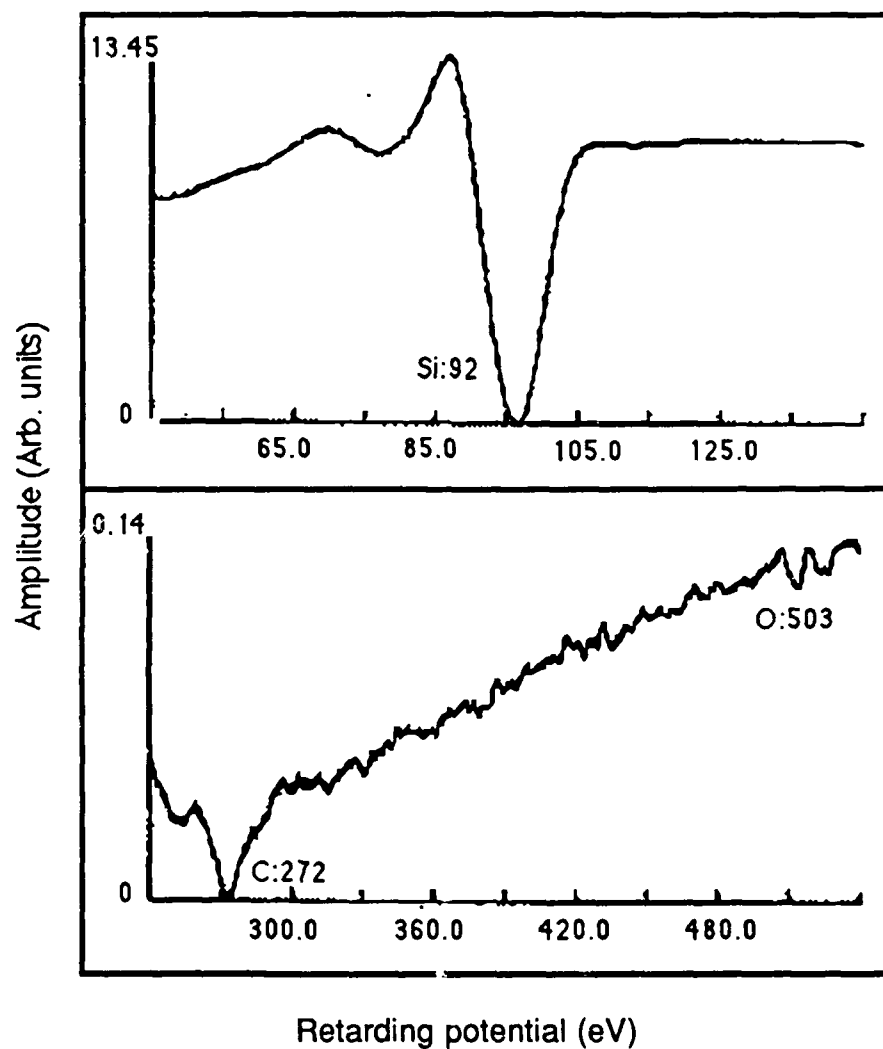


Fig. 2.25: Retarding field Auger spectrum of a Si(111)7x7 sample following a 1000°C annealing. The crystal had previously been Shiraki-etched. Peak height ratio is Si:C:O = 13.45:0.03:<0.01.

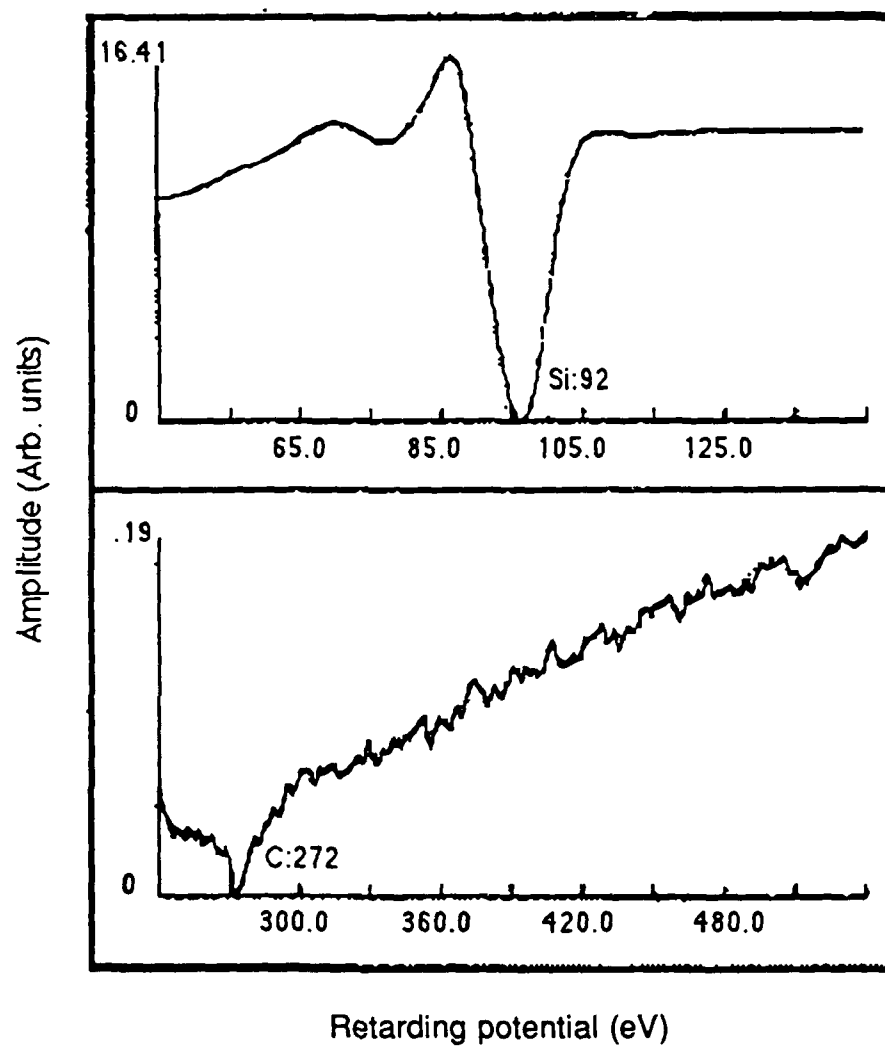


Fig. 2.26: Auger spectrum of an unreconstructed Si(111) surface following 8 min. of Ne ion sputtering at 1keV. Peak height ratio is Si:C = 16.41:0.03.

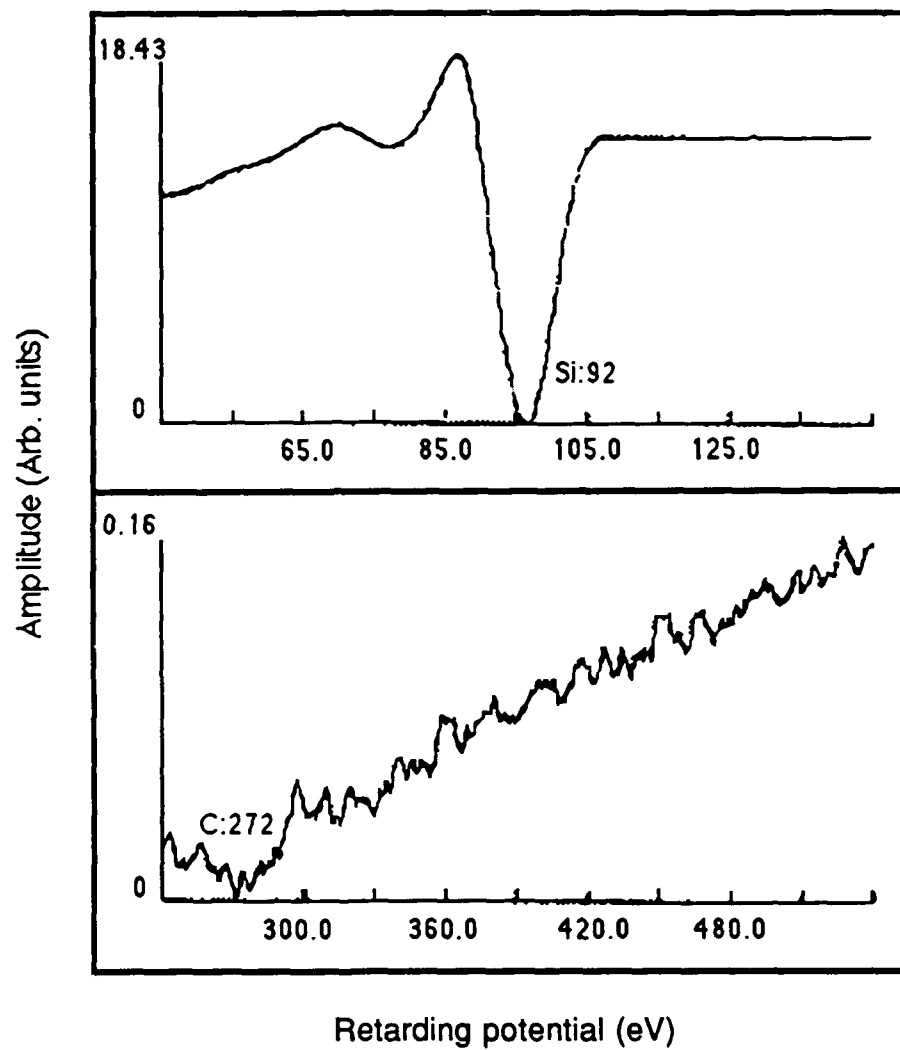


Fig. 2.27: Retarding field Auger spectrum of a Si(111)7x7 surface, following a full sputtering and annealing cycle.

The coarse tip approach using the louse was observed with a telescope outside the chamber and was halted when the visible separation between the tip and its reflection nearly vanished. At that point, a bias of -1kV was applied to the tip, and the louse was carefully moved in, with the feedback loop open, until a sample current appeared. Initial instabilities in the tip current usually decayed with further field emission. After the final step, each foot was clamped, and the tip was maneuvered by extending the piezo plate with the manual control while fine-tuning the voltages on the capacitive clamps. Once the louse was properly positioned, the scanner tube's z displacement was manually adjusted to a position at which bias conditions permitted the feedback loop to be closed. From this point onward, only the tip bias, tunneling current, and data offset level needed to be adjusted manually; the scanning functions were under software interface. If thermal drift caused the 'z' electrode to approach the end of its range, the piezo plate extension could be readjusted.

Images were displayed before the operator in real time and could be stored in the PC if desired. After the tunneling session, selected image files were transferred to a Silicon Graphics Iris 3000 workstation, which provided drift correction, three-dimensional modeling, filtering, and line cut displays using the DISPLAY v4.01 program developed at AT&T Bell Laboratories. Photographs were produced by a Matrix Instruments camera connected to the IRIS screen.

Figs. 2.28 and 2.29 display the adatoms of the famous silicon 7x7 reconstruction as imaged with the STM. The convention followed in the present work assigns a lighter shade of grey to greater retraction of the tip away from the surface. In the widely-held model for this surface to be

presented in §III.2, each protrusion that appears in the image as a local bright maximum is associated with an individual atomic site. Using such an image, the lateral displacements of the scanner tube could be calibrated with the known unit cell spacing of  $27\text{\AA}$ , as reflected in the periodicity of the LEED pattern. Likewise, the vertical displacement can be calibrated against single atomic steps in such images (fig. 2.30), which must have the (111) planar spacing of  $3.2\text{\AA}$ . (Be85b)

It is crucial to compare not only the distance scale but also the symmetry of the images with those of the LEED pattern, for a symmetry of the diffraction pattern that is apparently broken in the image may reflect a non-spherical tip rather than a property of the surface. Multiple tips provide a dramatic example of such a distortion, (Mi87, Pa87a, Pa88, Tr88) and can give rise to moiré patterns as in figs. 2.31 and 2.32. Fig. 2.33 shows a model for the construction of a multiple-tip image from two fully symmetric, but displaced images. The sharp boundary between distorted and normal regions in fig. 2.31 occurs near a step edge.

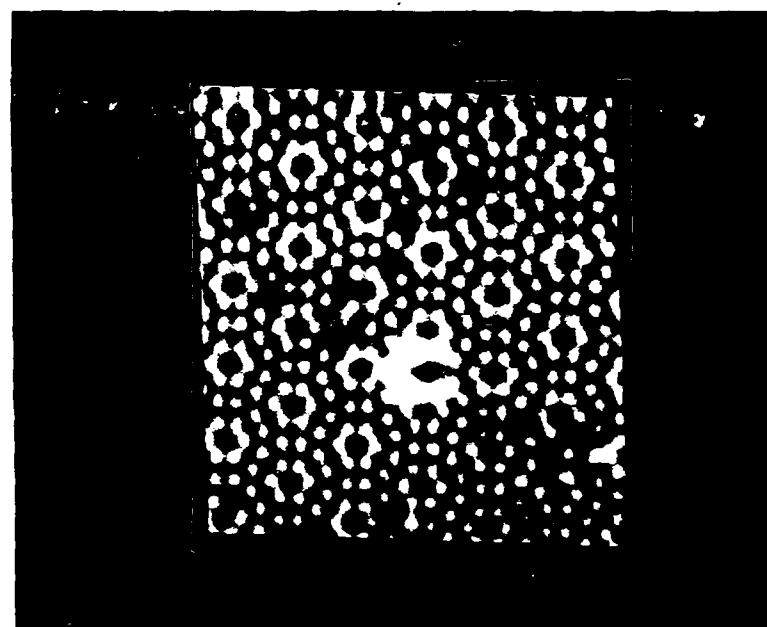


Fig. 2.28 130x130Å tunneling image showing the adatoms of the 7x7 reconstruction of clean Si(111). Tip bias = -2.0V, 1nA.



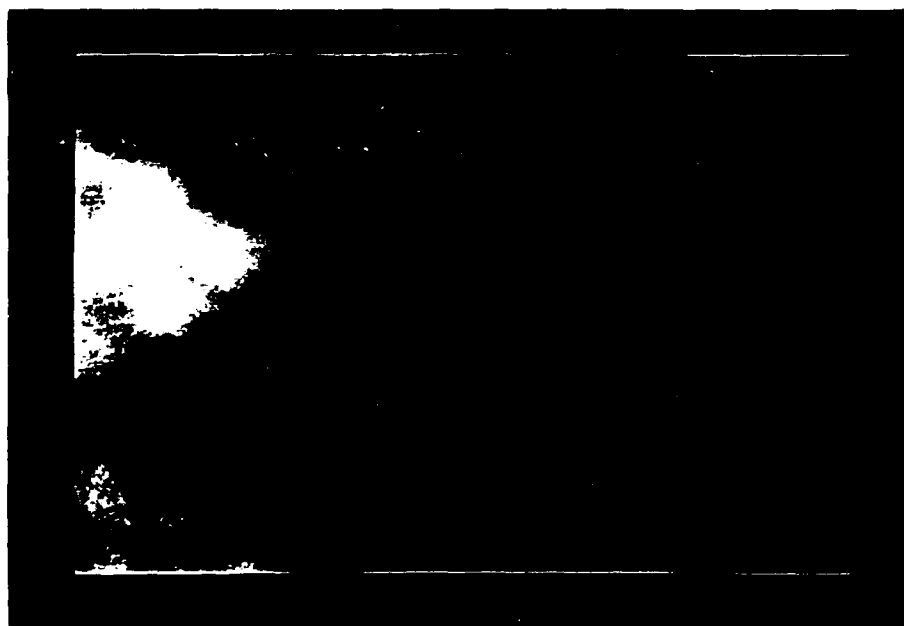


Fig. 2.29      A section of the 7x7 reconstruction, acquired at +1.8V tip bias and 1nA.

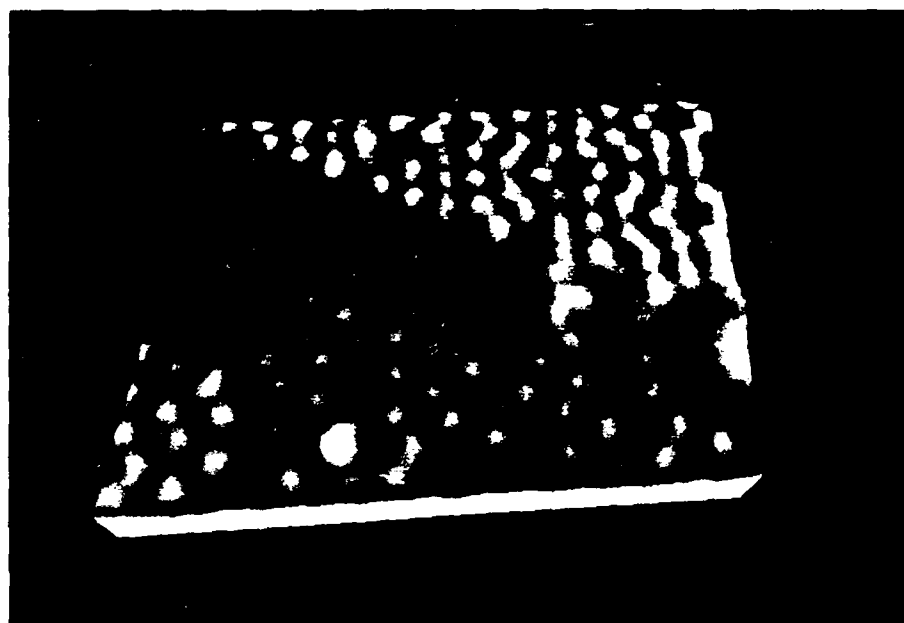


Fig. 2.30      A single atomic step in the Si(111)7x7 reconstruction, used to calibrate the vertical tip displacement. The step height is identical to the bulk (111) planar spacing, or  $3.2\text{\AA}$ .

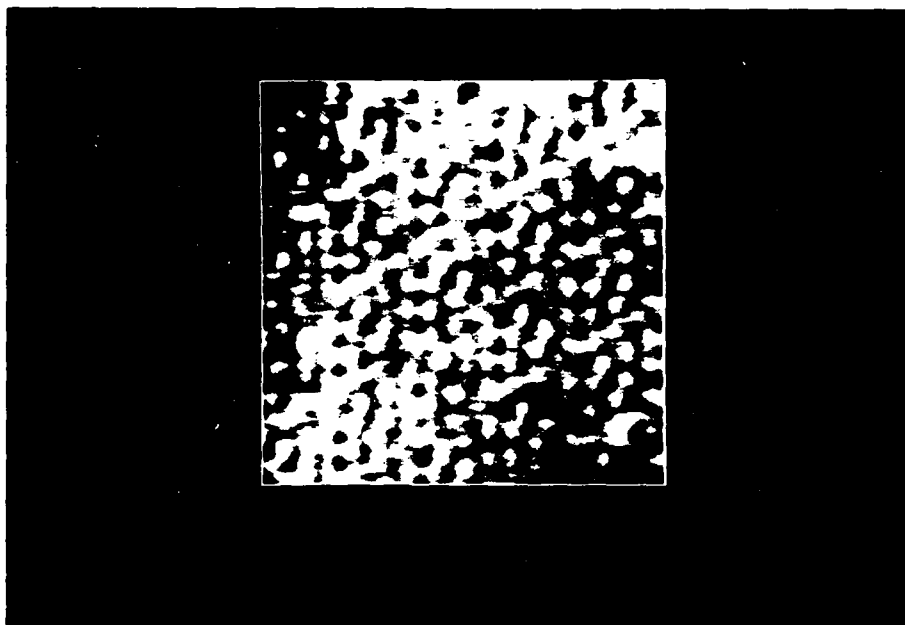


Fig. 2.31 Moiré effect in a  $100 \times 100 \text{ \AA}$ , multiple tip image of the  $7 \times 7$  reconstruction. Tip bias =  $-1.4 \text{ V}$ ,  $1 \text{ nA}$ .

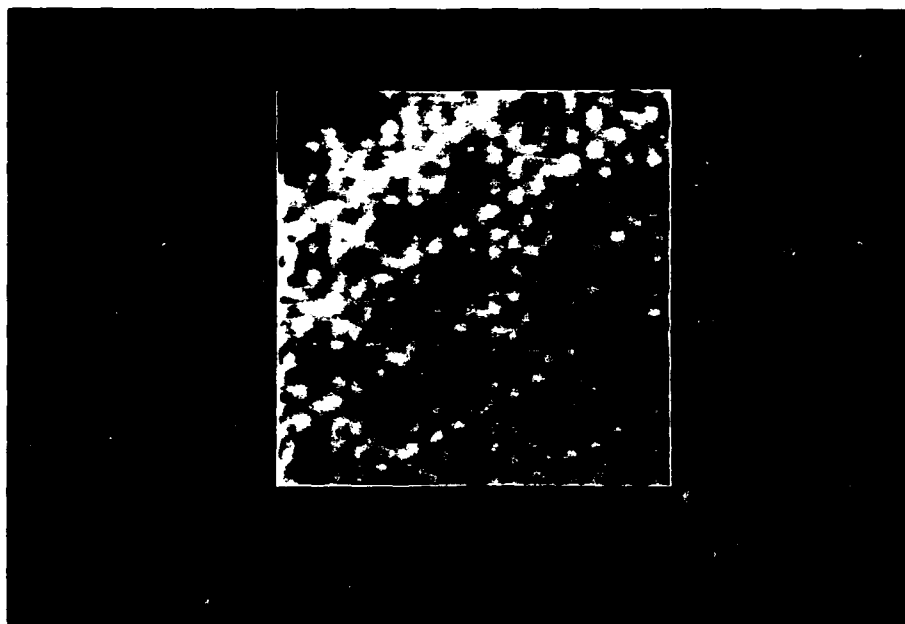
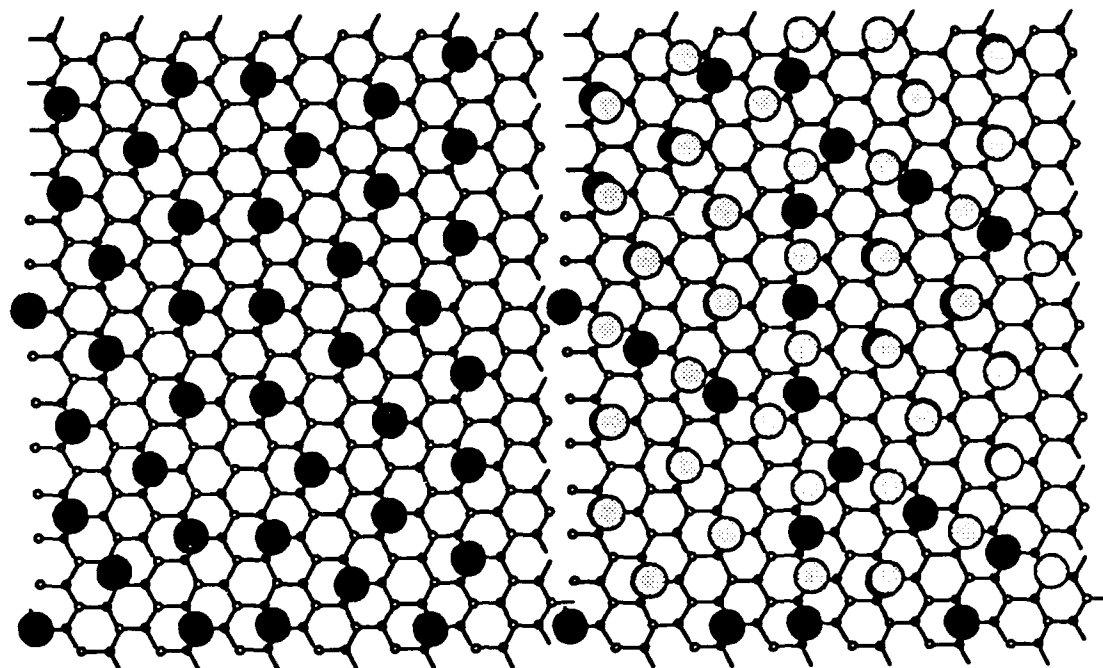


Fig. 2.32 As fig. 2.31, but with tip bias = +1.5V.



## Multiple tips

Fig. 2.33: Left, adatoms of the 7x7 reconstruction of Si(111), shown in black over a grid for reference. Right, two sets of adatoms, shown partially and fully shaded, spatially displaced from each other to simulate the effect of imaging with two tips simultaneously.

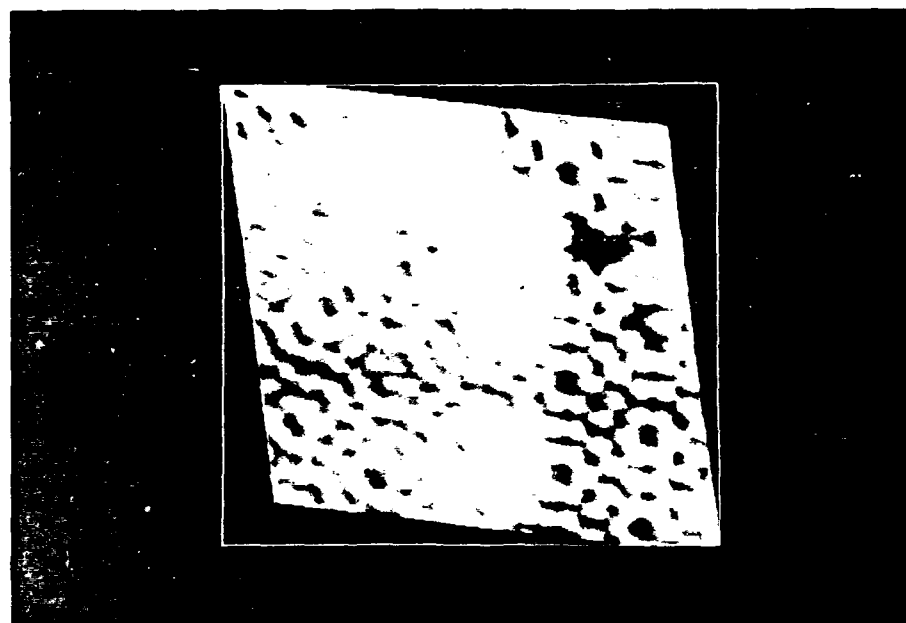


Fig. 2.34      The boundary between single- and double-tip regions occurs near an atomic step.

### II.5.2 Tunneling Spectroscopy

Two types of grey-scale images, differing not in their mechanism of acquisition but only in the parameter measured, are presented in the present work. Conventional topographs display the vertical tip displacement during constant-current scanning and therefore represent the incoming signal at A/D port 0 in fig. 2.18 on a gray scale. Differential conductivity images display the lock-in output signal, presented to A/D port 1 in that figure, as a function of lateral position. In both cases, the feedback adjusts the tip height in response to the current signal.

Tunneling spectra yield plots of  $dI/dV$  vs.  $V$ , which can then be normalized according to the considerations of §II.2. A sample, gated spectrum generated from a 7x7 surface is shown in fig. 2.35. The peak positions closely match those of previous reports, and their common association with surface state bands will be reviewed in §III.2. (No86, Ni87b)

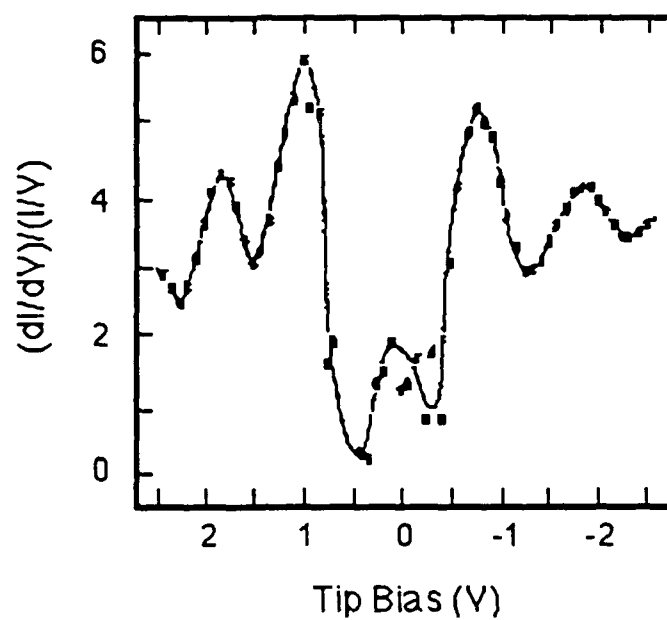


Fig. 2.35: Tunneling spectrum obtained from Si(111)7x7.



### **III.**

## **Chemisorption on Si(111)--Background**

### **III.1 Introduction**

The present chapter reviews previous experimental and theoretical investigations of the adsorption systems studied here, beginning with the model for the clean Si(111)7×7 reconstruction. Various diffraction and spectroscopic techniques have already been applied to gallium adsorption on Si(111). While comparatively little work has so far addressed boron adsorption, several contrasting behaviors of boron and gallium as adsorbates on Si(111) have already been identified, and we may anticipate finding further variety in a microscopic comparison of the two systems.

One of the motivations of our own experiments is the identification of atomic-level phenomena that give rise to the larger-scale behaviors previously observed and outlined in this chapter. A natural starting point is the determination of the origin of the diffraction patterns. The local electronic structure probed by STM can be also be compared with conventional band structure measurements, where available. When possible, we shall also correlate our experimental results with recent surface stress and energy calculations, which appear to be a very promising route to achieve at least qualitative understanding of the structures observed. Several observations to be presented in Chapter V suggest that information gained from local investigations may be used to prepare materials exhibiting unanticipated macroscopic properties.

### III.2 Surface Lattice Structures

It has long been recognized that atomically clean semiconductor surfaces do not generally adopt a perfect termination of the bulk lattice, but rather undergo an atomic rearrangement, or "reconstruction." (Za88) The local, covalent character of atomic bonding in semiconductors, in contrast to metals, leads to a tradeoff at semiconductor surfaces between energy gained by bond formation and energy lost through deformation. It is often difficult to predict the equilibrium reconstruction of a surface *a priori* because of both the small energy differences of competing microscopic processes and the generally large superlattice unit cells which involve many atoms. Nevertheless, recent theoretical advances now provide some microscopic understanding of the conditions that stabilize a number of reconstructions.

A starting point for most of the experiments of this work is the Si(111)7×7 surface. While the diffraction pattern for this structure was known for some time, (La63) a number of models consistent with the LEED results existed until STM images of that surface appeared. (Bi83) The current, widely-held model for that surface consistent with experiments to date (Ta85) is illustrated in fig. 3.1. Perpendicular to the (111) face is a stack of double layers. In the 7×7 reconstruction, the last complete layer of one half of the unit cell is a simple termination of the diamond structure, whereas in the other half, the bond directions in the top double layer are rotated by 60° about the normal to the surface, giving rise to the stacking fault. Faulted and unfaulted subunits are joined by the dimer bonds, and

# Si(111)-7x7

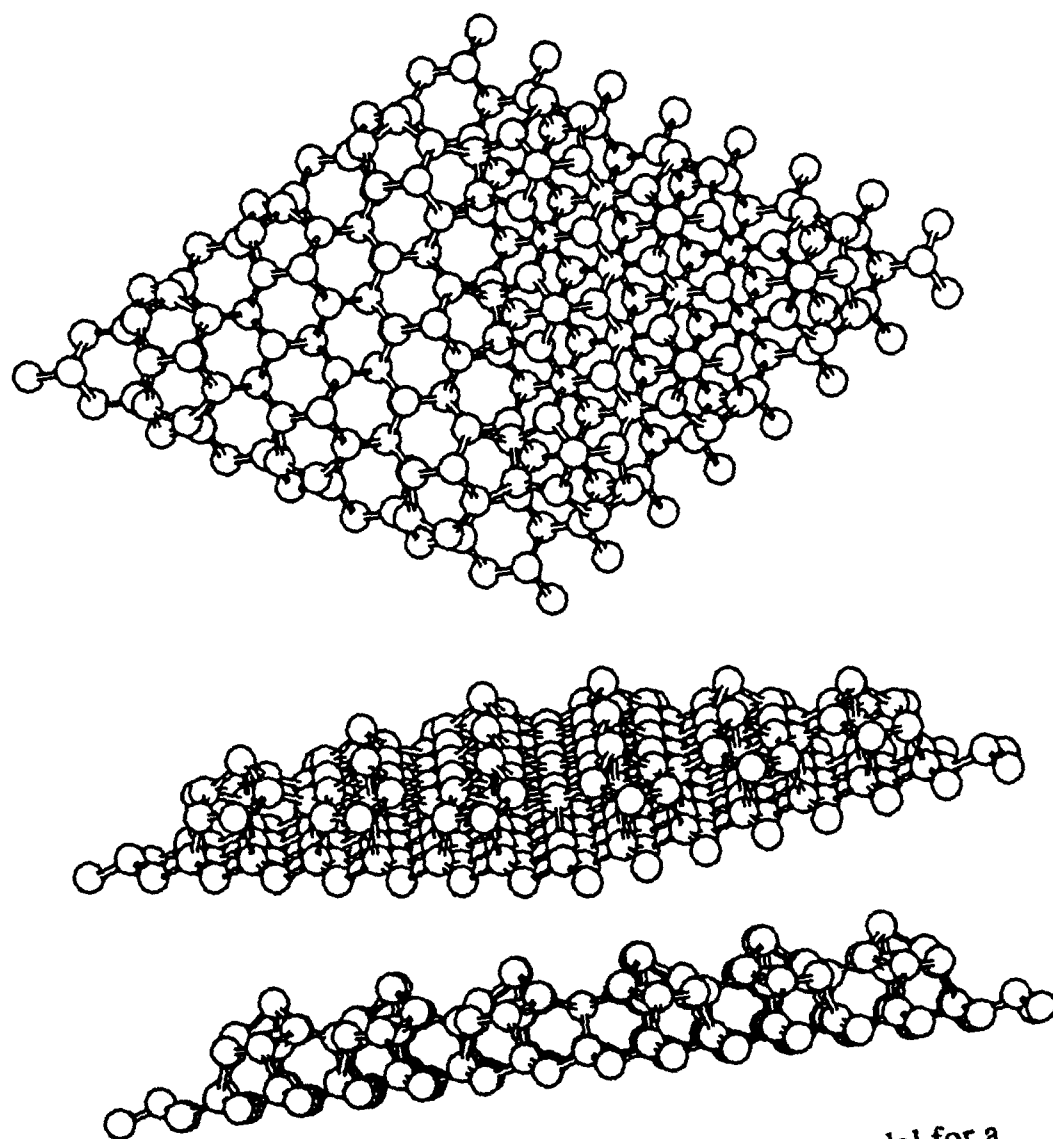


Fig. 3.1: Top, tilted, and side views of the DAS model for a unit cell in the 7x7 reconstruction, showing the twelve adatoms and the first two substrate double layers.

the vertices of different unit cells meet at corner holes. The twelve adatoms above this double layer each bind to three atoms in the upper, or rest atom, plane of the outer double layer in local  $2 \times 2$  subunits.

One consequence of the model is that the adatoms occupy only certain three-fold sites, for which a silicon atom in the lower plane of the first double layer sits directly underneath the adatom. Such a binding site ( $T_4$ ) for the adatom is to be contrasted with the three-fold "hollow" site ( $H_3$ ), which is alternatively available and has no atom directly underneath. STM studies have confirmed both the  $T_4$  binding position (Be85b) and the asymmetry in the unit cell resulting from the stacking fault. (Be85c, Tr86, Be89a)

This rearrangement removes many of the 49 dangling bonds of an unreconstructed area of similar size to the  $7 \times 7$  unit cell. In the reconstructed unit cell, one dangling bond sits on each of the twelve adatoms and the six rest atoms in the  $2 \times 2$  subunits. One additional dangling bond in every corner hole remains on an exposed atom of the second double layer, leaving a total of 19 dangling bonds per unit cell. The reduction in the number of dangling bonds from the perfect termination is a general property of semiconductor reconstructions and is thought to be one of the forces that drives such rearrangements.

It has been known for some time that the deposition of exactly  $1/3$  ML (1 ML =  $7.83 \times 10^{14}$  atoms/cm<sup>2</sup>) of Group III, trivalent metals on Si(111) results in the formation of a  $\sqrt{3} \times \sqrt{3} R 30^\circ$  surface lattice. (La64) In view of the preceding discussion, a natural adatom model for such a structure would place each trivalent atom above three silicon atoms in the last plane of outer

(111) double layer, completely terminating the dangling bonds of the unreconstructed, clean surface. Even this simple model admits two non-trivial alternatives for the lateral registration of adsorbed atoms with respect to the outer double layer, corresponding to the two types of three-fold binding sites indicated above. In one case, all of the adatoms would occupy hollow sites ( $H_3$ ); in the other case, filled sites ( $T_4$ ).

Fig. 3.2 illustrates the two alternatives. The first diagram of the figure represents the first double layer of an unreconstructed,  $1 \times 1$  substrate, where the outer atoms are shaded. A unit cell for this substrate is indicated. If one gallium adatom is to bind to three substrate silicons, then the diagram indicates that two inequivalent binding sites are available. Specifically, one of the threefold sites ( $T_4$ ) places the adatom directly above a silicon atom in the lower half of the first double layer, while the other available threefold adatom site ( $H_3$ ) does not.

For the case of gallium, comparison of surface bands measured by photoemission with those predicted from LDA calculations (Ni87a) have suggested that the filled site is favored, but direct evidence has been lacking. Conventional diffraction techniques have proven highly ambiguous in this case. For example, analysis of a single set of dynamical LEED data (Ka87, 88) recently led to two successive papers proposing very different geometries for adsorbed Ga. Analysis of STM and X-ray standing-wave results in this work will establish  $T_4$  adatom occupation of gallium conclusively.

Between  $1/3$  ML and 1ML gallium coverage, a RHEED study (Ot85) has reported several new periodicities that appear as the  $\sqrt{3} \times \sqrt{3} R 30^\circ$

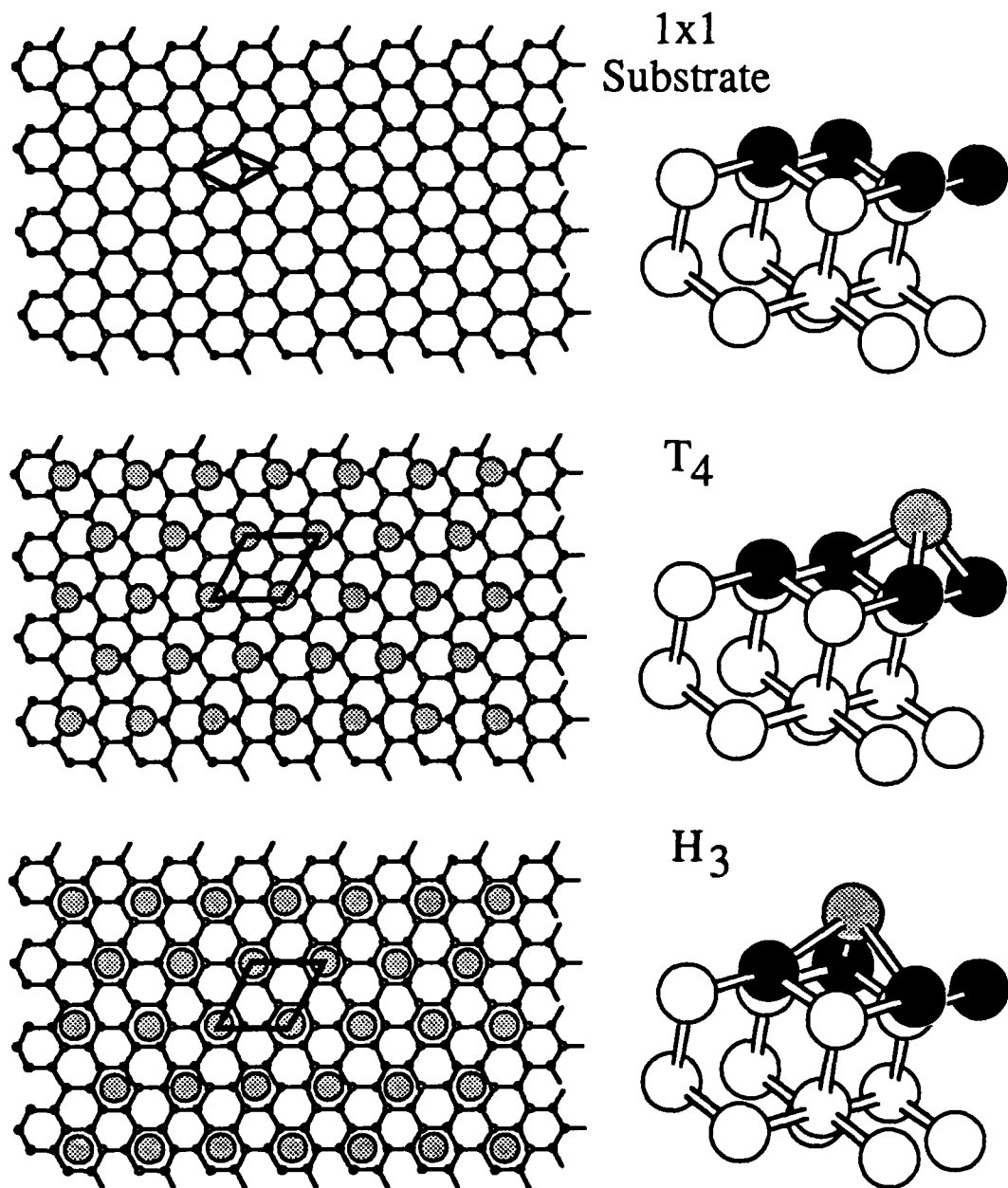


Fig. 3.2: (Top) Diagram of the outer double layer of an unreconstructed, 1x1 termination, with a 1x1 unit cell outlined. The outermost atoms in this layer are shaded solid. (Center)  $\sqrt{3} \times \sqrt{3} R 30^\circ$  structure with adatoms occupying the  $T_4$  site. The  $\sqrt{3} \times \sqrt{3}$  unit cell is outlined. (Bottom) As previous case, but with adatoms occupying the  $H_3$  binding site.

diffraction spots fade away. In particular, strong  $11\times 11$ ,  $6.3\times 6.3$ , and  $6.3\sqrt{3}\times 6.3\sqrt{3}$  spots have been observed. The associated structural transformation was reversible, for the  $\sqrt{3}\times\sqrt{3}$  pattern was reportedly recovered following gallium desorption by heating the sample below  $600^{\circ}\text{C}$ . Unlike the simpler  $\sqrt{3}\times\sqrt{3}\text{R}30^{\circ}$  structure, these new diffraction patterns originate from an *incommensurate* structure, meaning that the symmetry group of the adsorbate lattice is not, or is only accidentally, related to that of the substrate lattice. Consequently, the adsorbate coverage, expressed in monolayers, is an irrational quantity. Given the complexity of the various LEED patterns, it would evidently be quite difficult to deduce a surface structure from diffraction data alone. In fact, before the STM experiment was performed, there was *no* model for the Ga overlayer surface at all that accounted for *any* of the diffraction spots observed.

But incommensuration is interesting and worthy of examination in its own right. Incommensurate structures that recently attracted interest and have been determined experimentally include physisorbed rare gases on graphite by X-ray scattering (St84, Ho87), and charge density waves in chalcogenide layered materials by STM. (Co85, Sl86) Incommensurate chemisorbed adsorbate layers have not previously been imaged on a semiconductor surface. Such images would be desirable, however, because they would illustrate just how a surface accommodates competing adatom-adatom and adatom-substrate interactions. In fact, it will be shown below that the STM images can identify the real-space structure of the gallium overlayer. (Ch88)

Above 1 ML., Ga does not wet the Si(111) surface. Instead, a Volmer-Weber epitaxial growth mode, i.e. islands on a bare substrate, has been inferred from thermal desorption measurements. (Zi87b) Gallium islands on Si(111) have been photographed under the electron microscope, and their growth mechanism has been described as ripening. (Zi87a) While the details of island growth and ripening on the atomic scale are not within the scope of the present work, a satisfactory model of the various sub-monolayer gallium-induced surface structures must account for the cessation of smooth growth at 1ML that leads to the wetting problem.

While adsorption of 1/3ML of boron, another trivalent element, on Si(111) also yields the  $\sqrt{3}\times\sqrt{3}R30^\circ$  diffraction pattern, (Ko88a, Hi88) the resulting surface exhibits a number of sharp contrasts in both electronic and physical properties to the gallium-terminated surface. The differences in electronic properties, as revealed by tunneling spectroscopy, will be demonstrated in the subsequent chapters. Among the physical properties, we find that the Si(111) $\sqrt{3}\times\sqrt{3}R30^\circ$ -B surface is stable to prolonged (1 hr.) annealing at 1150°C, the upper limit of our sample heating capability. In contrast, above 650°C the LEED pattern of the Ga-terminated surface is obliterated, and above 850°C the surface reverts to the 7×7 reconstruction characteristic of clean Si. Furthermore, above 1/3 ML-B coverage no new diffraction patterns are encountered, and only islands are encountered in STM images. Unlike Ga, boron apparently does not form a uniform, ordered overlayer in the monolayer-coverage range.

Further differences in the behavior of the two adsorbate-covered surfaces have been revealed in a recent study of epitaxial Si growth on these



structures. (He89) It was reported there that room temperature deposition of .3ML of Si obliterated the  $\sqrt{3}\times\sqrt{3}$ R30° LEED pattern from the Ga-covered surface with no indication of gallium desorption by RBS or AES, so the gallium must have been redistributed randomly. In sharp contrast, deposition of 50Å of amorphous Si on Si(111) $\sqrt{3}\times\sqrt{3}$ R30°-B and subsequent *ex situ* X-ray analysis revealed  $\sqrt{3}\times\sqrt{3}$ R30° periodicity remaining at the buried interface, with no apparent degradation after exposure to air for several months.

Calculations of total energy and intrinsic surface stress are now routinely employed to gain at least qualitative understanding of the relative significance of the factors that determine the realization of competing surface geometries. These computations involve self-consistent density-functional calculations, with the exchange correlation energy treated in the local density approximation (LDA). (No84) The Hamiltonian is diagonalized in a basis of plane waves with kinetic energies below a finite cutoff, generally on the order of 12 Ry, and the atomic coordinates are relaxed to achieve the minimum energy configuration. Periodicity is enforced along the surface normal by employing alternating crystal slabs and vacuum along that direction, with inversion symmetry of atomic coordinates required in a slab. Surface stresses (Me88) are calculated in this geometry by applying established techniques of bulk stress calculations. (Ni85b)

Three important trends stand out from total energy calculations for clean Si(111). Table 3.1 displays recent results for various configurations of this surface, with substrate and adatom relaxations included. First, the presence

adatoms is favored over the unreconstructed surface because of the lower dangling bond density on the adatom-decorated surfaces. Second, while the  $T_4$  and  $H_3$  geometries are generally closer to one another in energy than either is to the unreconstructed surface, the  $T_4$  filling is preferred for Si, (No86) Al, (No84) and Ga (Ze89) adatoms on Si(111). Finally, an insulating surface layer is preferred to a metallic one. Thus, a termination all of the silicon substrate dangling bonds by trivalent metal adatoms in a  $\sqrt{3}\times\sqrt{3}R30^\circ$  geometries should be favorable. Si(7 $\times$ 7) adopts reconstructions with 2 $\times$ 2 subunits, which allow charge transfer from adatoms to neighboring rest atoms, leaving an insulating adatom filling.

While the favored reconstruction for a particular adsorbate and substrate does not necessarily minimize the average intrinsic surface stress, an excessively large stress may drive a rearrangement. It is desirable to understand the origin of the stress, for its sign and magnitude could affect the type of rearrangement. The convention is that a positive (negative) average stress,  $\sigma$ , indicates that the surface is under tension (compression) and favors contraction (expansion) of its lateral lattice constant.

Two trends indicated by intrinsic stress calculations are particularly pertinent to this work. (Me88, 89b) (See table 3.2) First, unreconstructed surfaces with substitutional Ga and Si atoms in the outer double layer are under compressive stress. The incomplete filling of the dangling bond orbitals of these atoms would favor  $sp^2$  hybridization, so the outer-layer atoms are expected to flatten their bond angles. The bond lengths must therefore shorten to maintain the transverse lattice constant. The table indicates that the effect is especially pronounced in the case of gallium

Table 3.1  
Some results of LDA total energy calculations for clean Si(111)  
(Ref: Me89a)

Structure	Energy (eV/1x1 cell) @ 12 Ry cutoff
1x1	1.39
$\sqrt{3}\times\sqrt{3}$ R30°-adatom, T <sub>4</sub>	1.18
2x2-adatom, T <sub>4</sub>	1.12
2x2-adatom, H <sub>3</sub>	1.23

Table 3.2  
Calculated stresses  $\sigma_{ii}$  for adsorbed Si(111) surfaces  
(Refs: Me88, Me89b)

Structure	$\sigma_{ii}$ (eV/1×1 cell)
Ga:Si(111), 1×1 substitutional	-4.45
Ge:Si(111), "	-1.12
As:Si(111), "	2.27
Si(111)	-0.54
Ga:Si(111), $\sqrt{3}\times\sqrt{3}$ R30°	1.35
Si(111), $\sqrt{3}\times\sqrt{3}$ R30°	1.70
Si(111), 2×2	1.66

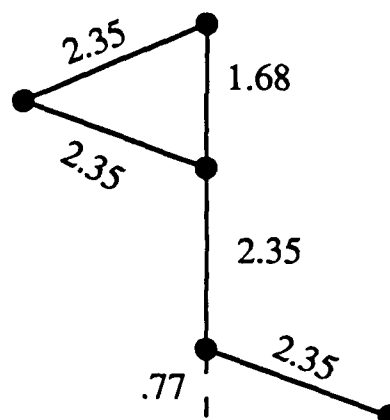
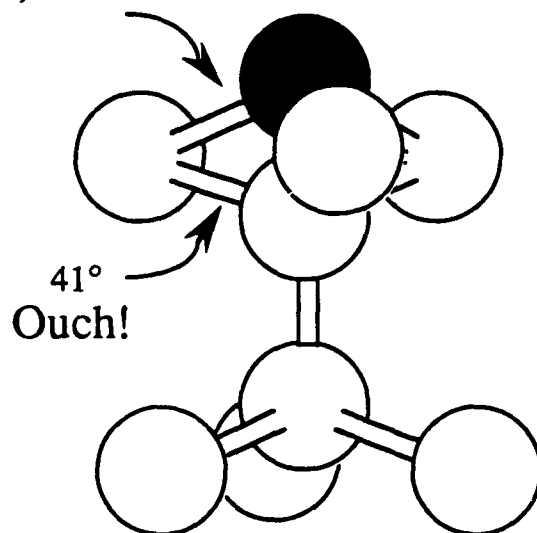
substitution, for the empty dangling bond orbital on gallium atoms would tend to favor rehybridization even more strongly than for silicon atoms.

The second point apparent from table 3.2 is that T<sub>4</sub> adatoms contribute tensile stress. Gallium or silicon atoms placed in an unrelaxed T<sub>4</sub> adatom geometry would have bond angles higher than the desired tetrahedral angles, so a relaxation would force the adatom and the second layer atom (see fig. 3.3) apart, with a consequent inward displacement of the adatom's neighbors in the first substrate layer. While this simple picture is applicable where the adsorbate and substrate atoms have comparable covalent radii, boron and silicon atoms have a substantial size mismatch. It is not necessarily expected that adsorbed boron would follow the pattern of T<sub>4</sub>-adatom occupation that has been firmly established for gallium( $\sqrt{3}\times\sqrt{3}R30^\circ$ ) and silicon(7x7), and alternative geometries will have to be considered for Si(111) $\sqrt{3}\times\sqrt{3}R30^\circ$ -B.

We also note that the application of the methods and general considerations presented above is constrained by present limits of computing power and cannot accommodate arbitrarily large unit cells. In particular, these methods alone are not at present sufficient to determine the relative stabilities of the various  $(2n+1)\times(2n+1)$  DAS models. Strong arguments for the energies and surface stresses of these reconstructions have been advanced, however, employing estimates of energies and stresses contributed by the various components of the surface unit cell, i.e., adatoms, faults, domain walls, etc. (Va88) Such work suggests that the driving force behind such reconstructions is the negative energy for domain

## T<sub>4</sub> Gallium Relaxation

(a) Unrelaxed



(b) Relaxed

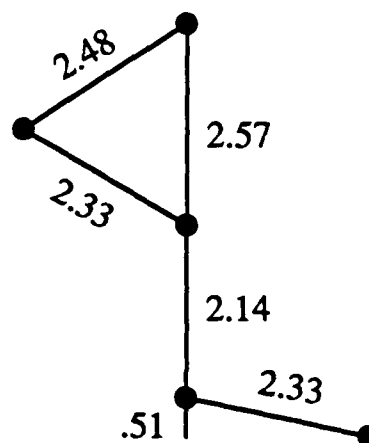
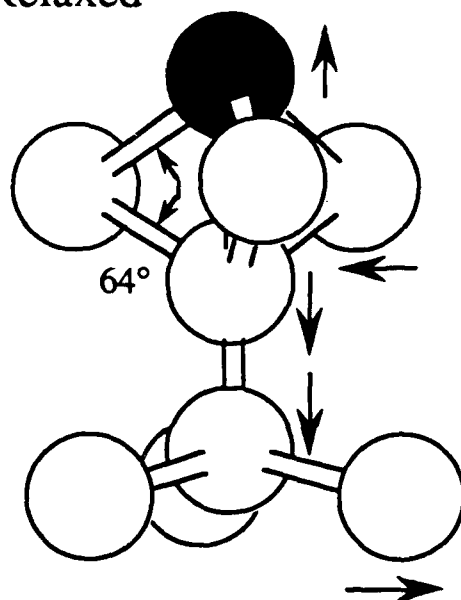


Fig. 3.3: Topology of Ga adatoms (shaded) in the T<sub>4</sub> site in  $\sqrt{3}\times\sqrt{3}$  surface structures. (a) Unrelaxed coordinates, obtained by setting all bond lengths equal to the sum of bulk covalent radii. (b) Relaxed atomic coordinates, from Ka88.

wall formation, with consequent dangling bond reduction. The precise configuration realized is determined by balancing the energetic contributions associated with the dimers as well as corner holes, stacking faults, and dangling bonds.

On the DAS surfaces, the lateral pull of the domain walls results in a lateral expansion of their  $2 \times 2$  subunits, which is partially counterbalanced by the intrinsic tensile stress of those  $2 \times 2$  subunits. While the stresses of the DAS unit cells do not by themselves determine the equilibrium reconstructions in this model, an externally applied strain could still alter the reconstruction. In this picture, the large intrinsic tensile stress associated with the dimer walls causes the equilibrium average tensile surface stress of  $(2n+1) \times (2n+1)$  surfaces to increase for lower  $n$ . Lateral compression of the  $7 \times 7$  surface might therefore be expected to induce the  $5 \times 5$  structure.

It will be shown in the subsequent chapters that the broad theoretical principles stated above are useful in achieving an understanding of the conditions under which new structures identified by STM might be expected to appear. The results of specific calculations that pertain to particular experiments in this work will be presented and discussed along with the experimental results.

### III.3 Surface Band Structure

The surface state band dispersions associated with the  $\text{Si}(111)7 \times 7$  reconstruction and with a number of trivalent-metal-induced  $\sqrt{3} \times \sqrt{3}R30^\circ$  surfaces have been investigated in detail by angle-resolved ultraviolet

photoemission spectroscopy (ARUPS) and inverse photoemission (KRIPES). The results of these studies may be compared with LDA band structure calculations for a number of these systems, and fig. 3.4 displays a number of recent theoretical and experimental results.

From simple electron counting, adatoms on Si(111)7×7 contribute four valence electrons each. Three of these should each be expected to participate in one covalent bond with a substrate atom in the first double layer (atoms 2, 3, and 4 in fig. 3.3), leaving one electron and one dangling orbital pointing normal to the surface, into the vacuum. One rest atom per unit cell also contributes one electron and one dangling orbital, so after hybridization, there should be three new occupied surface bands corresponding to the three new, inequivalent types of occupied electron orbitals. Charge transfer from the adatom to the rest atom orbital would then lower the energy of the band that has a higher wavefunction overlap with the rest atom than with the adatom.

These three bands have been identified by ARUPS (Uh85) (see fig. 3.4), and their positions and dispersions are in close agreement with the results of LDA slab calculations. (No86, Me89a) The fully occupied state  $\approx 2\text{eV}$  below the fermi level ( $S_3$ , or "back-bond") is believed to arise from the bonding of the Si adatom to the first layer substrate atoms. The rest atom band ( $S_2$ ) of a 2×2-type surface is found  $\approx 1\text{eV}$  below the fermi level. Finally, the narrow band ( $S_1$ ) at the fermi level is thought to originate from the partially-occupied dangling bond orbital atop each adatom. An unoccupied state ( $U_1$ ) within 0.6eV of the fermi level is thought to originate from the partially unoccupied character of the adatom dangling orbitals.



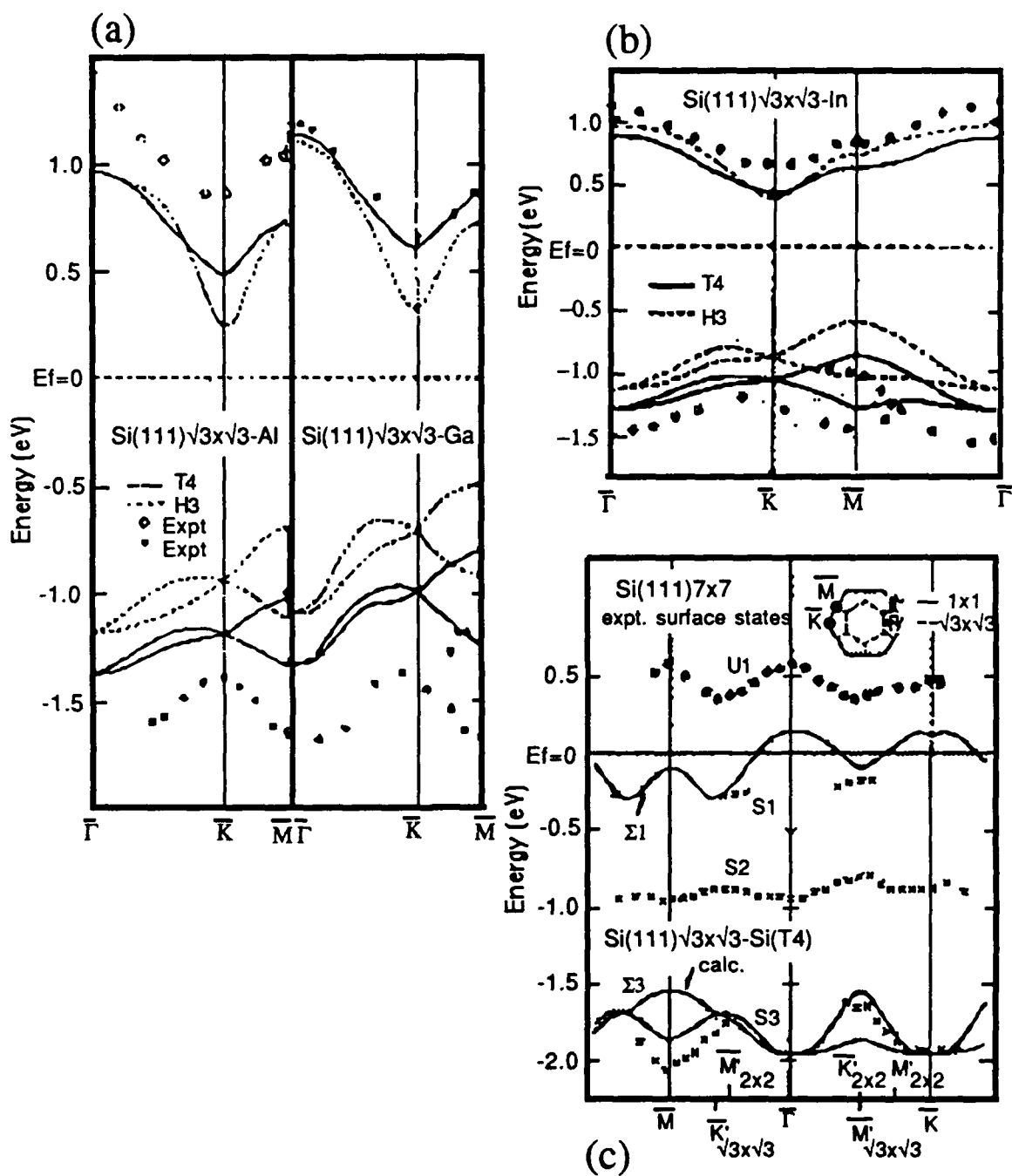


Fig. 3.4: Measured and calculated surface bands for the systems indicated, from (a) Ni87a; (b) Ni85a; (c) Ni87b, No86

The tunneling spectrum of fig. 2.35 may now be interpreted in light of these surface bands. According to the convention used in this work, negative tip bias corresponds to tunneling of electrons into empty surface states. The peak at -0.6V tip bias is thought to arise from the  $U_1$ -type adatom band, and the peak at 1.9V tip bias may be associated with the occupied, back bond states. The sharp peak at 1 V tip bias has previously been identified as comprising contributions from both the  $S_1$  adatom state and the  $S_2$  rest atom state. (Be89a)

Also shown in fig. 3.4 is a compilation of experimental and theoretical results for the surface band structures of Al-, Ga-, and In-terminated Si(111) surfaces in the  $\sqrt{3}\times\sqrt{3}R30^\circ$  structure, which resemble each other quite closely. (Ni87a,b) In each case, the fully occupied band  $\approx 1.5$ -2eV below the fermi level has been associated with the "back-bond" orbitals, as on the  $7\times 7$  surface with silicon adatoms. A wide, fully-unoccupied band ( $U_1$ ) appearing at 0.8-1.3eV above the fermi level is strongest at  $k_{||}=0$  and arises from the adatom dangling bond orbital. Thus two features distinguish the similar band structures of these trivalent-metal-terminated surfaces from that of the  $7\times 7$  reconstruction. First, the rest atom, or  $S_2$ , band found on the latter structure is absent from the Al-, Ga-, and In-terminated surfaces because the geometry of their  $\sqrt{3}\times\sqrt{3}R30^\circ$  structure leaves no rest atoms. Second, the adatom dangling-bond band which lay close to the fermi level in the  $7\times 7$  reconstruction ( $S_1$ ) is replaced in the  $\sqrt{3}\times\sqrt{3}R30^\circ$  structures by the fully empty band ( $U_1$ ). This point

might have been anticipated from the electron deficiency of the trivalent elements relative to silicon.

One KRIPES investigation of the  $\text{Si}(111)\sqrt{3}\times\sqrt{3}\text{R}30^\circ\text{-In}$  surface revealed a small low-lying unoccupied peak near the fermi level, similar in dispersion to that of the clean  $\text{Si}(111)7\times 7$ . (Ni85c) Since the LEED pattern in that work did not exhibit any trace of  $7\times 7$  periodicity, it was surmised that the low-lying empty state signal resulted from silicon adatoms present as defects in the surface layer. This conjecture could not be verified directly by such an experiment, which averages spectroscopic information over a region much larger than an area of atomic dimensions. In order to detect a band shift within such an area, a technique which is sensitive to surface electronic structure on the atomic scale is required. Because of the localized nature of the adatom dangling-bond orbital, (Me89a) it might be expected that the position of this orbital relative to the fermi level would enable the STM to distinguish Si adatoms from trivalent metal adatoms within an inhomogeneous surface that incorporates both Si adatoms and either Al-, Ga-, or In adatoms mixed in a  $\sqrt{3}\times\sqrt{3}\text{R}30^\circ$  structure.

In fact, such an analysis employing local tunneling spectroscopy was recently undertaken for the Al-terminated  $\text{Si}(111)$  surface, with promising results. In a series of reports, it was first demonstrated that tunneling spectra of the  $\text{Si}(111)7\times 7$  and the  $\text{Si}(111)\sqrt{3}\times\sqrt{3}\text{R}30^\circ\text{-Al}$  surfaces differ from each other, while specific features of each of the two spectra were identified with bands previously observed by photoemission. (Ha88a) Later, the feasibility of creating an inhomogeneous  $\sqrt{3}\times\sqrt{3}\text{R}30^\circ$  surface, on

which both Si and Al adatoms could be identified by STM, was established. (Ha88b)

While dramatically different tunneling spectra reportedly resulted from positioning the tip over Si or Al adatom cells, the detailed interpretation of these spectra in terms of surface bands is not yet fully resolved. (Mu89) In particular, the reported Si spectrum did *not* reveal an unoccupied,  $U_1$ -type band near the fermi level, and it was pointed out that the appearance of spectra acquired over Si adatoms can depend strongly on the bonding environments of the various systems in which Si adatoms are found. (Reply to Mu89) Apparently, the Al/Si-terminated Si(111) surface did not unambiguously reveal a local variation in the position of the dangling bond orbital from that which is characteristic of clean, Si-terminated surfaces up to that which is characteristic of the Al-terminated surface. In contrast, we shall see that tunneling spectroscopy of the inhomogeneous, B-terminated  $\sqrt{3}\times\sqrt{3}R30^\circ$  surface does indicate both  $S_1$ - and  $U_1$ -type states localized on both Si and B sites.

#### III.4 Group III Adatoms--Summary of Previous Work

In light of the absence of boron data in fig. 3.4, we now examine the general context of Group III adsorption systems. Table 3.3 summarizes the experimental and theoretical studies to date of the structure and energy bands of various Group III adsorbates on Si(111) in the  $\sqrt{3}\times\sqrt{3}R30^\circ$  structure. The aluminum-, gallium-, and indium-terminated surfaces have all been imaged under the STM, and their surface band dispersions have been determined experimentally.  $T_4$  adatom occupation of gallium is a

Table 3.3:

$\sqrt{3} \times \sqrt{3} R 30^\circ$  Induced  
on Si(111)

Group III

B
$r = 0.80 \text{ \AA}$
Al
$r = 1.25 \text{ \AA}$
Ga
$r = 1.25 \text{ \AA}$
In
$r = 1.50 \text{ \AA}$

STM: Ha88b  
UPS, IPS, Theory: Ni87a

X-ray standing waves, STM, Theory: Ze89  
STM: No88  
UPS & IPS: Ni87a

STM: No87  
Theory, UPS, IPS: Ni87a

subject of this work, and will later be demonstrated conclusively. For the aluminum- and indium-terminated surfaces, the  $T_4$  adatom structure is strongly favored by theoretical energy-minimization considerations. Moreover, the measured U1 band in each case lies closer the predicted band for the  $T_4$  structure than for the  $H_3$  structure. It was also noted above that Si adatoms on Si(111) assume a  $T_4$  structure.

The apparent generality of the phenomenon of  $T_4$  adatom occupation might therefore make a study of the boron-terminated surface at first seem repetitious. In fact, table 3.3 indicates that the extensive body of investigations of Al, Ga, and In adsorption is complemented by relatively little work on boron adsorption. Still, there is cause to question whether boron will follow the pattern established by its Group III cousins. Covalent radii, which were shown in §III.2 to play a central role in the binding topology are listed for each element in the column. (Ma75) Compared with boron, the radii of Al, Ga, and In only deviate slightly from one another and from silicon, and they might all be expected to display similar adsorption behavior. Boron is a considerably smaller atom, so an investigation of the  $Si(111)\sqrt{3}\times\sqrt{3}R30^\circ$ -B system would test both the apparent generality of  $T_4$  adatom binding under new conditions and the predictive power of theoretical considerations that are commonly invoked.

## IV. Gallium adsorption on Si(111)

### IV.1 Coverage below 1/3 ML

#### IV.1.1 Sample Preparation

The starting point for the experiments described in this chapter is the clean Si(111) surface, prepared with the  $7\times 7$  reconstruction according to the procedure of §II.6. In this experiment, the samples were cut from a polished,  $.04\Omega\text{-cm}$  As-doped Si(111) wafer. An image of this reconstruction is needed to determine the lateral distance scales of the  $x$  and  $y$  piezo transducers, for ultimately all distance scales derive from the diffraction pattern. Thus, the spacing between unit cells of the  $7\times 7$  surface must be  $26.9\text{\AA}$ , or seven times the  $1\times 1$  spacing of  $3.84\text{\AA}$ . The resulting distance calibration can later be applied to a new surface of undetermined structure.

A clean Si(111) surface that yields a sharp  $7\times 7$  LEED pattern is ready for gallium deposition, according to the procedure introduced in §II.6. Gallium is evaporated by heating the oven to  $800^\circ\text{C}$  with a dc current through the oven's filaments. With the sample held at  $\approx 400^\circ\text{C}$  before the oven's orifice, the  $\sqrt{3}\times\sqrt{3}R30^\circ$  diffraction pattern characteristic of 1/3 ML gallium coverage ( $\text{La}64$ ) appears after  $\approx 2$  minutes of evaporation. A sharpening of the diffraction pattern may occur if the sample heating is maintained for  $\approx 1$  additional minute.



Fig. 4.1 Tunneling image of Si(111) $\sqrt{3}\times\sqrt{3}$ R30°-Ga, showing adatoms spaced 6.7Å apart. Tip bias = -1.4V, 1nA.



Following sample cooling to room temperature, examination of the surface under the STM produces images such as fig. 4.1. Using the calibration of the lateral distance scale from  $7\times 7$  images, we find that the spacing between protrusions in fig. 4.1 is  $6.7\text{\AA}$ , which corresponds to the  $\sqrt{3}\times\sqrt{3}R30^\circ$  periodicity observed under LEED. It appears that, just as on the silicon  $7\times 7$  surface, the gallium-induced  $\sqrt{3}\times\sqrt{3}R30^\circ$  structure is terminated by adatoms.

This observation might have been anticipated on the basis of the trivalency of gallium. If the adatom layer consists of gallium atoms seated on a relaxed,  $1\times 1$  silicon substrate, then a structure such as appears in fig. 4.1 would completely terminate all of the dangling bonds of the substrate. Nevertheless, the tunneling image itself does not prove that the observed adatoms are actually gallium. Such chemical information is not provided by STM and must be acquired by an independent measurement of the vertical position of the impurity.

The technique of X-ray standing-wave interferometry (Go74, Pa86) provides the vertical position of the impurity relative to the extrapolated bulk planes that lie parallel to the surface. In order to address the question of gallium adatom occupation, such an experiment was performed in conjunction with the present work, (Ze89) with the results displayed in fig. 4.2. The measured quantities represented by the data points are the gallium fluorescence yield and the Bragg reflectivity of Mo  $K\alpha$  incident radiation. From these are extracted both the position of the gallium atoms relative to the bulk planes ( $P$ , in dimensionless units), and the coherent fraction ( $F$ ), by

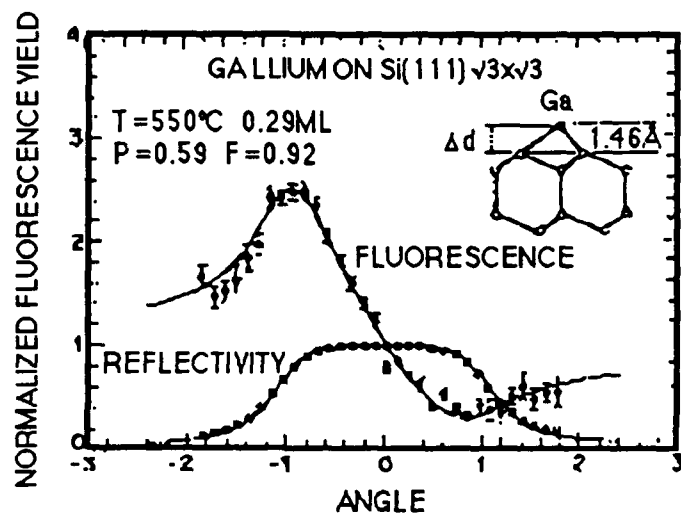


Fig. 4.2: Reflectivity and fluorescence yield for Ga on Si(111)- $\sqrt{3}\times\sqrt{3}$ R30°, from X-ray standing wave interferometry. Inset shows [110] projection of (111) planes with Ga in the T4 geometry.

fitting the data to dynamical theory according to these two adjustable parameters. The measured Ga height of  $1.46 \pm 0.03 \text{ \AA}$  above the extrapolated outer layer as shown, together with the high coherent fraction of 0.97, establishes adatom occupation by Ga on Si(111).

The vertical position of the Ga adatom can, and must, therefore be established independently of STM. Nevertheless, we shall see that the structure of the Si(111) $\sqrt{3} \times \sqrt{3} R 30^\circ$ -Ga surface is not determined completely from the data presented so far. In particular, the relationship of the adatom layer to the substrate remains undetermined.

#### IV.1.2 Registry from STM

The remaining ambiguity in this surface structure concerns the binding site of the Ga adatoms on the substrate, with the possible alternative structures as described in §III.2. The two binding configurations of fig. 3.2 are inequivalent, yet either one could give rise to the tunneling image of fig. 4.1. Tunneling microscopy can still be employed, as follows, to determine which of the two structures of fig. 4.2 is actually realized. We have seen (§II.5) that there is a surface, the Si(111)7×7 reconstruction, which can be prepared easily and within which T<sub>4</sub> occupation by Si adatoms has been established. Therefore, if a surface can be prepared which incorporates domains of the known structure, the 7×7, and the undetermined structure, the Ga-terminated  $\sqrt{3} \times \sqrt{3} R 30^\circ$ , and if sharp interfaces between two dissimilar domains are found, then the STM can be used to analyze the registry across the interface. (Go85, Wi87)

The procedure for this experiment begins once again by preparing a clean Si(111)7×7 surface. Gallium is then deposited as before, but with a reduced evaporation time. As a result of the lower exposure, the gallium coverage will not be adequate to terminate the entire surface, so regions of the 7×7 reconstruction will remain. Ideally, the surface should simultaneously exhibit both the 7×7 and the  $\sqrt{3}\times\sqrt{3}$ R30° diffraction spots before tunneling.

The preceding procedure is reliable but tedious, and two short-cuts may be employed. First, an interface between the two phases can be guaranteed at a cost of confinement to one region if the evaporation favors one side of the sample. Second, if after gallium deposition, all traces of 7×7 periodicity are obliterated, it is not necessary to desorb the entire gallium layer and start over from clean Si(111)7×7. The high-temperature annealing required to reconstruct Si(111) alone would be undesirable, for prolonged high-temperature processes both strain the pumping system by outgassing the chamber and exacerbate thermal drift during tunneling. Instead, it is necessary only to desorb just enough excess gallium that the 7×7 reconstruction begins to appear. The sample heating must then be cut off immediately to prevent complete gallium disappearance. This process can be carried out with continuous sample exposure to the LEED apparatus, and without requiring that the sample temperature exceed 650°C.

When the mixed surface is scrutinized under the STM, typically large regions of one or the other domain appear. Occasionally, a sharp interface between the two phases is encountered, as in fig. 4.3. The analysis then consists of studying corrugation traces, or one-dimensional maps of tip

height versus lateral position, along lines that span the interface. In this work, the traces are extracted from raw two-dimensional scans at the IRIS station. Fig. 4.4 displays an example of such a trace taken along the path indicated. On this and other cuts examined, the corrugation is in close agreement with a  $T_4$  model for the Ga adatom binding site. The trace that might have resulted from a hypothetical  $H_3$  structure is also indicated to illustrate that the STM can comfortably distinguish the two structures.

The association of a line trace with one of the two models derives from the explicit construction of alternate models for the interface, according to the possible binding sites under consideration. Fig. 4.5 illustrates such a comparison. The Si adatoms in the  $7\times 7$  reconstruction are placed on the  $T_4$  site in both cases according to the DAS model, whereas the alternative gallium positions are considered explicitly. The corrugation trace from the actual image can then be compared with corresponding traces derived from the two models to determine the best fit. Scrutinization of many interfaces on separate samples has not resulted in the detection of Ga adatoms occupying the  $H_3$  site. Apparently, gallium adatoms on Si(111) occupy the  $T_4$  position exclusively. The combination of STM and X-ray standing-wave interferometry data has therefore produced a complete determination of the Ga position in the  $\text{Si}(111)\sqrt{3}\times\sqrt{3}R30^\circ$ -Ga surface.

The gallium-terminated surface commonly incorporates an additional type of interface separating domains of the  $\sqrt{3}\times\sqrt{3}R30^\circ$  and  $5\times 5$  phases. In fact,  $5\times 5$  domains appear commonly on gallium-terminated  $\sqrt{3}\times\sqrt{3}R30^\circ$  surfaces without the long-range coherence to be represented in a LEED pattern. The  $5\times 5$  reconstruction is one of three DAS structures that were

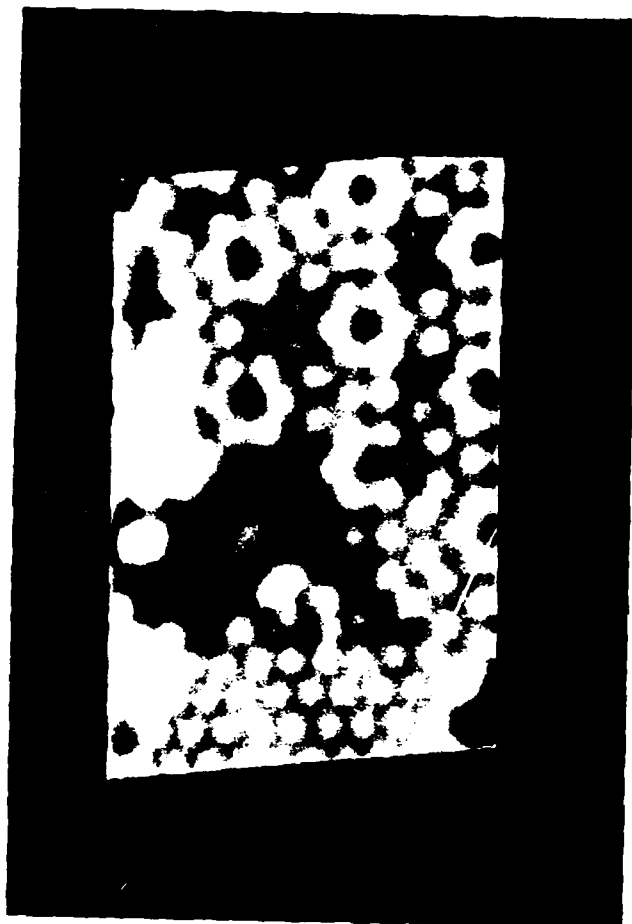


Fig. 4.3 STM image showing a boundary between domains of  $7 \times 7$  and  $\sqrt{3} \times \sqrt{3} R 30^\circ$  structure. The line indicates the path of a corrugation trace. Tip bias = -1.14V, 1nA.

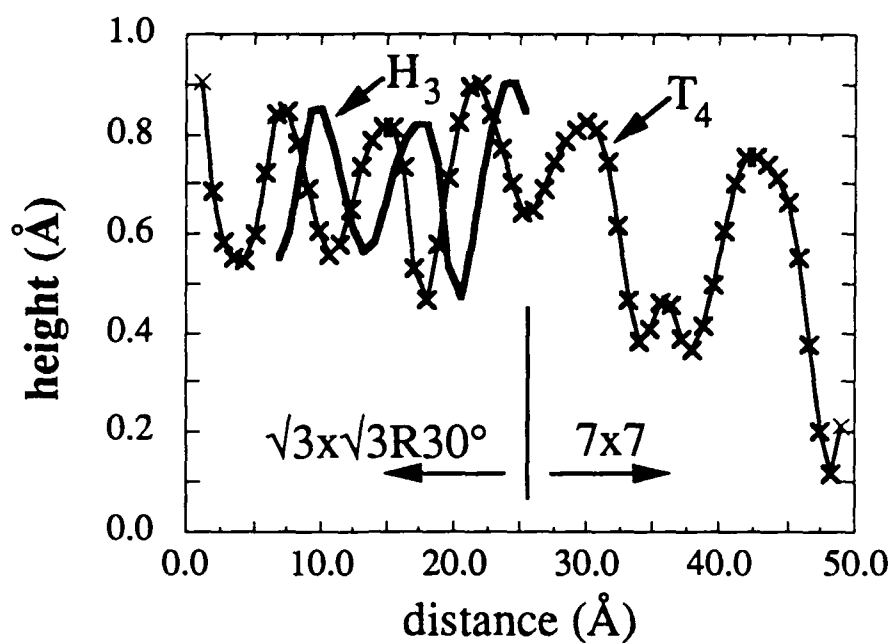


Fig. 4.4: Corrugation trace representing tip height vs. lateral distance, along the line in fig. 4.3 spanning the  $7\times 7$ - $\sqrt{3}\times\sqrt{3}$  interface, demonstrating T4 adatom occupation. Actual data points are marked with an "X," while the heavy line indicates how the trace might have appeared if the surface had adopted the H3 structure.

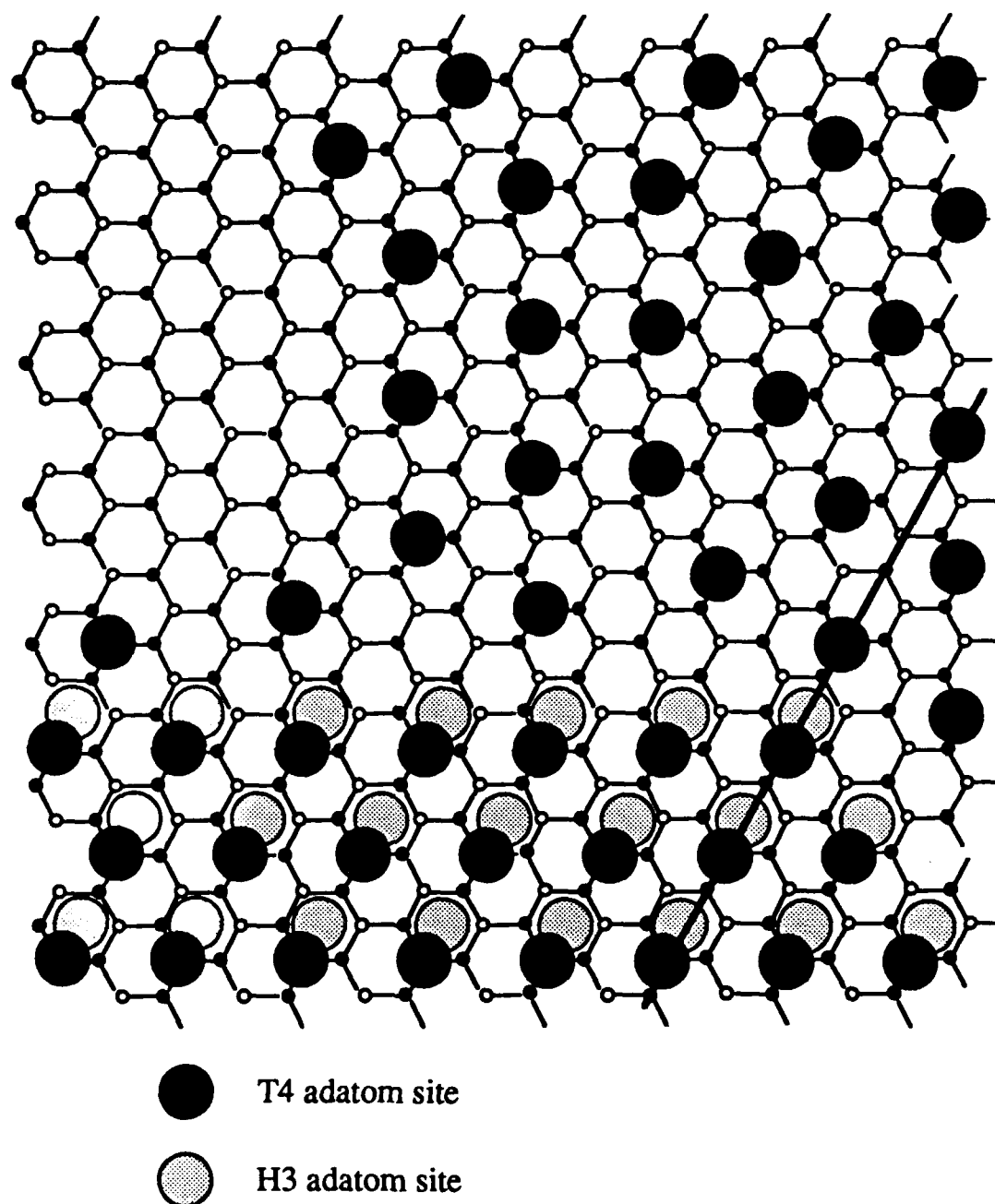


Fig. 4.5: Two alternate models for the adatom binding configuration in the tunneling image, fig. 4.3. The solid line is the path for the corrugation trace in fig. 4.4, which demonstrates that the T4 structure, *not* the H3, is realized.



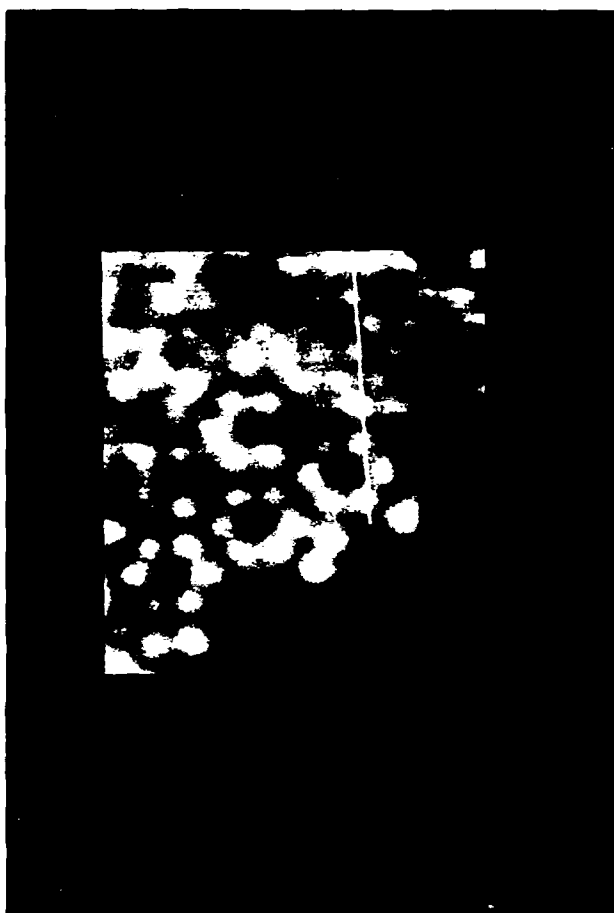


Fig. 4.6 STM image showing a  $5 \times 5 - \sqrt{3} \times \sqrt{3} R 30^\circ$  interface. Tip bias = -1.6V, 500pA.

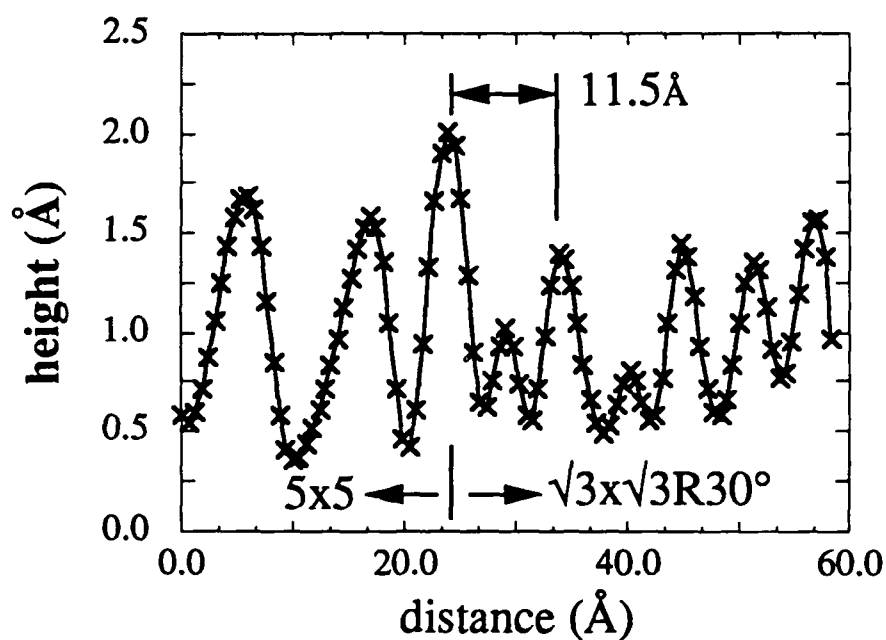


Fig. 4.7: Corrugation trace along the  $5 \times 5 - \sqrt{3} \times \sqrt{3} R 30^\circ$  interface in the tunneling image of fig. 4.7. The cut demonstrates the consistency of T4 adatom occupation across the interface, for an H3 structure on either side would place the indicated atoms  $13.5 \text{ \AA}$  apart. The reconstructions were induced by Ga adsorption.

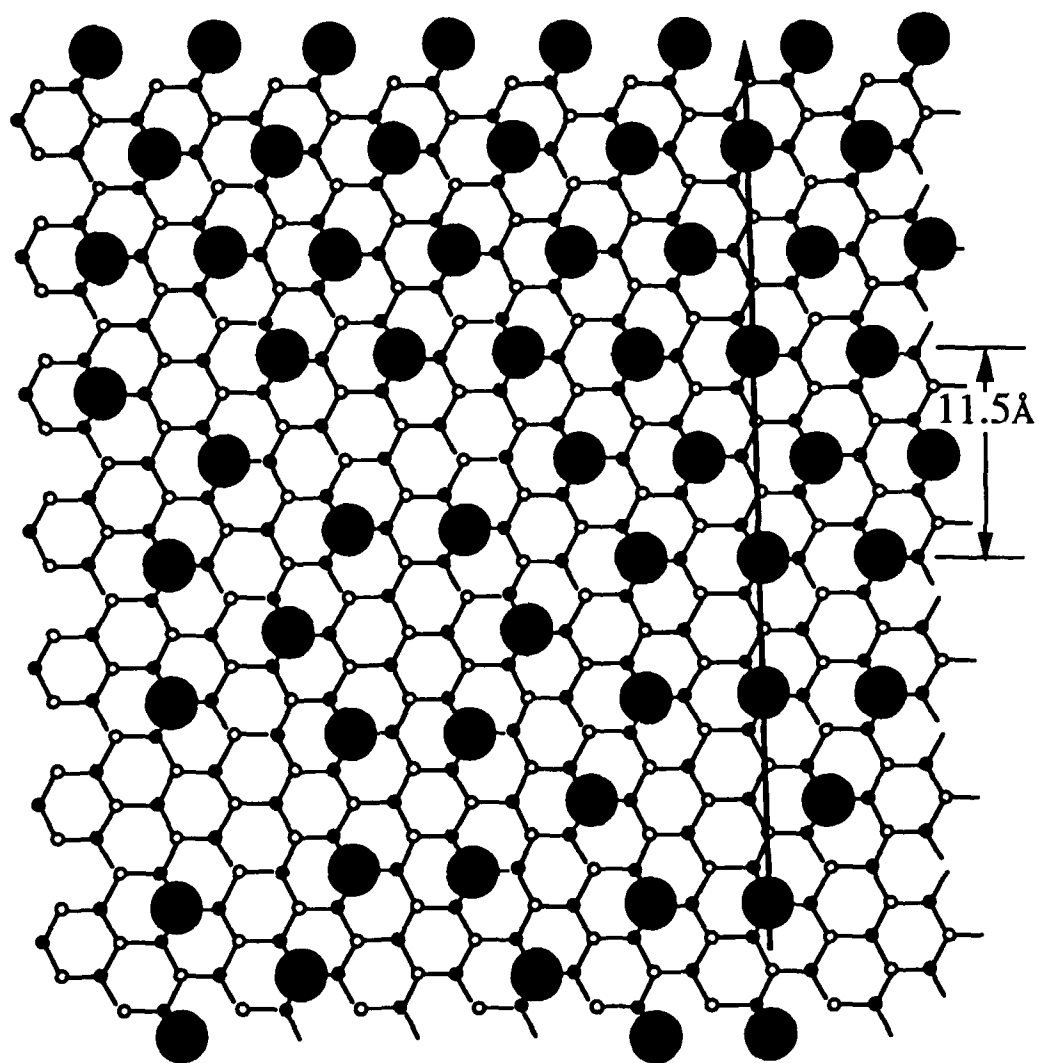


Fig. 4.8: Model for the  $5\times 5-\sqrt{3}\times\sqrt{3}R30^\circ$  interface in the Si(111)-Ga surface of fig. 4.6. The solid line is part of the path of the corrugation trace of fig. 4.7.

previously observed locally in STM images of laser-annealed Si(111).  
(Be86)

If the  $5\times 5$  phase appears in regions where the gallium concentration is locally insufficient to form a complete  $1/3$  ML covering, then the prevalence of this new phase as an intermediate between the  $7\times 7$  and  $\sqrt{3}\times\sqrt{3}R30^\circ$  structures might be understood according to the principles of §III.2. It was noted there that a transition from the  $7\times 7$  to the  $5\times 5$  reconstruction would be expected to accompany the application of a compressive stress to the surface. In addition, it has been found that the tensile stress associated with gallium adsorption on the  $T_4$  site is expected to be lower than that of silicon adsorbed on the same site, after relaxation. Therefore, the partial substitution of silicon adatoms on clean Si(111) $7\times 7$  by gallium should increase the compression of the surface and drive a transition to the DAS surface of lower index.

The  $T_4$  binding of site of adatoms in the  $5\times 5$  structure, as predicted by the DAS model for that reconstruction, can be verified by applying the above analysis to interfaces in images such as fig. 4.6. With the  $\sqrt{3}\times\sqrt{3}R30^\circ$  binding site now established as  $T_4$ , the best fit configuration for the  $5\times 5$  region is shown explicitly in figs. 4.7 and 4.8. Once again,  $T_4$  adatom occupation is found to hold on both sides of the interface.

#### IV.1.3 Highly inhomogeneous surfaces and electronic contributions

Controlled deposition of very low quantities of gallium ( $\ll 1/3$  ML) on reconstructed Si(111) have resulted in an apparent local mixing of

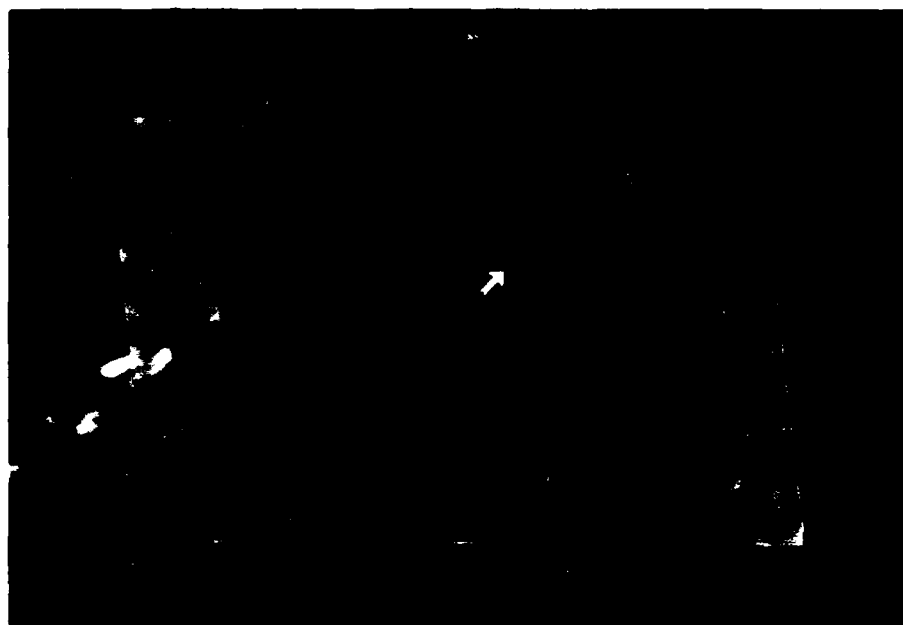


Fig. 4.9 STM image of the 7x7 reconstruction following light deposition of Ga. The arrow indicates a dark, minority species incorporated into the surface lattice. Tip bias = -1.1V, 1nA.

gallium and silicon atoms. For example, fig. 4.9 shows a typical region of  $7\times 7$  periodicity found near an interface between  $7\times 7$  and  $\sqrt{3}\times\sqrt{3}R30^\circ$  domains on a surface prepared to exhibit a coincidence of the two diffraction patterns, as above. A striking feature of this region is the presence of two apparently distinct species at the surface, indentifiable by their relative brightnesses. This behavior is not found for adatoms on clean Si(111) $7\times 7$  surfaces. Consequently, the image suggests the presence of both gallium and silicon in the reconstruction, yet the complicated nature of this surface structure, which involves rest atoms, adatoms, and substantial subsurface relaxations, would seem to preclude a definitive identification of the actual gallium sites with the STM alone.

A stronger case for the chemical identification of an occupied site with STM could be made within the far simpler  $\sqrt{3}\times\sqrt{3}R30^\circ$  structure, where gallium adatom occupation has been established. On mixed phase surfaces,  $\sqrt{3}\times\sqrt{3}R30^\circ$  domains near  $7\times 7$  regions also display local mixing, as illustrated in fig. 4.10. Once again, under particular tunneling bias conditions, the contrast between the two types of sites is striking. Moreover, the relative brightness of the two species is strongly bias dependent. This latter observation, together with the expectation that the difference between the vertical positions of silicon and gallium adatoms should be low ( $< 1\text{\AA}$ , see §III.3), suggests that the observed contrast results from differing local electronic structures associated with each type of adatom. The possibility of identifying electronic effects associated with individual atomic defects from topographical images was demonstrated recently under similar conditions. (Ha88b)

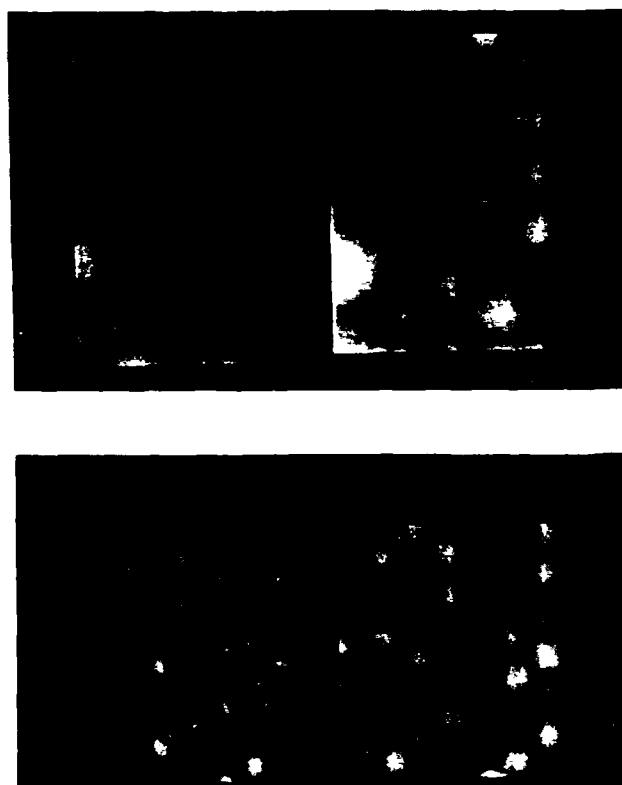


Fig. 4.10 Top--STM images of  $\text{Si}(111)\sqrt{3}\times\sqrt{3}\text{R}30^\circ\text{-Ga}$  at -1V tip bias (left) and -1.5V (right), showing a reversal of adatom shading. Bottom--STM images of  $\text{Si}(111)\sqrt{3}\times\sqrt{3}\text{R}30^\circ\text{-Ga}$  at +1V (left) and -0.8V (right), showing consistent shading at low tip bias.

The experimental and theoretical band structures associated with Si and Ga adatoms in  $\sqrt{3}\times\sqrt{3}$ R30° coverings are understood and were presented in §III.3 above. Recalling the results in that section, both adatom-covered surfaces are expected to possess a fully occupied back-bond state  $\approx 1.5$ -2eV below the fermi level, but they differ in the energy of their respective dangling bond orbitals. While the silicon adatom's orbital is partially occupied and should lie near the fermi level, that of gallium appears  $\approx 1$ eV higher.

Examination of fig. 4.10 reveals that the relative brightness of the adatoms follow a bias dependence that correlates with the band structures established by photoemission. Employing the analysis of §II.1 above, a greater retraction of the tip over one site than over another would suggest that the integrated surface density of states between the fermi level and the tip bias voltage is higher for the first site than the second, if the actual vertical atomic positions are equal. Thus, the bright appearance of the minority species, presumably silicon, at low positive bias is consistent with the partial occupation of the dangling bonds atop silicon, but not above gallium. Likewise, if unoccupied states are probed, the bright appearance of the minority species at low negative tip bias reverses as the bias passes the unoccupied gallium dangling bond level. At higher negative tip bias ( $> 1.8$ eV above the fermi level), the contrast between the two types of sites disappears. This observation also follows from the band structures identified by photoemission, for the unoccupied dangling orbitals on each type of site lie below these higher bias levels. We note here that our



observations of the contrast of the atomic sites differ in some details from another recent report of this system. (No88)

As noted in §III.3 above, silicon substitution in the adatom layer of a  $\sqrt{3}\times\sqrt{3}R30^\circ$  structure, apparently observed on the gallium-terminated surface of this work, was also surmised for the indium-terminated surface from KRIPES (Ni85a) and STM, (No88) and for the aluminum-terminated surface on the basis of KRIPES. (Ni87a) However, a predominance of silicon in the adatom layer has *not* been observed in any of these structures. We shall find below that the boron-terminated Si(111) surface, in contrast to these cases, can admit a predominance of silicon substitution by a mechanism that is not available to surfaces terminated by boron's Group III cousins.

## IV.2 Beyond 1/3 ML--Incommensuration and Superlattices

### IV.2.1 Sample preparation

Several coincident diffraction patterns have previously been observed upon further deposition of Ga on Si(111) within the submonolayer range. In order to image the associated gallium-induced overlayer, a clean, reconstructed Si(111) surface was first prepared. As before, the  $7\times 7$  LEED pattern characteristic of clean Si(111) first transformed with gallium deposition to the  $\sqrt{3}\times\sqrt{3}R30^\circ$  pattern. Further gallium coverage, together with subsequent annealing at 300-500°C, resulted in the disappearance of this latter diffraction pattern and the formation of sets of hexagonal arrays of diffraction spots centered on the first-order spots of the silicon substrate. The assignment of the new spots as  $6.3\times 6.3$ ,  $6.3\sqrt{3}\times 6.3\sqrt{3}$ , and  $11\times 11$ ,

together with photographs of the diffraction patterns themselves, has been presented previously. (Ot85)

The reversibility of the deposition process permitted an alternative method of creation of the overlayer by first depositing excess gallium, such that only faint first-order LEED spots would be visible. Annealing at 500°C, with continuous examination under LEED, would then desorb the excess gallium and reorder the surface to the overlayer periodicity. After the sample had cooled to room temperature, it could be transferred to the STM.

As with the case of lower gallium coverage treated in §IV.1 above, we do not possess the means for an independent measurement of the average gallium coverage over the sample *in situ*. In any case, such a measurement would not reflect the local gallium distribution in the tunneling images of the inhomogeneous surfaces that are normally prepared. A more meaningful estimate of local gallium coverage, which we attempt to employ whenever possible, is to correlate the periodicity observed in tunneling images with the diffraction patterns, which in turn have been associated with particular gallium coverages in previous reports. For example, each of the diffraction patterns observed for various stages of submonolayer gallium deposition has previously been associated with a particular coverage by quantitative X-ray fluorescence scattering, calibrated with Rutherford backscattering. (Ze88, 89) We point out that, while our retarding-field Auger apparatus does not detect gallium at 1/3ML (fig. 4.11), it does detect the Ga peak in the overlayer, as shown in fig. 4.12. However, we cannot perform a precise quantitative analysis on the basis of

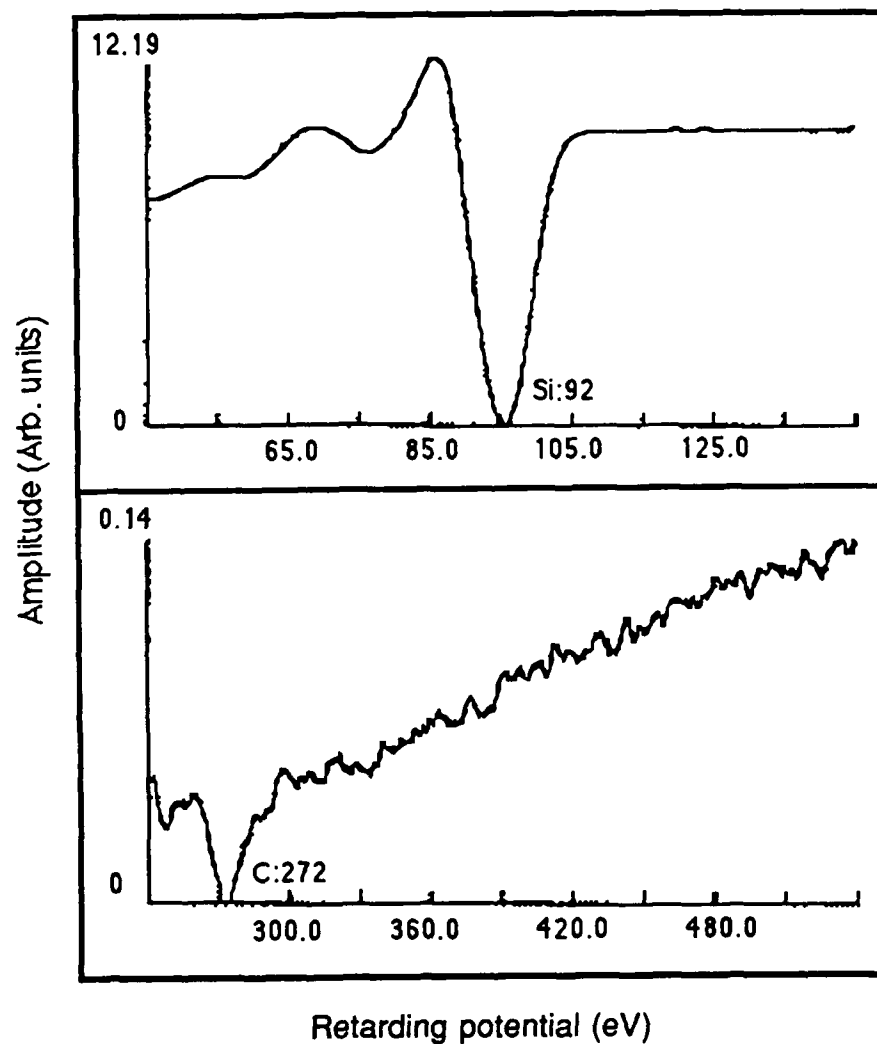


Fig. 4.11: Retarding field Auger spectrum of  $\text{Si}(111)\sqrt{3}\times\sqrt{3}\text{R}30^\circ\text{-Ga}$ . A weak, broad Ga peak at 55eV is apparent.

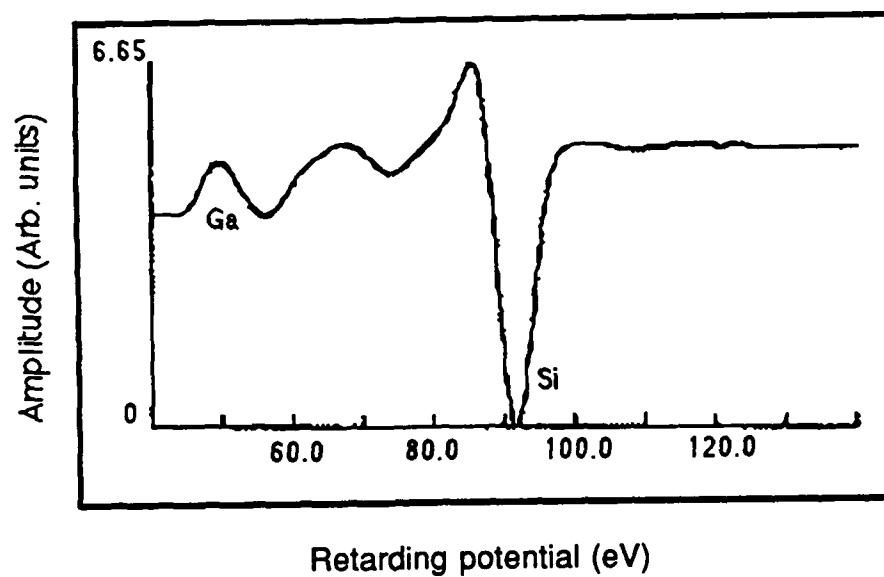


Fig. 4.12: Retarding field Auger spectrum of the incommensurate Ga overlayer, from a surface of the type in fig. 4.13.

this spectrum for want of a precise gallium peak height calibration. While the spectrum of fig. 4.12 does reflect the presence of gallium, it does not indicate contamination above the levels characteristic of the "clean" Si(111) from which the  $7\times 7$  reconstruction is prepared in this work.

#### IV.2.2 Tunneling results

In sharp contrast to Si(111) $7\times 7$  and the Si(111) $\sqrt{3}\times\sqrt{3}R30^\circ$ -Ga surfaces, on which stable tunneling was possible under a wide range of tipbiasing conditions, we have found that reproducible imaging of the gallium overlayer has been possible only at substantially higher tip-sample separation than was necessary for the two previous surface structures. Therefore, the images displayed in this section were acquired with higher voltage bias and lower sample current than was required for the surfaces studied elsewhere in this work. Still, occasional jumps in the tip-sample separation, often accompanied by the onset of instability, indicated frequent transfer of material between the tip and the surface.

Fig. 4.13 displays an image of the gallium overlayer surface which was prepared according to the procedure in the previous section. After tunneling, the sample was removed from the chamber for Rutherford backscattering, which determined an average gallium coverage of 1 ML. Two salient points emerge from examination of this image. First, noting the dimensions of the figure, we find that the protrusions are not individual atoms, but rather aggregates, or supercells arranged in an ordered, hexagonally close-packed structure of lattice spacing  $24\text{\AA}$ , aligned with the symmetry axes of the surface. This distance corresponds to the  $6.3\times 6.3$

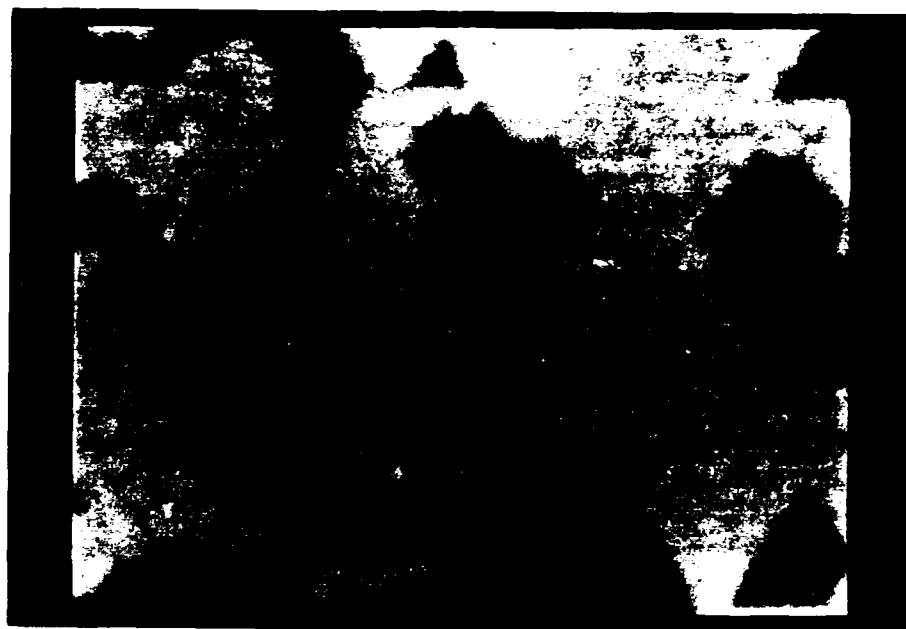


Fig. 4.13 470x400Å STM image of the Ga-induced overlayer characteristic of  $\approx 0.75\text{ML}$  Ga coverage. Tip bias = -3.3V, 800pA.

periodicity observed by LEED. Immediately, the origin of this diffraction pattern is found to be an incommensurate superlattice. Because individual atoms are not distinguished in this image, thermal drift has not been corrected in this or several other images in this section.

Second, there are two distinct terraces in the images, and in fact the entire reconstructed surface is found to be decorated with remarkably straight steps that align themselves with the three symmetry axes of the surface. The vertical corrugation within one terrace is  $\approx 0.75 \text{ \AA}$ , and the shape of the supercells is well-defined right up to the step edges. The steps may be shown more explicitly in a three-dimensional representation of the data in fig. 4.14. The step height is found to be  $3.2 \pm 0.2 \text{ \AA}$ , which coincides with the double-layer spacing of bulk silicon, parallel to the (111) face. Apparently, single atomic silicon steps lie underneath the visible structure.

The detailed shape of the supercells has been found to vary on samples prepared at different times. For example, fig. 4.15 displays the superlattice material with far less regular supercells than in fig. 4.13. Nevertheless, the  $6.3 \times 6.3$  periodicity is preserved over the long range. We have not been able to correlate the regularity in the supercell shape with variations of a particular step in the surface preparation.

While the preceding images of this section illustrate the nature of the overlayer material, it would be helpful to prepare an inhomogeneous surface incorporating reconstructions of known structure in order to explore the initial growth stages of the new material. The utility of this approach was already illustrated in §IV.1 for the case of the simpler  $\sqrt{3} \times \sqrt{3} R 30^\circ$  structure. Following a similar course toward preparing a multiple-phase surface, the



Fig. 4.14 A portion of the region in the previous figure emphasizing the steps of height  $3.2\text{\AA}$ .





Fig. 4.15 200x200Å STM image of a Ga-induced overlayer surface, showing a more irregular pattern of supercells than in fig. 4.13. Tip bias = -3.1V, 500pA.

procedure here is to end up with a surface that simultaneously exhibits as many diffraction patterns as possible, including  $7\times 7$ ,  $\sqrt{3}\times\sqrt{3}R30^\circ$ , and the overlayer LEED spots. On particularly auspicious occasions, all corresponding real-space structures might then be represented in one image.

An example of such an image is presented in fig. 4.16, which illustrates a number of stages in the formation of the overlayer. First, a number of regions of the  $7\times 7$  reconstruction remain, and one unit cell is indicated. The presence of both this and the  $\sqrt{3}\times\sqrt{3}R30^\circ$  domains also indicated allow an accurate calibration of the lateral tip displacement for this particular image. We note that the gallium adatoms within the  $\sqrt{3}\times\sqrt{3}R30^\circ$  regions occupy the  $T_4$  position, confirming our earlier determination. Several modified  $7\times 7$  unit cells indicated apparently hold gallium nucleation sites in a  $1\times 1$  filling, shown explicitly in the model of fig. 4.17. This filling is not observed to extend continuously beyond an area of three  $1\times 1$  cells within individual  $7\times 7$  unit cells.

Finally, we find islands of what appears to be the superlattice structure, over which the tip retracts  $1.2 \text{ \AA}$  relative to its position above the surrounding adatoms. Using the lateral distance calibration provided by the previously determined reconstructions in the image, the spacing between supercells in the islands is found to be  $24 \text{ \AA}$ , as on the superlattice previously identified, suggesting that the islands in this image in fact represent initial growth of the overlayer material.

While several  $7\times 7$  regions in this image are spatially separated, their symmetry axes align exactly and should therefore indicate the state of the surface before the growth of gallium. Thus, the original, pristine  $7\times 7$

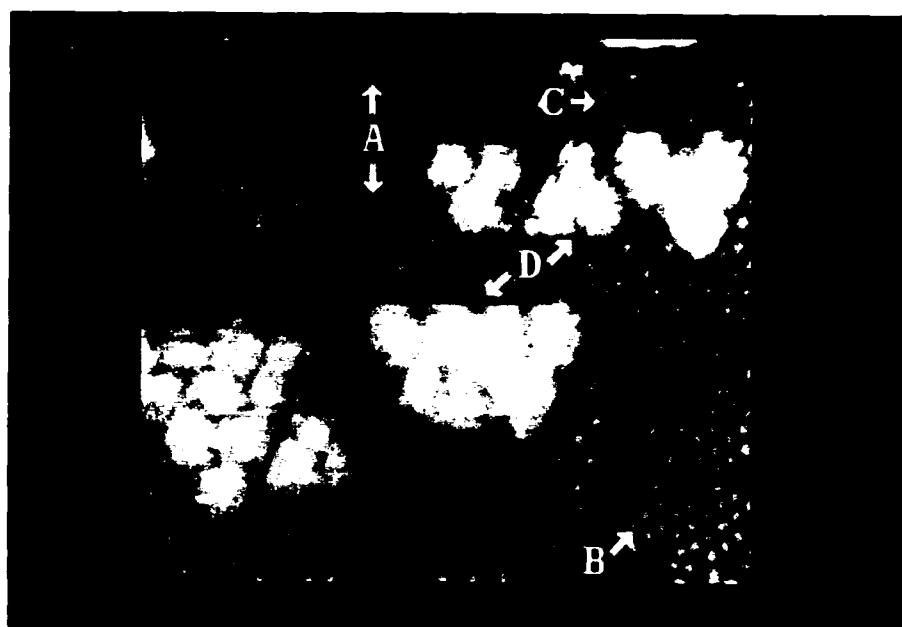


Fig. 4.16 200x200Å STM image showing regions of (a) 7x7, (b)  $\sqrt{3}\times\sqrt{3}R30^\circ$ -Ga, (c) nucleation sites, and (d) islands of superlattice material. Tip bias = -1.5V, 1nA.

## Nucleation

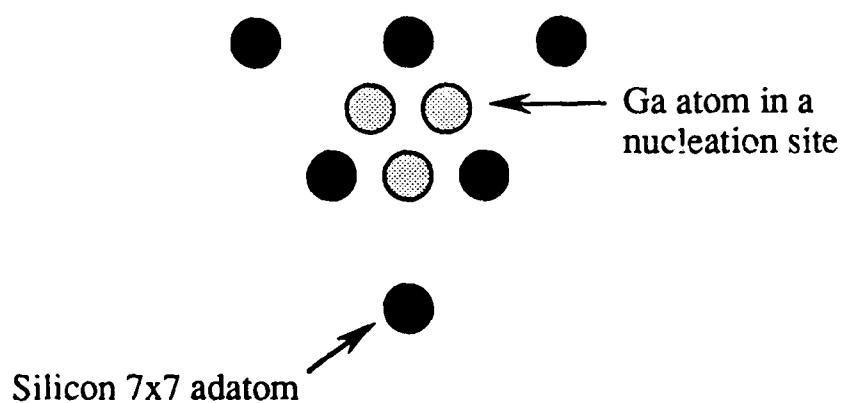


Fig. 4.17: A picture for the gallium nucleation observed in fig. 4.16, wherein gallium atoms are incorporated into the 7x7 reconstruction to form a local, 1x1 filling.

surface was not completely disrupted by the shower of gallium, but retained enough of its character to communicate the long-range order in its past. It is observed that one edge of each island in the image aligns along one straight edge of a primordial series of  $7\times 7$  cells. However, the mismatch of the  $7\times 7$  and the  $6.3\times 6.3$  spacings causes the islands to fall out of alignment with the  $7\times 7$  skeleton at their far edges.

When a portion of this image is scanned with higher resolution, (fig. 4.18), individual atoms in the supercells can be distinguished and are seen to compose an oriented, hexagonal array of  $4.1\text{\AA}$  spacing, again incommensurate with the substrate lattice but aligned with its symmetry axes. The overlayer material is therefore an incommensurate superlattice, whose individual supercells are in turn composed of an incommensurately packed atomic lattice. A corrugation trace on the superlattice, showing the  $4.1\text{\AA}$  internal atomic spacing, is shown in fig. 4.19. The distinction of this structure from a  $1\times 1$  lattice, of  $3.8\text{\AA}$  spacing, is within the resolution of the STM.

Since the transformation of the surface via  $7\times 7 \rightarrow \sqrt{3}\times\sqrt{3}R30^\circ \rightarrow$  incommensurate overlayer with increased gallium coverage reverses with annealing, the desorption of gallium from a surface already prepared with the overlayer should offer an alternate route to the juxtaposition of multiple phases. In practice a mixed-phase surface could be obtained from a sample initially completely covered by the superlattice by repeatedly applying and removing the heating current with the sample positioned so that the LEED pattern could be seen continuously. The sample reached a maximum of

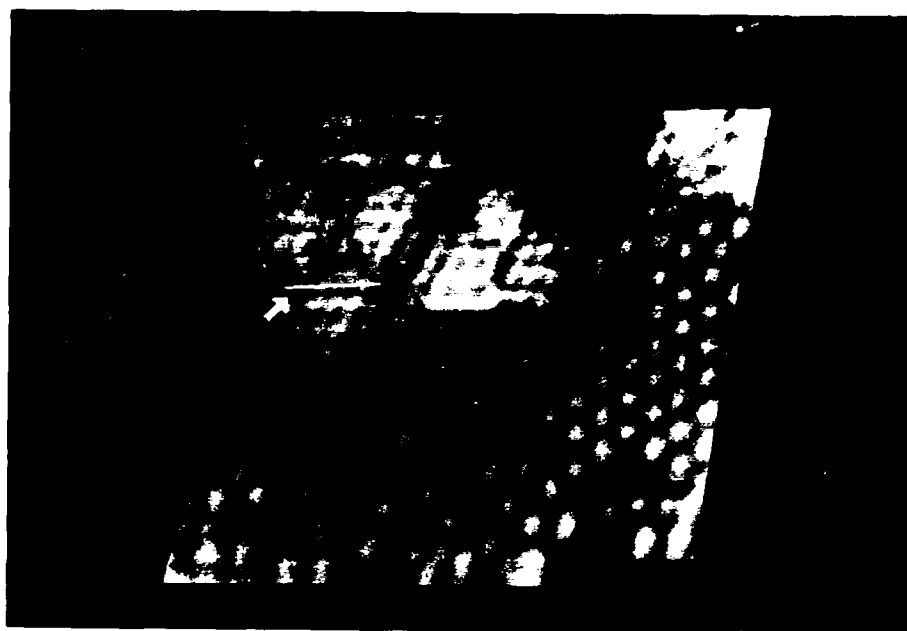


Fig. 4.18  $100 \times 100 \text{ \AA}$  STM image showing a portion of fig. 4.16 in greater detail. The atomic-level structure of the supercells is evident.

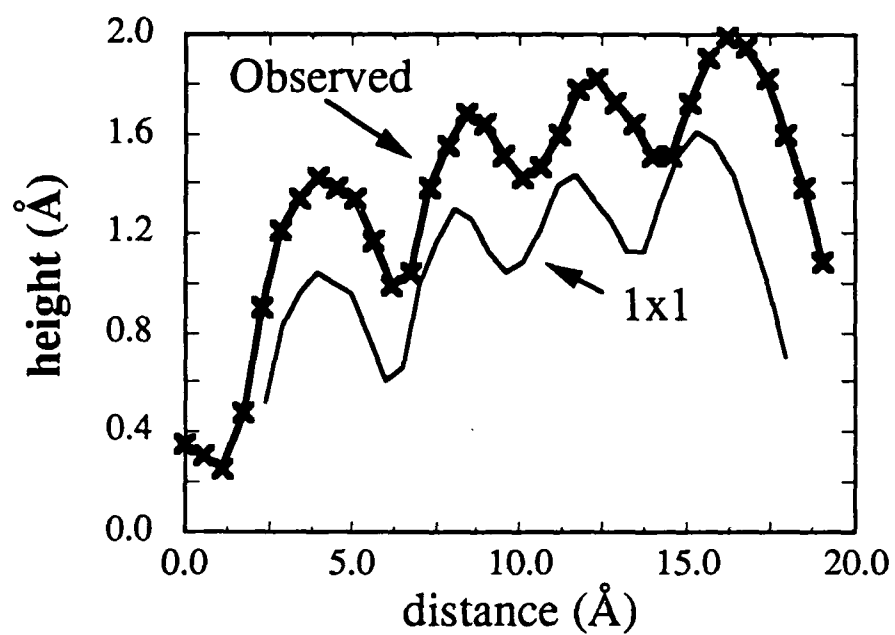


Fig. 4.19: Corrugation trace within one supercell in fig. 4.18, showing the incommensurate,  $4.1\text{\AA}$  atomic spacing.

600°C for <5 sec. per cycle, and the heating power was removed once the  $\sqrt{3}\times\sqrt{3}R30^\circ$  diffraction pattern appeared.

The result of this procedure is presented in fig. 4.20. After some Ga desorption, the terrace edges which were so straight and well aligned in previous images are evidently disturbed and appear irregular here. In addition, regions of distinct appearance from the superlattice are found at step edges. The tip retraction above these regions relative to the lower terrace is 1.1 Å. When a portion of the image is scanned with higher resolution (fig. 4.21), it is found that the dimensions and orientation of the unit cells in this region are identical to those of the  $\text{Si}(111)\sqrt{3}\times\sqrt{3}R30^\circ$ -Ga structure. It appears, then, that the transformation of the surface lattice by desorption is initiated at the step edges, and images such as these offer a glimpse of an intermediate stage in this process.

It was pointed out in §III.2 that the island growth of Ga on  $\text{Si}(111)$  that occurs above 1 ML has been investigated extensively elsewhere. A wide distribution of island sizes has been found by electron microscopy. Additionally, the islands are highly mobile and coalesce with time. The low melting point of 30°C for gallium suggests that some islands of pure gallium might be semi-liquid at room temperature. Fig. 4.22 presents an STM image of a droplet without discernible internal corrugation, demonstrating that the apparent prototype of a liquid island characteristic of >1ML gallium coverage can be observed by STM.

The images shown above present a comprehensive view of the gallium overlayer from the vantage of STM, but a complete understanding of the binding of the surface to the substrate requires additional information.



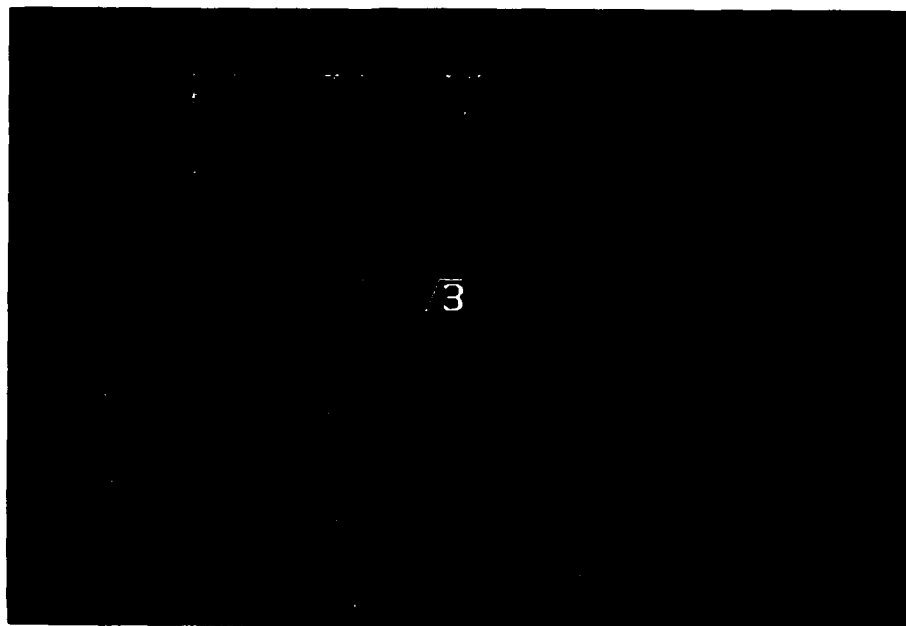


Fig. 4.20 400x400Å STM image following partial Ga desorption from a surface of the type in fig. 4.13. Regions of  $\sqrt{3}\times\sqrt{3}R30^\circ$  periodicity form at terrace edges. Tip bias = -2.5V, 1nA.

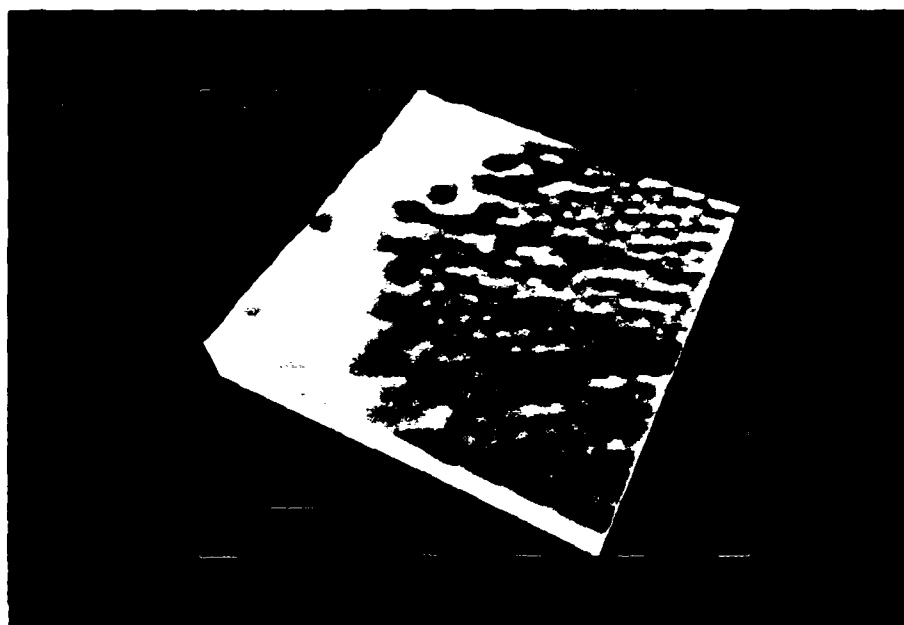


Fig. 4.21 100x100Å STM image showing a  $\sqrt{3}\times\sqrt{3}R30^\circ$  region at a step edge in greater detail. Tip bias = -2.6V, 1nA.

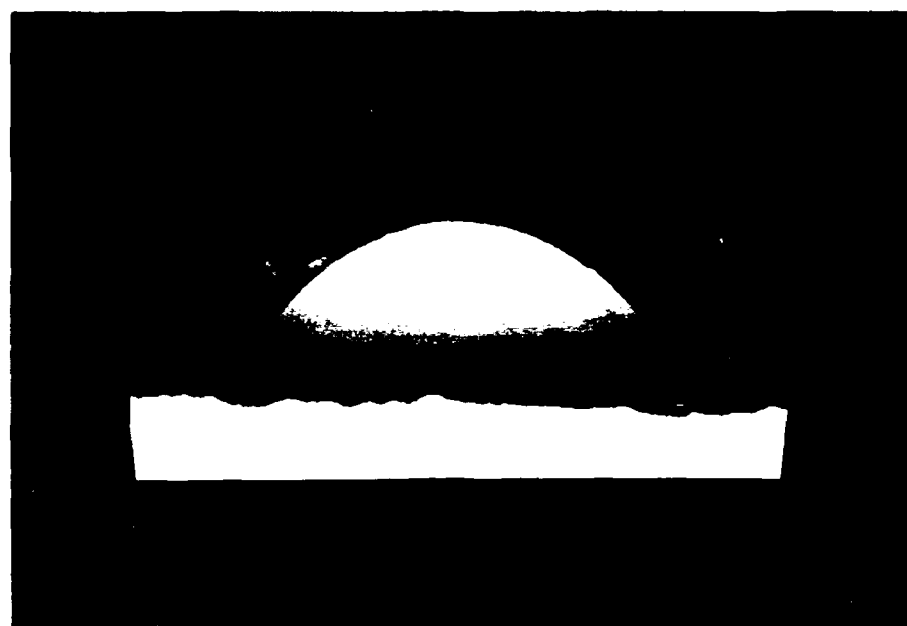


Fig. 4.22 400x400Å STM image showing a droplet on Si(111) following heavy Ga deposition. Tip bias = +5V, 800pA.

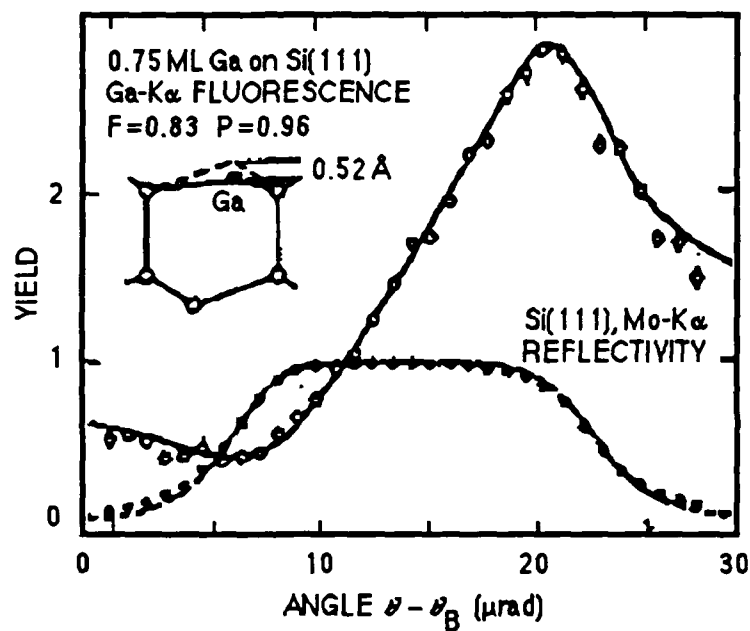


Fig. 4.23: Reflectivity and fluorescence yield versus angle for the Ga overlayer on Si(111), from X-ray standing-wave interferometry. The inset indicates a substitutional model for Ga, as presented by Ze88.

In fact, X-ray standing-wave measurements performed on this system placed the vertical position of the gallium only  $.25\text{\AA}$  above the extrapolated lower half of a silicon double-layer. (Ze88) The bulk separation of planes within one double layer is  $.77\text{\AA}$ . Based on this information alone, a natural model for the overlayer might have put gallium in  $1\times 1$  substitutional sites in the outer double layer. Fig. 4.23 presents the model originally proposed on the basis of the X-ray data.

The difficulty is that such a model would not account for the incommensurate diffraction patterns, and the  $3.84\text{\AA}$  spacing predicted by a  $1\times 1$  substitutional model is at odds with the  $4.1\text{\AA}$  spacing found in the tunneling images. Taken alone, therefore, the vertical position measurement is also insufficient to determine the surface structure completely. However, the synthesis of the tunneling and interferometric data shall lead to a consistent picture that accounts for the observations of each. (Ch88)

#### IV.2.3 A microscopic picture of incommensuration

According to the interferometric measurements on the overlayer system, the outer double layer does appear to be compressed by  $>0.5\text{\AA}$ . The resulting bond angle stress is apparently released by a lateral expansion of the surface to form the  $4.1\text{\AA}$  periodicity observed in the tunneling images. The boundaries between the supercells would then arise naturally from the incommensurate relation between surface and substrate, manifested in a highly periodic array of misfit dislocations. Gallium metal is an orthorhombic crystal with lattice parameters  $\approx 4.5\text{\AA}$ , so the sign of the

mismatch of the bulk silicon and gallium lattice parameters matches the direction of surface relaxation. A picture of the surface structure consistent with the available data sets is shown in fig. 4.24.

A number of experimental observations may be interpreted in light of this model. The high step density present in the superlattice but absent from the virgin substrate would come about as silicon atoms that are freed up in the formation of the lower terrace by gallium substitution contribute to the formation of the upper terrace. The vertical rise of a terrace must then coincide with the bulk double layer spacing, as is observed. This process would be reversed by the flash heating and accompanying desorption which led to figs. 4.20 and 4.21. In that case, if gallium desorption initiates at steps, coverage of the remaining fresh silicon double layer by fewer available gallium atoms would yield the  $\sqrt{3}\times\sqrt{3}R30^\circ$  structure observed at step edges.

Next, the order of progression of the growth of the superlattice can be inferred from figs. 4.16 and 4.18 as follows. The gallium apparently nucleates initially by filling in  $7\times 7$  subunits in a local  $1\times 1$  filling. The resulting compressive stress of such a filling may even offset the tensile stress associated with the  $7\times 7$  reconstruction, but the absence of any more extensive  $1\times 1$  areas suggests that any further incorporation of gallium immediately precipitates an outward expansion to relieve the surface compression. This scenario for the origin of overlayer islands from  $7\times 7$  cells also accounts for the observed occurrence of one edge of each island on a  $7\times 7$  domain wall.

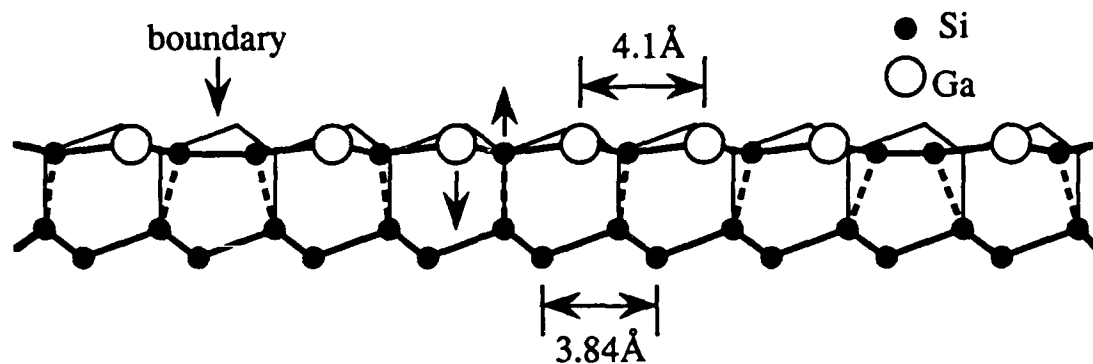


Fig. 4.24: Model for the gallium overlayer on Si(111), showing the incommensurate relationship between the outer-layer and substrate periodicities. The outer double layer is compressed vertically into a planar, graphite-like Si-Ga alloy. Accompanying the vertical compression is a lateral, outward relaxation.

The compression of the outer double layer results in two nearly coplanar, interpenetrating hexagonal silicon and gallium sublattices which together more nearly resemble a graphite plane than a silicon double layer. While the surface layer here is a Si/Ga alloy rather than graphite, the inertness of an outer layer with a planar topology fits well with previous observations that gallium does not wet the Si(111) surface above 1ML. (Zi87a, b, 88a, b)

The reason for the outer layer compression itself is not available from the data, but can be understood together with the drive toward lateral expansion as a consequence of the theoretical principles indicated in §III.2. Total energy calculations that were performed in conjunction with the X-ray standing-wave interferometry predicted a compression of the outer layer that would place the gallium atom in a vertical position in close agreement with the actual measurement, and it was realized in that work that the flattening of the bonds of gallium was a consequence of rehybridization of the of trivalent Ga atoms from the tetrahedral  $sp^3$  configuration toward the planar  $sp^2$ . (Ze88) This behavior fits the trend toward increasing compression from right to left across a row of the periodic table indicated in §III.2 supported theoretically (Me89b) and experimentally. (Be88, Pa86) However, the very high compressive stress of a hypothetical substitutional  $1 \times 1$  gallium-terminated surface (Me88) would favor a lateral expansion accompanying the vertical compression. While this analysis does not predict the exact lattice spacings of the surface, it does help to identify the competing forces at work.



A truly complete picture of this surface must account for the origin and assignment of all of the observed LEED spots, but this task is beyond the capabilities of the experimental techniques employed thus far and must await further study by other methods. We have already identified the  $6.3 \times 6.3$  diffraction pattern unambiguously with the supercell spacing, and the  $11 \times 11$  spots may arise from the  $4.1 \text{ \AA}$  atomic spacing by multiple scattering. While we also observe the  $6.3\sqrt{3} \times 6.3\sqrt{3}$  pattern, we have not seen obvious manifestations of this symmetry in the tunneling images. A surface as complex as this might well incorporate new periodicities in subsurface rearrangements. The exclusive surface sensitivity of STM prevents a straightforward observation of subsurface reordering. Moreover, the variety in the observed shapes of supercells on different samples suggests that the surface can assume several phases, possibly with different subsurface periodicities, which are not readily distinguishable under STM. The nature of the interfacial region might be illuminated through further study with EXAFS, UPS, or other spectroscopies.

The precise prediction of the observed periodicities that the surface consistently chooses to assume appears out of reach at this time. Some progress has been made in the construction of predictive models for the commensurate-incommensurate transition in simpler, physisorbed systems, (Co82) but the vastly more complicated nature of the chemisorbed system studied here, with its subsurface rearrangements and surface alloying, does not admit a straightforward application of these approaches. We have already identified the competing interactions among which the surface ultimately compromises with a specific atomic packing. Qualitatively, the

incommensurate relationship and interaction between the observed surface structure and the underlying silicon lattice will certainly drive the creation of new periodicities in the system. One dramatic product is the regular, 24Å spacing between dislocations. Yet, the interaction responsible for their creation may be so strongly dependent on lateral overlayer displacement as to preclude a simple microscopic explanation for their observed periodicity and structure. At least we can offer none here on the basis of the available data; rather, we must marvel at nature's ability to achieve a consistent, stable solution that accommodates violent interactions in seemingly intractable mathematical competition, once again.

## V. Boron Adsorption

### V.1 Preparation and imaging

A boron-induced  $\sqrt{3}\times\sqrt{3}R30^\circ$  surface structure can be acquired simply by annealing degenerately boron-doped Si(111). The process of boron segregation that induces this surface lattice has been described elsewhere. (Ko88a, He89) The samples used here were cut from  $\approx 10^{20} \text{ cm}^{-3}$  doped wafers and cleaned in vacuum by the procedure of §II.5. When annealed briefly at  $850^\circ\text{C}$ , the samples display the  $7\times 7$  reconstruction in both LEED and STM. Further annealing at  $1000^\circ\text{C}$  transforms the diffraction pattern to  $\sqrt{3}\times\sqrt{3}R30^\circ$ , as observed on the Ga-terminated surface. Annealing for two minutes was sufficient to observe large reconstructed regions under STM. Longer annealing times, up to  $3/4$  hr., were not found to degrade the quality of the LEED pattern or the tunneling images.

Fig. 5.1 illustrates an STM image of this surface. In accordance with the  $\sqrt{3}\times\sqrt{3}R30^\circ$  LEED pattern, protrusions, presumably adatoms, appear and are spaced  $6.7\text{\AA}$  apart. A mixture of two atomic species, distinguished by their relative brightness, is evident here. The brighter adatoms are apparently randomly distributed and, in this preparation, invariably account for 15-20% of the imaged atoms. Moreover, the relative brightness of the two types of sites persists regardless of the polarity and value of the tunneling bias voltage.

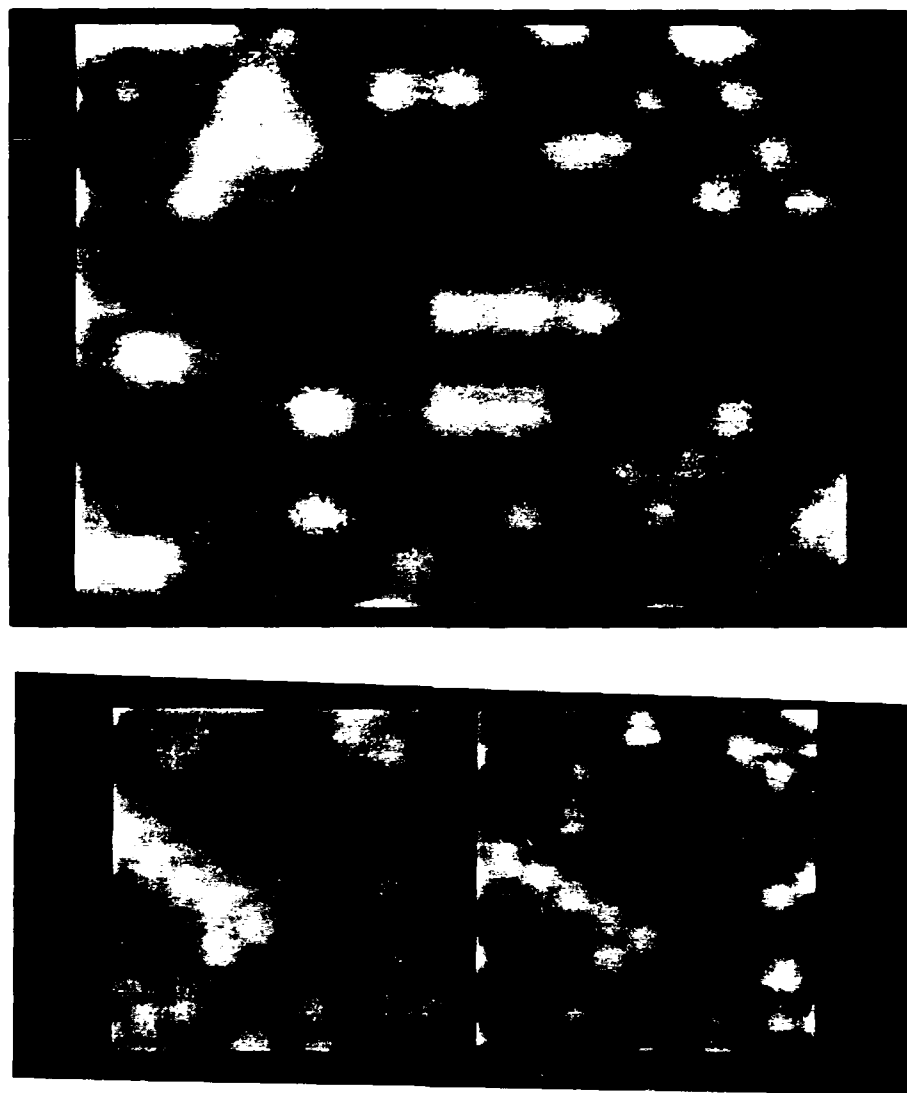


Fig. 5.1 (Top) 80x60Å STM image of  $\text{Si}(111)\sqrt{3}\times\sqrt{3}\text{R}30^\circ\text{-B}$  prepared by annealing heavily B-doped  $\text{Si}(111)$ . Tip bias = -1.25V, 1nA. (Bottom) STM images acquired at +1.1V (left) and -1.4V (right) tip bias, showing the constancy of the relative shading of the two types of adatom sites.

These observations already distinguish this surface from Si(111) $\sqrt{3}\times\sqrt{3}$ R30°-Ga.

With such persistent and regular inhomogeneity in this surface, it is tempting to try to control the overall ratio of the two types of sites observed. To this end, we have employed two additional methods of surface preparation. In the first of these, a clean silicon surface displaying the 7 $\times$ 7 reconstruction was first prepared on .04 $\Omega$ -cm As-doped Si(111). The ion gun was used to sputter boron onto the clean surface from a target held 1 cm away from the sample for  $\approx$ 45 sec. The  $\sqrt{3}\times\sqrt{3}$ R30° LEED pattern was then obtained after brief annealing at 800°C. Depositions were attempted with the sample held at various temperatures during the sputtering, from room temperature to 400°C, and the  $\sqrt{3}\times\sqrt{3}$ R30° symmetry resulted under all conditions.

STM investigations revealed that, while short deposition times yielded images similar to fig. 5.1, incorporating up to 25% bright adatoms, increased deposition times resulted in a diminished concentration of the bright sites (<5%), as shown in fig. 5.2. In contrast to the gallium case, no new ordered overlayer appeared with further boron deposition.

The last method of preparation began with a  $\sqrt{3}\times\sqrt{3}$ R30° reconstruction on a boron-doped Si(111) sample as above. Without further sample heating, additional silicon was deposited by evaporation from a second silicon wafer until the  $\sqrt{3}\times\sqrt{3}$ R30° LEED pattern was obliterated, normally about 2 min. The evaporation source, described in §II.4, sat 1 in. from the sample, and was heated resistively to 1200°C by 4A ac during evaporation. After the silicon deposition, brief annealing at 800°C yielded

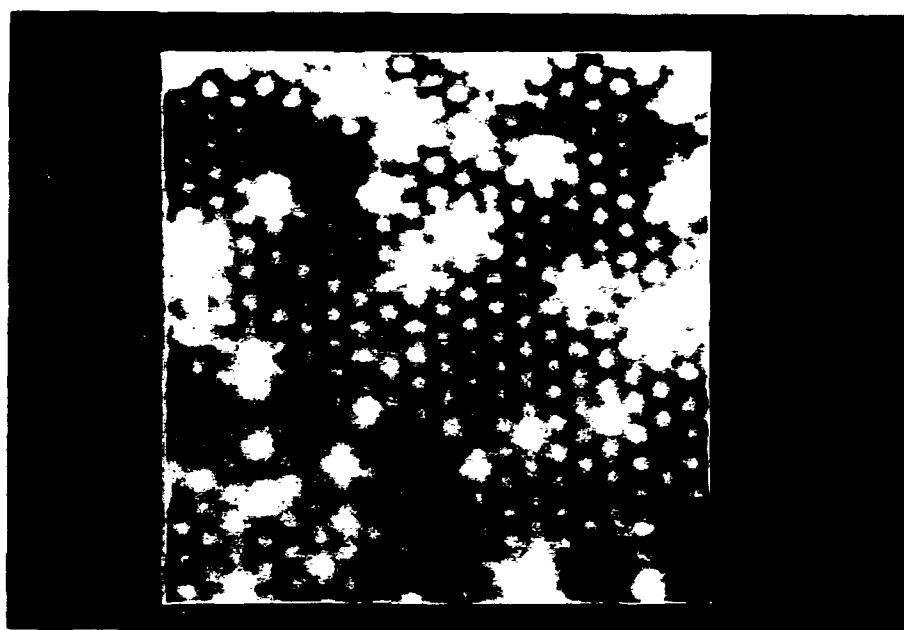


Fig. 5.2      $100 \times 100 \text{ \AA}$  STM image of a surface prepared by sputtering boron onto clean, As-doped Si(111). Tip bias = -2.5V, 1nA.

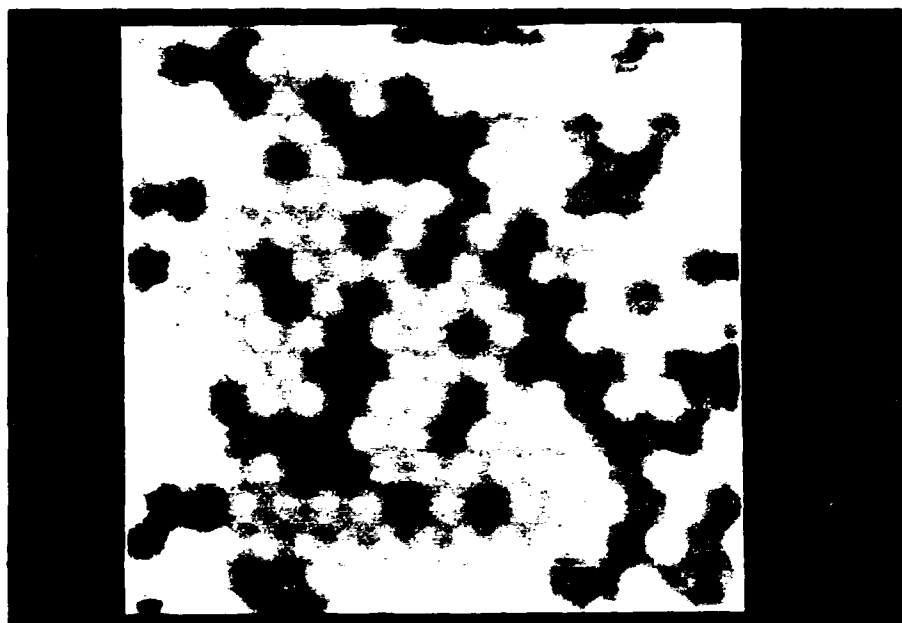


Fig. 5.3      $100 \times 100 \text{ \AA}$  STM image of a surface prepared by evaporating Si onto a B-terminated  $\sqrt{3} \times \sqrt{3} R30^\circ$  surface and annealing briefly. Tip bias = -1.0V, 1nA.

a  $7\times 7$  LEED pattern. Momentary heating at  $950^{\circ}\text{C}$  then transformed the surface to  $\sqrt{3}\times\sqrt{3}\text{R}30^{\circ}$ , which was examined under STM. As shown in fig. 5.3, this procedure raises the proportion of bright adatoms in the images up to 80%.

A precise measurement of the absolute boron coverage is not available here. Nuclear reaction analysis of the  $\text{B}(\text{p},\alpha)$  reaction does not offer sharp depth resolution, (Fe86) so such a measurement would not separate the surface signal from that arising from the possibly substantial subsurface boron presence in each of the preparations employed here. Auger spectroscopy presents the opposite problem; the sharp depth resolution of that technique for boron (Da76) requires a knowledge of the vertical boron position for an absolute coverage measurement. It is still possible to compare relative coverages. Fig. 5.4, for example, shows an Auger spectrum of an annealed boron-terminated sample, as shown in displayed in fig. 5.1. Fig. 5.5 shows a spectrum following external boron deposition, which in this case resulted in a higher proportion of dark sites in the STM images, and also enhanced the boron KLL peak. The boron peak is considerably attenuated in the spectrum of fig. 5.6, acquired after Si reevaporation on a  $\sqrt{3}\times\sqrt{3}\text{R}30^{\circ}$  surface. The Auger measurement is routinely performed to verify that the contamination level of each surface is no higher than that of "clean"  $\text{Si}(111)7\times 7$ .

In general, then, increased boron concentration at the surface yields more dark adatoms, and increased silicon concentration yields more bright ones. Thus, we associate the dark adatoms with the presence of boron, and the bright ones with its absence. It has therefore proven possible to prepare



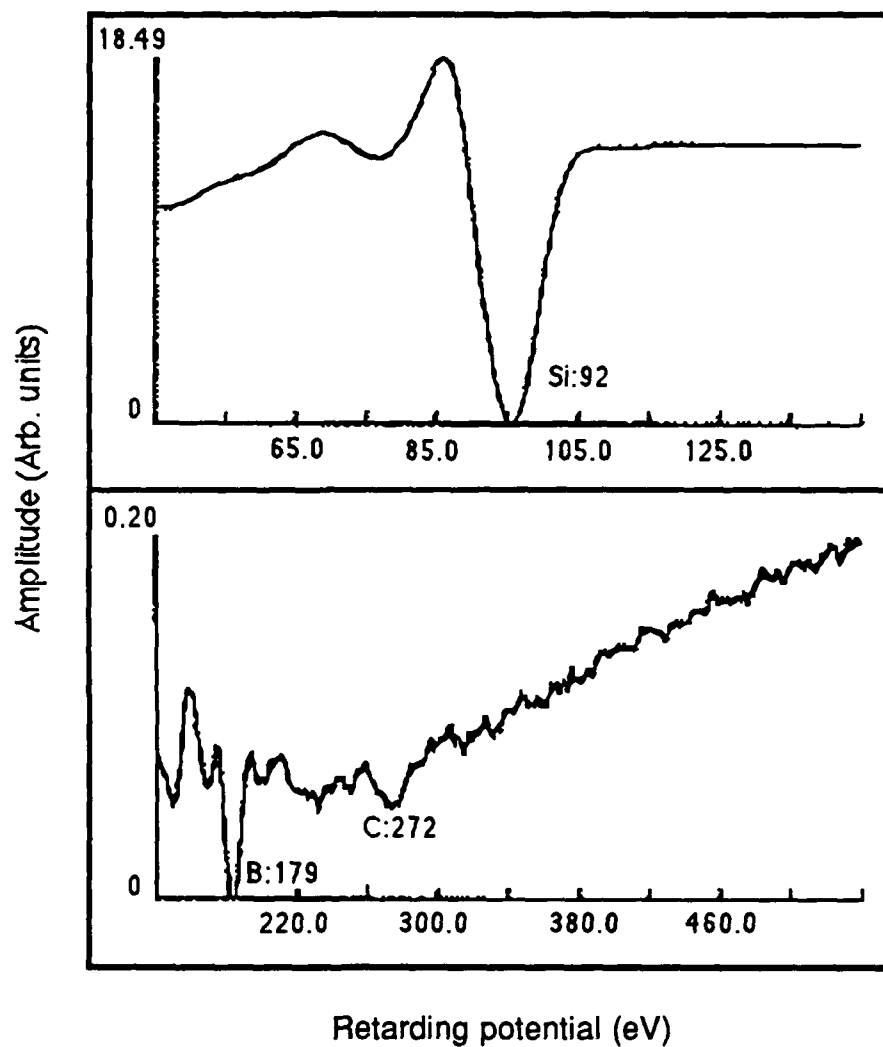


Fig. 5.4: Retarding field Auger spectrum of Si(111)- $\sqrt{3}\times\sqrt{3}$ R30°-B, prepared by annealing a heavily-B-doped crystal. Peak height ratio is Si:B:C = 18.49:0.08:0.05.

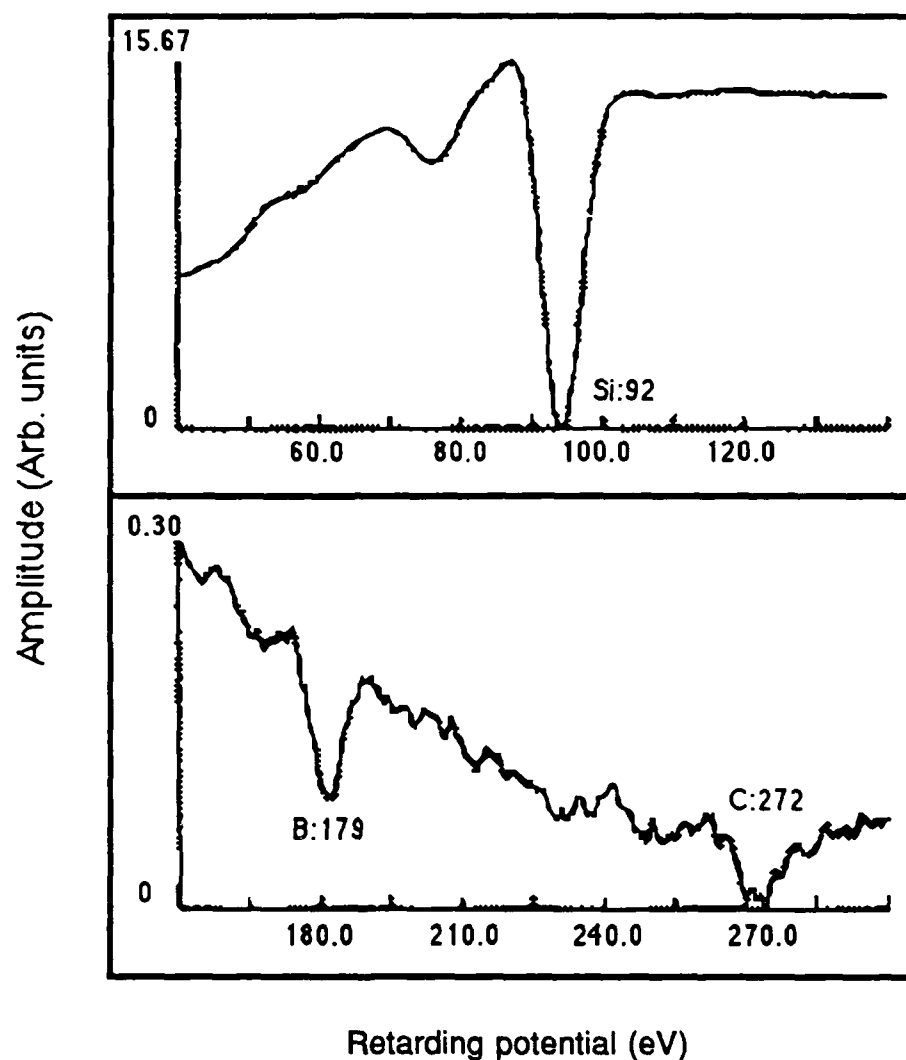


Fig. 5.5: Retarding field Auger spectrum of a surface of the type displayed in fig. 5.2, prepared by sputtering B on clean Si(111). Peak height ratio is Si:B:C = 15.67:0.14:0.08.

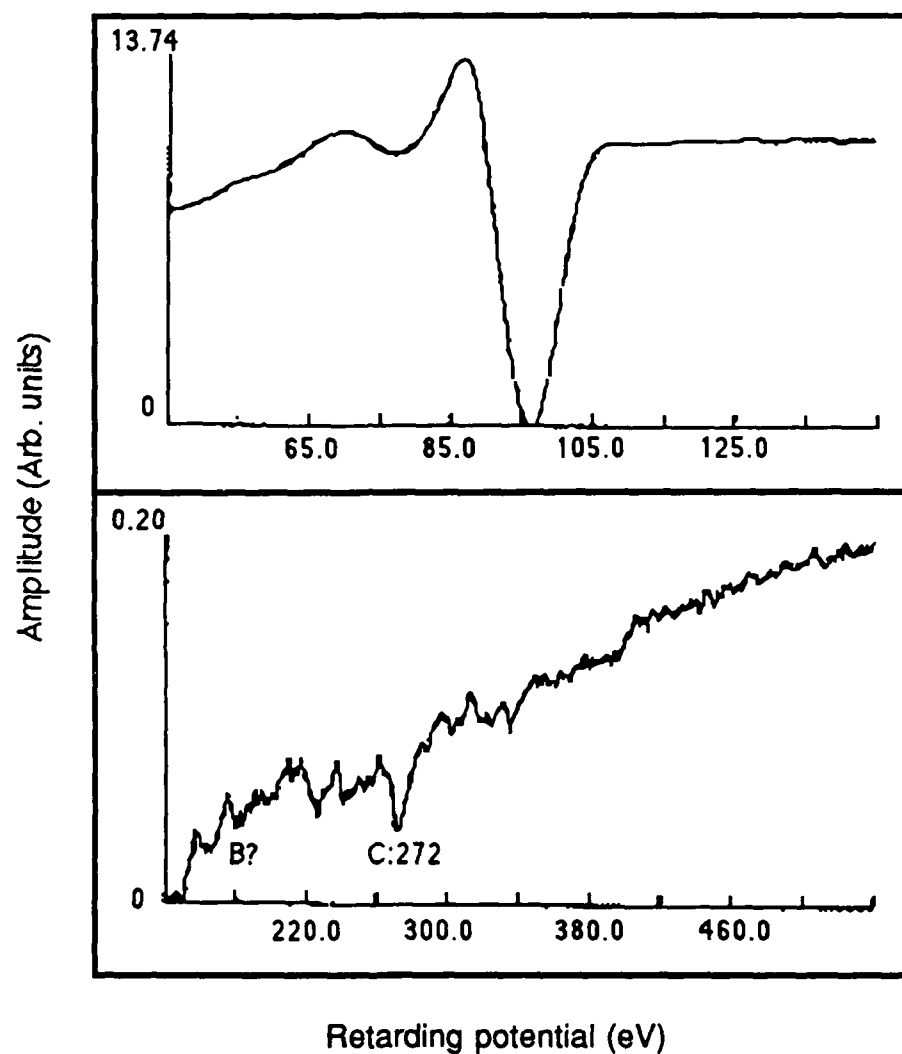


Fig. 5.6: Retarding field Auger spectrum of a surface of the type in fig. 5.3, prepared by reevaporating Si on a B-terminated surface. Note the suppression of the B peak despite the persistence of  $\sqrt{3} \times \sqrt{3}$  symmetry.

an inhomogeneous surface incorporating two distinct types of atomic sites, to use the STM to distinguish these two sites and identify one with the presence of a dopant, and to control the overall dopant concentration at the surface by tuning the parameters of sample preparation.

With these determinations accomplished, we can address the more fundamental question of the underlying reasons for the appearance of these images and the consistently brighter appearance of one type of site. This question motivates the remainder of the work in this chapter. As a starting point, the surface structure should then be understood as fully as possible; in particular, the site occupied by boron atoms must be determined. As in the case of gallium termination, the above images alone do not determine the actual position of the impurity or the complete topology of the reconstruction with subsurface relaxations.

## V.2 Surface Structure

### V.2.1 Observations

We have prepared mixed-phase surfaces using all three preparations of the preceding section. With the exception of the first preparation, simple annealing of the heavily-doped sample, sharp interfaces between  $7\times 7$  and  $\sqrt{3}\times\sqrt{3}R30^\circ$  domains could be observed in STM images. Determination of the lateral adatom registry could then proceed according to the prescription of §IV.1. Figs. 5.7-9 present such an interface, a corrugation trace, and a model for the interface.

These data indicate adatom occupation of the three-fold filled site. We note, however, that near the phase boundary, the surface is silicon-rich,

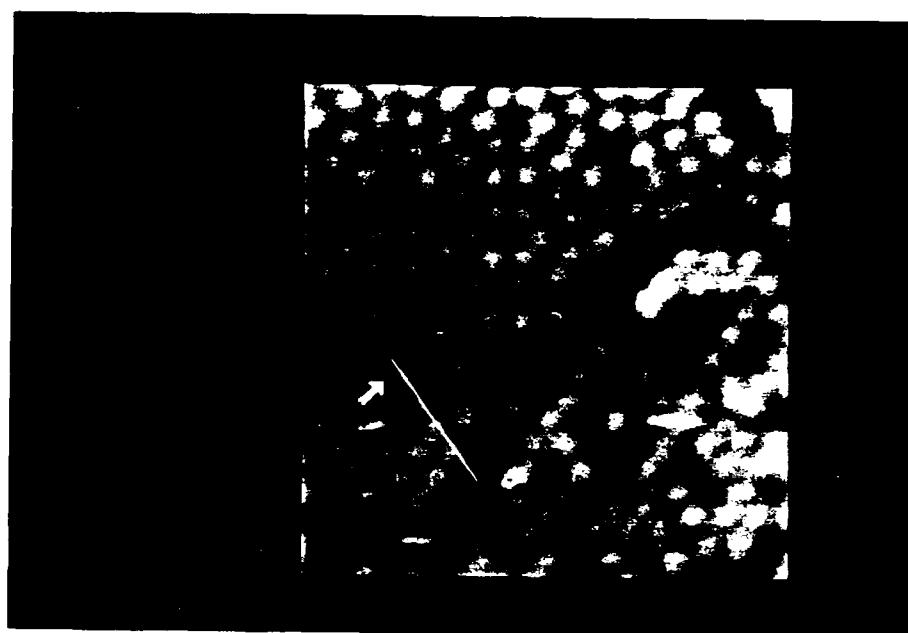


Fig. 5.7  $100 \times 100 \text{ \AA}$  STM image showing an interface between  $7 \times 7$  and  $\sqrt{3} \times \sqrt{3} R30^\circ$  domains, where B has been deposited by sputtering. Tip bias =  $-1.3 \text{ V}$ ,  $1 \text{ nA}$ .

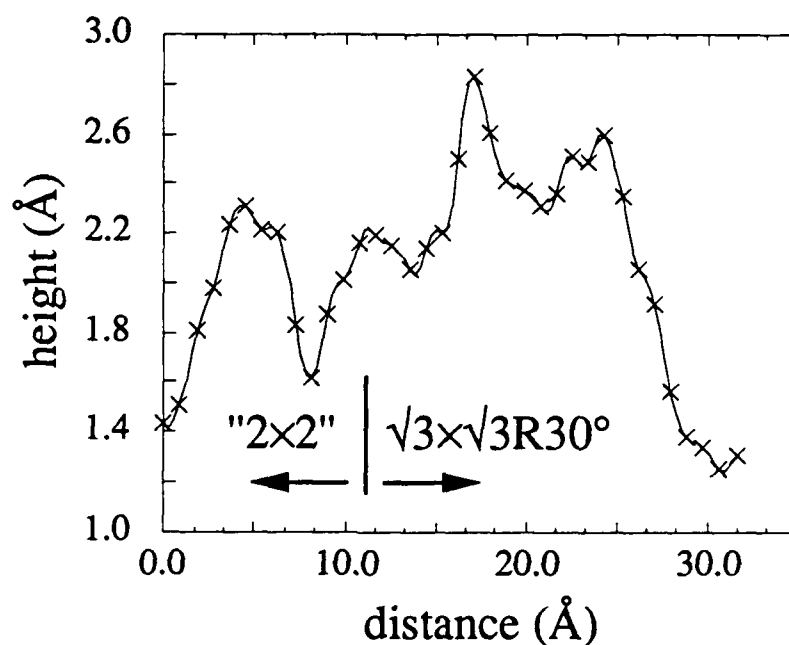


Fig. 5.8: Corrugation trace across the interface in fig. 5.7, separating a region of  $\sqrt{3}\times\sqrt{3}$  filling and one of local  $2\times 2$  filling characteristic of the  $7\times 7$  reconstruction. The equal spacing of lateral adatom positions indicates that the adatoms on either side of the interface adopt the same binding site.

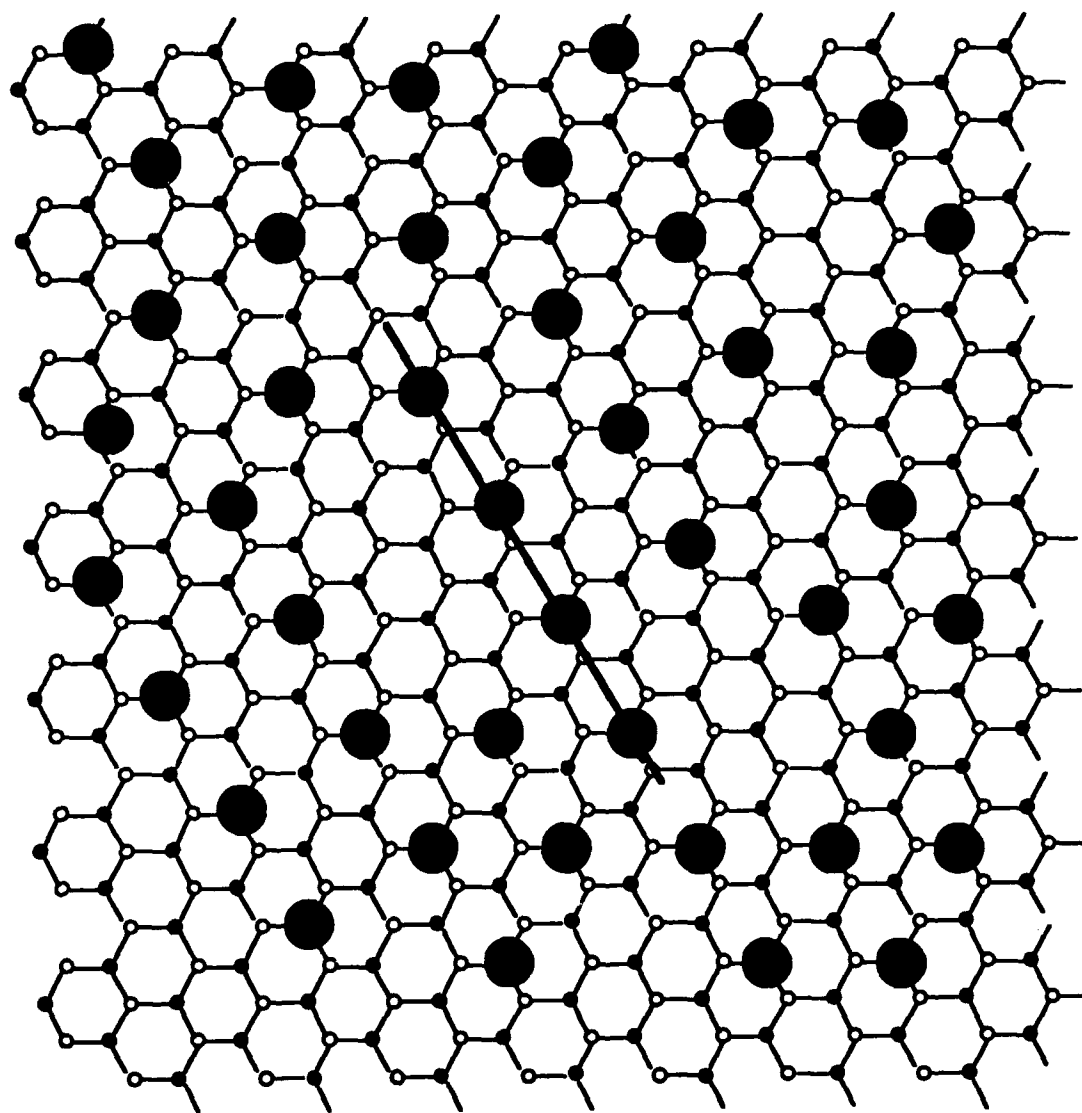


Fig. 5.9: Model for the phase boundary in fig. 5.7. The heavy line is the path of the corrugation trace in fig. 5.8.

and the  $\sqrt{3}\times\sqrt{3}R30^\circ$  region consists predominantly of bright, boron-free sites. Therefore, this analysis actually demonstrates that silicon adatoms on a silicon substrate occupy the  $T_4$  binding site in the  $\sqrt{3}\times\sqrt{3}R30^\circ$  configuration. In order to extend the analysis to substantially boron-occupied  $\sqrt{3}\times\sqrt{3}R30^\circ$  regions, we suggest that if the adatoms in such a region occupied hollow sites instead, then line defects should separate  $T_4$  and  $H_3$  regions. We have searched for and detected line defects within  $\sqrt{3}\times\sqrt{3}R30^\circ$  regions, but in every case the registry was preserved across the defects.

Local mixing of reconstructions on a small scale can be observed by preparing a heavily boron-doped sample according to the first technique of the previous section, but terminating the annealing after the  $7\times 7$  reconstruction has formed and before the  $\sqrt{3}\times\sqrt{3}R30^\circ$  LEED pattern has sharpened. The LEED pattern at that point displays strong first-order spots, but only very weak additional patterns. It has previously been observed that a " $1\times 1$ " LEED pattern, which reflects an absence of long-range coherence, may still arise from a surface with considerable short-range order. (Be86) STM images of this type of surface then offer a snapshot of a surface frozen in the midst of a transformation.

Fig. 5.10 presents such an image, taken adjacent to an atomic step, with  $5\times 5$  and  $7\times 7$  unit cells as indicated. At this level, the STM detects locally ordered regions that would be undetectable by diffraction techniques that sample an area larger than the characteristic domain size. Despite the breakdown of long-range coherence, the adatom registry across phase



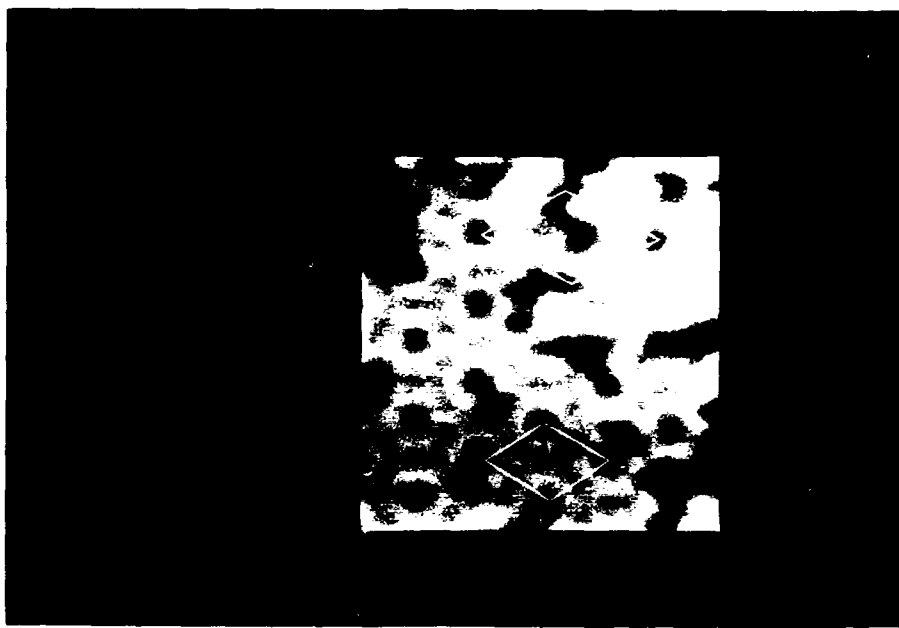


Fig. 5.10 STM image of a region with both 7x7 and 5x5 reconstruction. The larger unit cell indicated corresponds to the former structure. The surface was prepared by annealing a heavily B-doped Si(111) crystal partially.

boundaries is found to be consistent even in this somewhat disordered regime.

Apart from the adatom binding site, one additional piece of structural information can be gleaned from analysis of STM data. Since the tunneling images must reflect the full symmetry of the surface, the assigned boron position must accord with each observed symmetry. First, each visible adatom occupies a three-fold symmetric position about an axis perpendicular to the (111) face. In addition, the adatom layer and outer substrate double layer are symmetric under reflection along the short diagonal of the  $\sqrt{3} \times \sqrt{3} R30^\circ$  unit cell. The preservation of this symmetry is demonstrated by corrugation traces about the long diagonal of the unit cell, as shown in fig. 5.11. In these line cuts, the principal maxima represent the adatoms, while the secondary peaks occur at the saddle point, where the tip crosses the short diagonal. The reflection symmetry about that axis is manifested in the consistent occurrence of the secondary peak precisely midway between adatoms.

#### V.2.2 A picture of surface B doping

While the conclusions from the STM data above do not completely determine the structure of the reconstruction, they do reduce the possible binding site for boron to the two shown in fig. 5.12, which are consistent with both  $T_4$  adatom binding and the observed symmetries. In the first case, boron would occupy the  $T_4$  adatom position itself, following the pattern of the other Group III elements. In the second case, the boron atom would sit directly underneath a silicon adatom in a novel structure. We

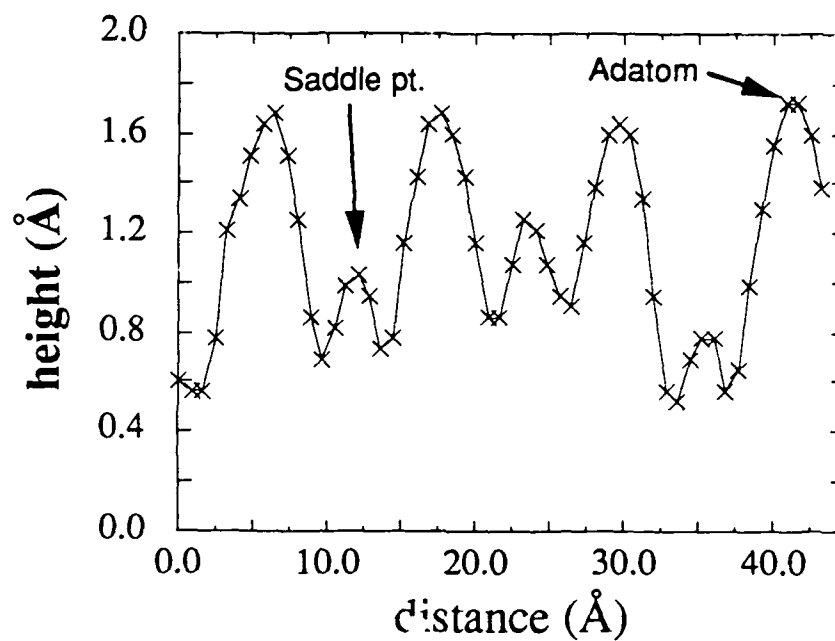


Fig. 5.11: Corrugation trace along the long diagonal of the  $\sqrt{3}\times\sqrt{3}R3C^{\circ}$  unit cell in fig. 5.2. The principal maxima occur on adatom sites. Note that the secondary peaks, which represent saddle points, occur exactly midway between the adatom positions.

## Boron on Si(111)

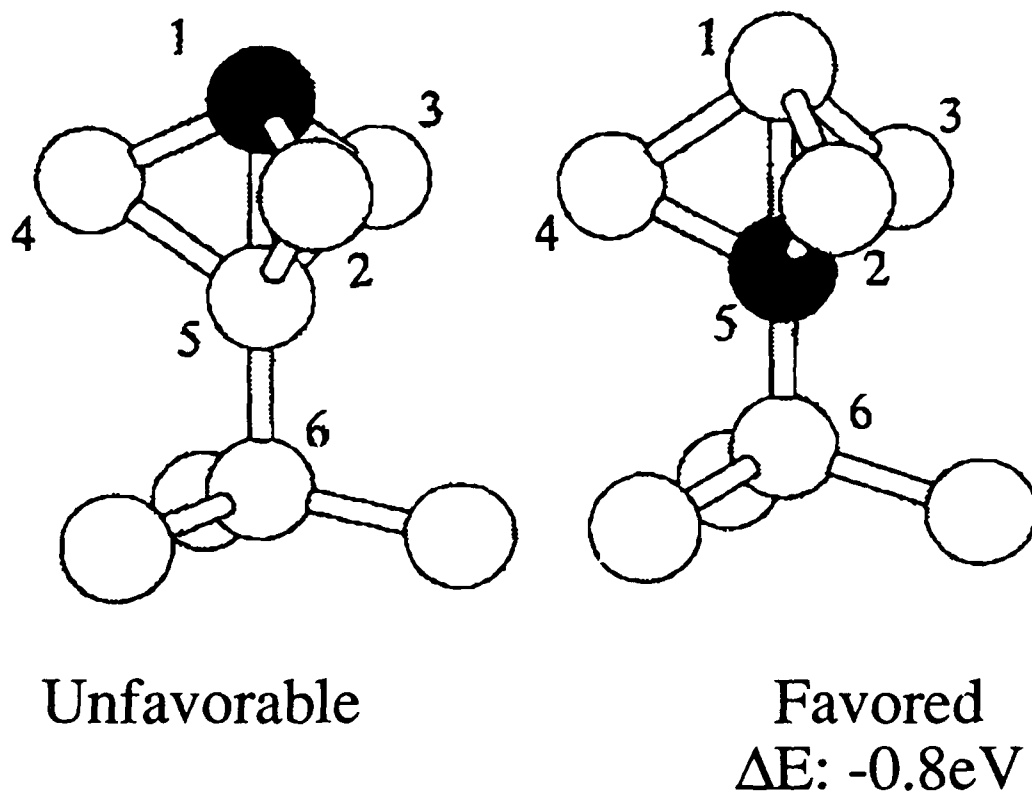


Fig. 5.12: Relaxed  $\sqrt{3}\times\sqrt{3}$  geometries for a boron atom (shaded solid) adsorbed (left) in the T<sub>4</sub> position, and (right) in the B<sub>5</sub> position. Both are consistent with the full symmetry observed in STM images, but LDA calculations place the second structure at a far lower energy.

## Unrelaxed B Substitution

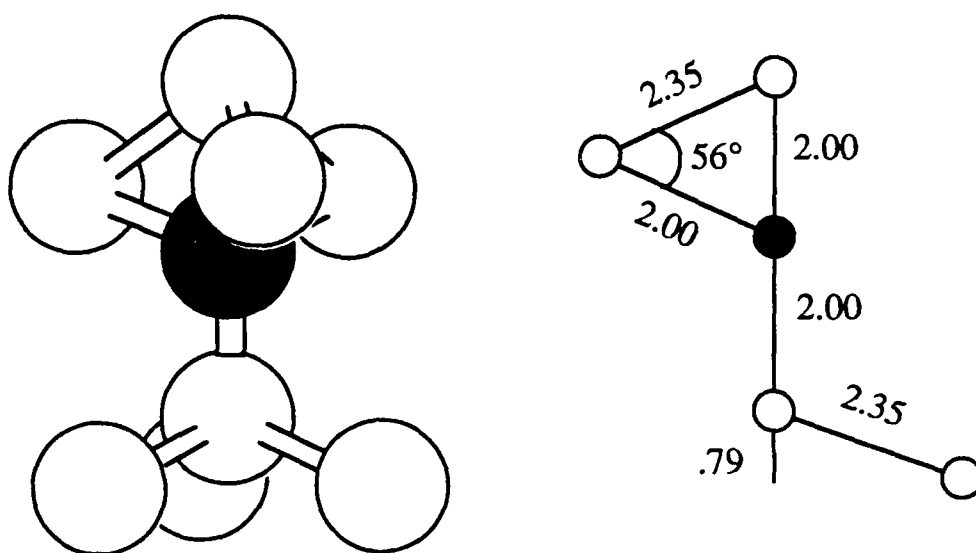


Fig. 5.13: Topology of B substitution in the B<sub>5</sub> site (solid shading). The unrelaxed bond lengths are taken as the sum of bulk covalent radii.

refer to the boron site in the latter case as  $B_5$ . It was shown in §III.2 that Si, Al, Ga, and In adatoms on Si(111) adopt the first structure after a relaxation that adjusts bond angles in the outer layer in the direction of the favored tetrahedral topology to relieve that layer's tensile stress only partially, at the expense of transferring stress to the second double layer and compressing the bond lengths within the outer double layer. A compromise is reached, but stresses remain.

However, examination of fig. 5.13 reveals that if boron sits underneath the adatom, then because of the small atomic size of boron, even the *unrelaxed* atomic positions fall in such a way that the bond angles of the outer layer are already favorable, and the adatom's nearest neighbors do not have to undergo further unfavorable, inward compression. Thus, minimal tensile stress need be transferred to deeper layers, and the awkward compromise assumed by the Al-, Ga-, and In-terminated surfaces is unnecessary for the B-terminated surface.

A more quantitative justification of this picture resulted from total energy calculations of the type described in §III.2, which compared the relaxed geometries of the two possible boron adsorption sites in fig. 5.12. The structure with boron occupying the lower,  $B_5$  position, emerged lower in energy by .93eV per adatom cell, or .31eV per  $1\times 1$  cell. (Be89b) To illustrate the enormity of these energies at this scale, previous *ab initio* calculations have placed the energy difference between unreconstructed Si(111) and a  $2\times 2$  adatom-covered surface, which is estimated to lie close in energy to the  $7\times 7$  reconstruction, at .27eV per  $1\times 1$  cell. (Va87a, Me89a)

In view of the strong favoring of the second structure in fig. 5.12, together with the presence of an annealing step in each surface preparation in this work, these theoretical considerations would strongly indicate  $B_5$  binding for boron. In this picture, all of the observed adatoms in the tunneling images of  $\text{Si}(111)\sqrt{3}\times\sqrt{3}\text{R}30^\circ\text{-B}$  are silicon. The darker adatoms would sit directly above a boron atom, whereas the bright ones would not. We shall therefore refer to the dark sites as "boron-occupied," and to the bright sites as "boron-free." Thus, adsorbed boron indeed breaks the pattern of  $T_4$  adatom occupation set by its Group III cousins.

A consequence of this picture, apparent from fig. 5.13, is that the adatoms at boron-occupied sites should lie  $\approx 0.4\text{\AA}$  below those at boron-free sites. We saw earlier that the contrast between gallium and silicon adatoms on the  $\text{Si}(111)\sqrt{3}\times\sqrt{3}\text{R}30^\circ\text{-Ga}$  surface disappears above  $\pm 1.5\text{V}$  bias, where the integrated densities of states at the two sites should begin to converge. The vertical gallium and silicon adatom positions were expected to be similar. In contrast, the greater topographic contrast in the two corresponding types of sites on  $\text{Si}(111)\sqrt{3}\times\sqrt{3}\text{R}30^\circ\text{-B}$  may account for the persistence of their observed distinguishability in images acquired in a similar bias range. However, at lower biases, the difference in the tip height between the two types of sites exceeds  $1\text{\AA}$ ; in that case, the measured corrugation cannot be explained entirely by the novel boron adsorption topology. In that bias regime, we have already seen that the contrast between silicon and gallium adatoms on  $\text{Si}(111)\sqrt{3}\times\sqrt{3}\text{R}30^\circ\text{-Ga}$  appeared to be affected strongly by surface states. Therefore, we turn next to an

examination of the electronic properties of the tunnel junction between the tip and the boron-terminated surface.

### **V.3 Local tunneling spectroscopy**

#### **V.3.1 Atom-resolved spectra and surface states**

The principles and operating procedures for the spectroscopic measurements are defined in the Chapter II. We have contrasted the electronic properties of the tunnel junction associated with the two types of sites on  $\text{Si}(111)\sqrt{3}\times\sqrt{3}\text{R}30^\circ\text{-B}$  by interrupting 2-d scans at random, fixing the lateral and vertical positions of the tip, sweeping and modulating the dc tip bias, and recording both the tunnel current and differential conductivity as a function of tip voltage. The tunnel current was read directly from the buffered preamp output, and the differential conductivity was recorded by a lock-in amplifier, as described in §II.4. The scanning software indicated precisely where, in relation to the surface topography, the spectrum was acquired. In this way, the I-V characteristic of a particular pixel could be acquired. Of the many tunneling spectra acquired at random locations, those that were taken with the tip directly above an adatom were selected and examined.

This method of acquisition and analysis differs from some previously reported approaches in sampling a highly local region and avoiding spatial averaging of spectra. The drawback of this approach is its frequent inconvenience, for it demands a precise definition of the parameters observed, as follows. Even when atomic resolution images are obtained, the tip structure is undetermined and uncontrollable, and perfect conical





Fig. 5.14 80x80Å topographic image (left) and dI/dV image (right) showing the effect of an asymmetric tip on conductivity measurements. The arrows indicate a 7 o'clock shadow near bright adatom sites resulting from an asymmetric tip. Tip bias = -1.4V, 1nA.

symmetry at the end of the tip is rarely realized. Commonly, a broken tip symmetry reflects subtly in tunneling images. For example, fig. 5.14 indicates the severe effect that such a non-conical tip structure can have on a differential conductivity measurement. As a result of the broken tip symmetry, atomic sites in the  $dI/dV$  image are shadowed. If such a topograph were interrupted at random for spectroscopic scans, discrepancies might result from the broken symmetry.

We have found that the analysis of tunneling spectra without any regard to the structural pathology of the tip results in a plethora of seemingly irreconcilable data. We therefore narrow the pool of acceptable spectra to those which derive from *both* topographic and  $dI/dV$  images that do not display any breaking of the three-fold symmetry of the LEED pattern. In practice, this is a very stringent restriction that removes over 85% of the data pool. Nevertheless, it is requisite to any meaningful definition of the measurement, and after this selection, we find empirically strong consistency among spectra corresponding to similar atomic sites.

Previous disclosures of local tunneling spectra have avoided this inconvenience by averaging electronic information over a larger area. In a recent study of aluminum impurities on Si(111), the tunneling spectra presented reportedly represented an average of many spectra acquired in one unit cell. (Ha88b) An alternative scheme, reported in studies of Si(111)-As and various reconstructions of Si(111) and Ge(111), utilized a "dull" tip that yielded topographs of poor spatial resolution. (Be88, 89a) Either method would gain consistency by weakening the definition of the measured quantity, at the expense of the lateral resolution that we prefer here.

Typical tunneling spectra for each adatom type are displayed in fig. 5.15. According to the convention introduced in §II.2, the plotted quantity is normalized to the total conductivity in order to remove some of the distance dependence, and so that the plotted quantity is dimensionless.

Both spectra display an occupied state peak at a tip bias of +1.5-1.8V. Peaks at this energy have previous been associated with the occupation of back-bonding orbitals (No84, 86) and would therefore be expected to appear on both boron-occupied and boron-free sites. While such an assignment here would apparently be consistent with previous observations, it is difficult to demonstrate conclusively. First, it was pointed out in §II.1 that data at positive tip bias may be dominated by unoccupied tip bands, and this phenomenon has recently been demonstrated explicitly in another system. (K189) Second, the traditional assignment of the spatial distribution of the back-bond state places most of the electron density between adatoms. A conductivity image at the bias voltage of the spectral peak would therefore be unable to distinguish electron state density from the topographic background discussed in §II.1.

Finally, even if the observed spectral peak does originate from a back-bonding surface state, the meaning of the exact peak position for a surface state with  $k_{\parallel} \neq 0$  localized between adatoms in a one-dimensional spectrum acquired directly above adatoms would still be undetermined. In view of these considerations, we acknowledge the consistency of the appearance and position of this peak with previous work, but we shall refrain from developing any arguments that depend on an assignment of this

# $\text{Si}(111)\sqrt{3} \times \sqrt{3}\text{R}30^\circ\text{-B}$

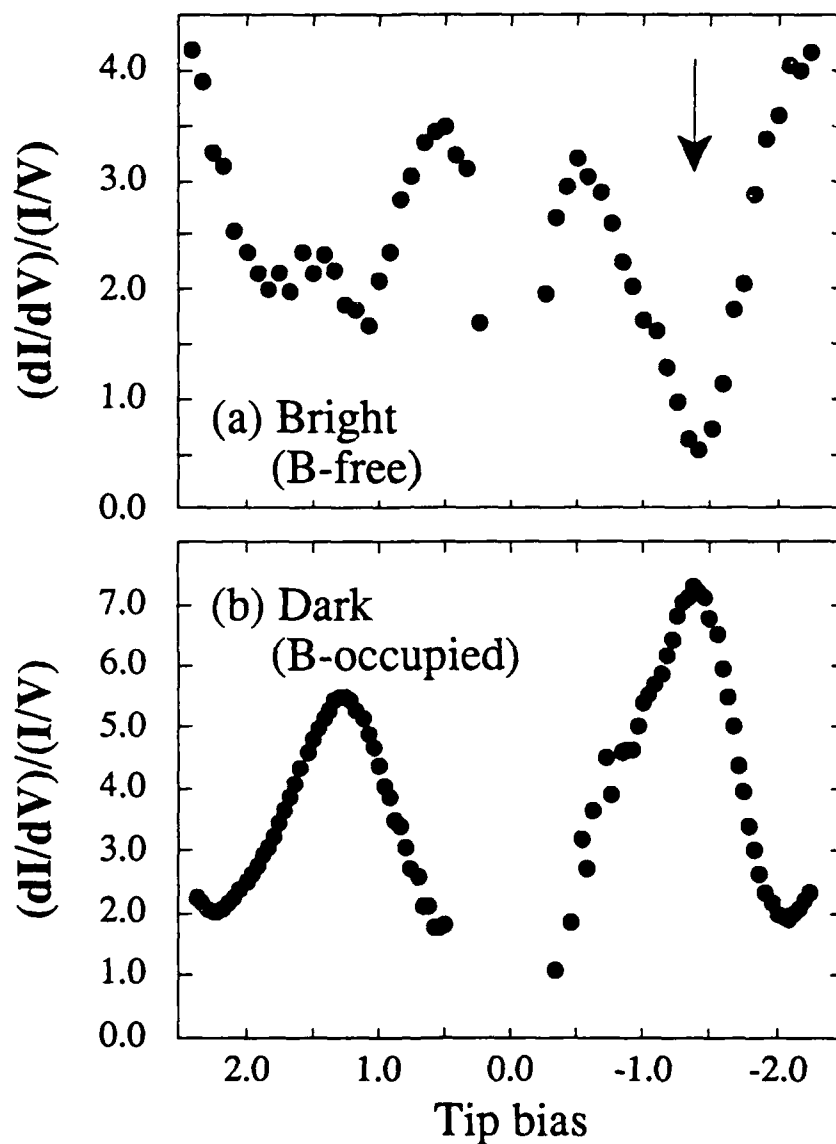


Fig. 5.15: Tunneling spectra recorded over (a) bright, boron-free, and (b) dark, boron occupied sites on a surface of the type displayed in fig. 5.1. The arrow indicates -1.4V tip bias. Negative tip bias represents electron tunneling into unoccupied surface states.

spectral feature. We shall concentrate instead on features that distinguish the two types of sites.

The spectrum from the boron-free site shows significant structure in the density of states within 0.5eV on either side of the fermi level, as expected for a silicon adatom on a silicon double layer, with its partially occupied dangling orbital. (No86) The presence of this feature on the boron-free sites and corresponding absence above the boron-occupied sites would certainly enhance the bright appearance of the former sites down to low tip biases regardless of polarity, as observed.

Spectra acquired above the dark atoms display a prominent peak at -1.4V tip bias. Since the bright adatom spectra display a minimum at the same bias, indicated by the arrow, the spatial distribution of an unoccupied surface state at this energy may be revealed by simultaneously acquiring both a conventional, constant-current topograph and an image of the differential conductivity at -1.4V tip bias. The resulting pair of images is presented in fig. 5.16. The second image represents the output of the lock-in amplifier as a function of lateral position, in response to a small, fast modulation (25mV rms, 6.25kHz) of the tip bias voltage. Brighter shading in this image indicates higher differential conductivity. It is apparent that peaks in the differential conductivity at this bias occur directly atop dark atoms, while troughs occur directly atop bright ones.

As with the tunneling spectra, it is necessary to define the constraints on the interpretation of the dI/dV image in order to ensure that topographic background effects are not interpreted erroneously as surface state features. First, we confine the analysis to a comparison of the magnitude and spatial

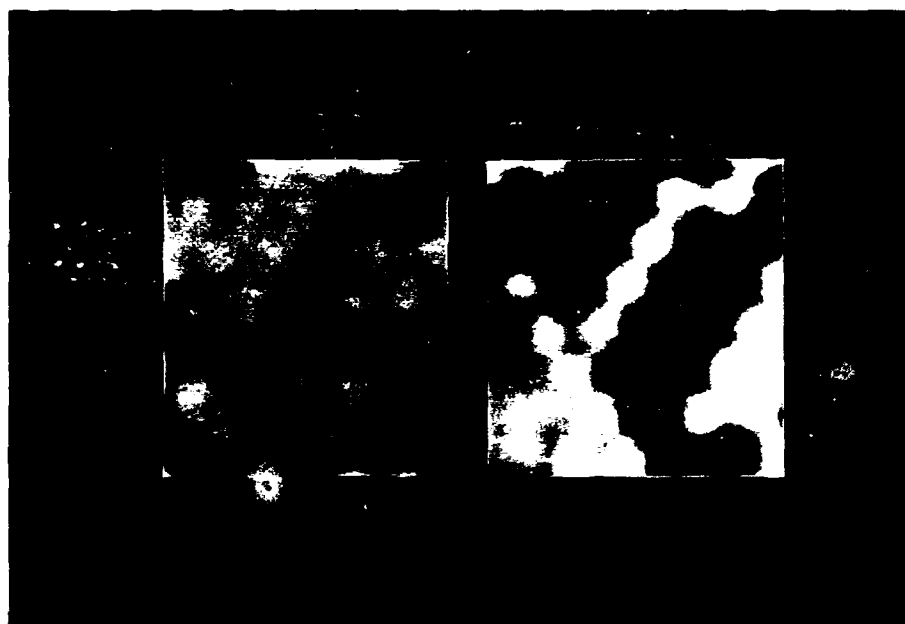


Fig. 5.16 40x40Å STM topographic image (left) and dI/dV image (right) recorded at -1.5V tip bias and 1nA.

curvature of the imaged quantity directly over atomic sites. In §II.1 it was indicated that even in the absence of surface states, purely topographic effects would cause the  $dI/dV$  image to appear as the reverse of the topography. Thus, the halos around the atomic positions in the boron-free regions of the  $dI/dV$  image may well be of topographic origin; accordingly, we do not attempt to infer any interatomic orbital distribution from the relationship between topographic maxima and minima in the  $dI/dV$  image.

With the analysis of a  $dI/dV$  image now confined to a comparison of the two types of topographic maxima, it remains to address dependence of the differential conductivity on tip-sample distance. It was pointed out in §II.1 that even in the absence of vertical topographic variation between two types of atomic sites with distinct local electronic structures, the distance dependence of the  $dI/dV$  could distort the conductivity image. The prescription was found to be a suitable normalization of the differential conductivity. We note that the very procedure of imaging  $dI/dV$  with the feedback operating continuously automatically yields the normalized quantity  $(dI/dV)/(I/V)$ , owing to the constancy of  $I$  and  $V$  during scanning. We therefore intentionally acquire the topographic and  $dI/dV$  images under identical bias and current conditions in order to suppress the contribution of the "background" in the differential conductivity image, which results from changes in the transmission probability with tip height and bias, to the contrast between the two types of atomic sites.

We may now use fig. 5.16 to compare the differential conductivities associated with the two distinct types of topographic maxima. The line cut through the  $dI/dV$  image in fig. 5.17 demonstrates that at  $-1.4V$  tip bias,

## Bias-dependent dI/dV profiles

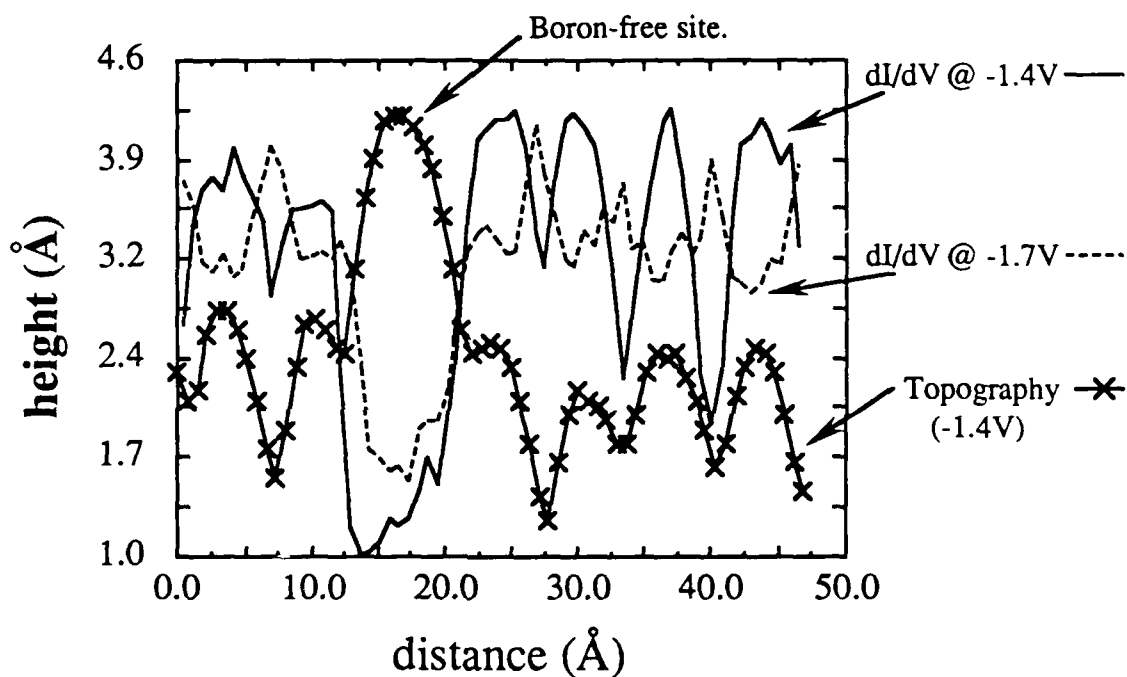


Fig. 5.17: Comparison of corrugation profiles from topographic and dI/dV images on Si(111) $\sqrt{3}\times\sqrt{3}$ R30°-B, acquired along a primitive axis. Local topographic maxima represent atomic sites. At -1.7V tip bias, spatial conductivity *maxima* occur on topographic *minima*. At -1.4V, local maxima in both dI/dV and topography coincide on dark, boron-occupied sites, but deep dI/dV minima occur at the bright, boron-free sites. The dI/dV profiles are scaled to arbitrary units.



electronic effects dominate topographic effects at the boron-occupied sites, for the spatial maxima in the differential conductivity at these sites correspond to the topographic maxima. At higher bias, a local minimum in  $dI/dV$  occurs at the atomic position, indicating a diminished influence of a surface state contribution at that bias and a dominance of the  $dI/dV$  image by the topographic "background" effect. The clear coincidence of topographic maxima with  $dI/dV$  maxima in fig. 5.16 emphasizes the influence of a surface state 1.4V above the fermi level. Having addressed the reasonable constraints on the interpretation of the data, we may infer the presence of an unoccupied surface state, 1.4eV above the fermi level, spatially localized atop the boron-occupied sites.

This identification, though deduced from tunneling data alone, follows qualitatively the pattern identified in fig. 3.4 on the basis of photoemission and theoretical studies of the Al-, Ga-, and In-terminated Si(111) surfaces. In each case, a dangling bond orbital was located  $\approx 1\text{eV}$  above the fermi level of the respective surface. As the position of this band signified the most dramatic difference from the band structure calculated for Si(111) $\sqrt{3}\times\sqrt{3}$ R30° with Si adatoms, the position of a dangling-bond peak in local tunneling spectra acquired on a surface incorporating both boron-free and boron-occupied sites might be expected to be the most dramatic distinction in the tunneling spectra associated with each site, if an individual dangling orbital is confined to an area of atomic dimension. Fig. 5.16 demonstrates that this confinement is realized. The distinction in the spectra of fig. 5.15 therefore represents the detection a shift in the energy of the dangling orbital on the atomic scale.

Recent calculations offer support for this picture. (Be89b) A consequence of the model for this surface discussed in §V.2.2 is that charge should be transferred to the boron atom in the B<sub>5</sub> site from the dangling orbital of the silicon adatom above, leaving the latter state empty. In particular, LDA calculations placed the unoccupied surface band on the top silicon adatoms 0.3eV higher than the half-occupied band of silicon adatoms on boron-free sites. Though this value falls short of the measured shift of the unoccupied state peak of  $\approx 0.9\text{eV}$  between the two spectra in fig. 5.15, the predicted and actual directions of the shift coincide. A discrepancy in the measured and predicted magnitudes should not be alarming, for in every system represented in fig. 3.4, LDA predictions fell short of the measured energy of the unoccupied state, while the qualitative predictions were still useful. Calculated contour plots for the unoccupied state that illustrate its strong localization have been presented previously. (Me89a)

Additional support for the assignment of peaks in the tunneling spectra comes from recent KRIPES and ARUPS measurements, which revealed unoccupied states at  $\Gamma$ -point energies of 0.5 and 1.3eV above the fermi level of a surface prepared by annealing heavily boron-doped Si(111), as above. (Ka89) The dispersion of the lower, unoccupied state resembled that of the lowest unoccupied band of clean Si(111)7 $\times$ 7. The tunneling images and spectra suggest that the presence of that band originates from the boron-free sites on Si(111) $\sqrt{3}\times\sqrt{3}$ R30°-B. The close agreement of the  $\Gamma$ -point position of the second state with the strong unoccupied-state peak in the boron-occupied tunneling spectra corroborates both the STM's

detection of a surface state at that energy and that its sensitivity to that state's  $k_{||}=0$  component. Fig. 5.18 displays the measured band dispersions assigned to boron-occupied sites. The unoccupied surface state, with maximum intensity near the zone center, was assigned to the adatom dangling bond, while the occupied state, with minimal intensity near the zone center, was assigned as a back-bond state.

The spectroscopic data presented so far represent surfaces prepared according to one of the first two procedures described in §V.1; specifically, simple annealing or external boron deposition. As a result, the concentration of bright, boron-free sites was in each case below 25%. Fig. 5.19 presents tunneling spectra from surfaces at the opposite end of relative boron and silicon concentration, prepared by evaporating Si on a boron-terminated surface and annealing briefly according to the third procedure in §V.1. In the occupied-state region, the boron-free spectrum resembles that of clean Si(111)7×7, but the band positions are clearly perturbed strongly by the undetermined subsurface boron doping that results from this preparation.

The band movement should diminish in the unoccupied state region, where the dangling-bond orbitals should hybridize only weakly with bulk bands. In fact, the characteristic structure consisting of a minimum in the boron-free site spectrum and a maximum in the boron-occupied site spectrum still appears prominently and has shifted upward by less than 0.2eV. This observation establishes both the presence of the spectral structure throughout the range of surface boron concentrations attained under three distinct methods of preparation, while suggesting the possibility

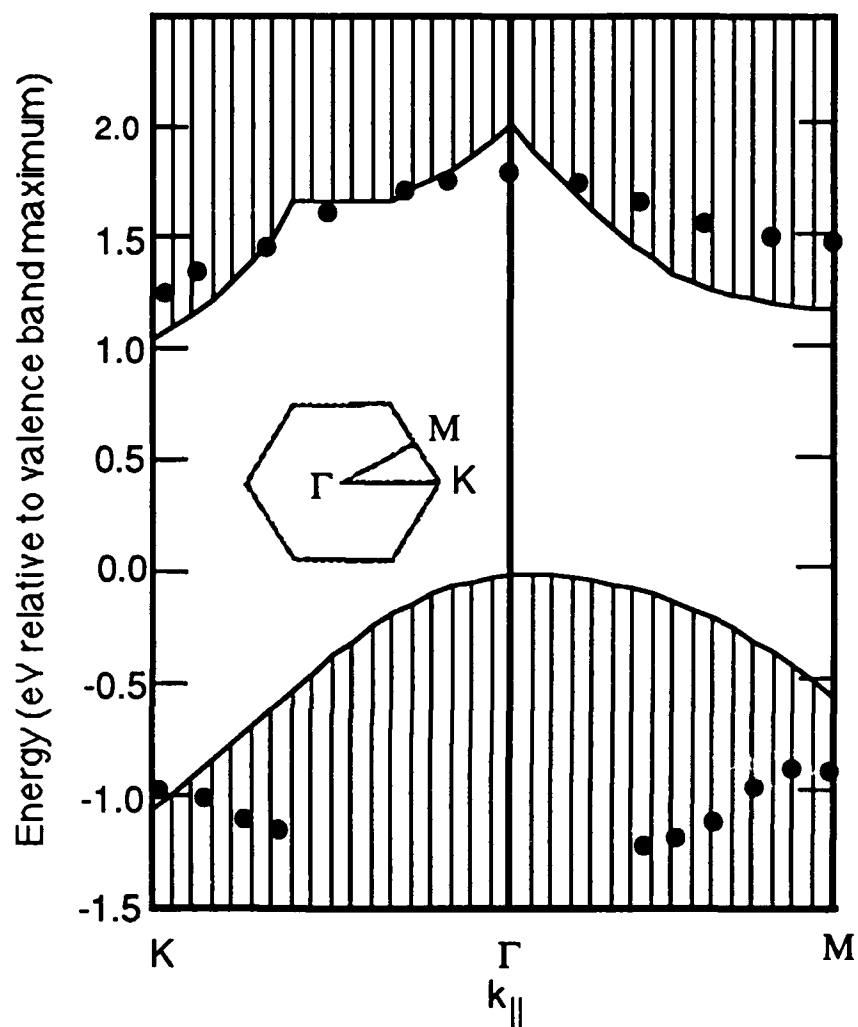


Fig. 5.18: Energy bands for Si(111) $\sqrt{3} \times \sqrt{3}$ R30°-B from photoemission and inverse photoemission. Surface states are dotted. The fermi level is taken 0.5eV above the valence band maximum. [Ka89, with permission]

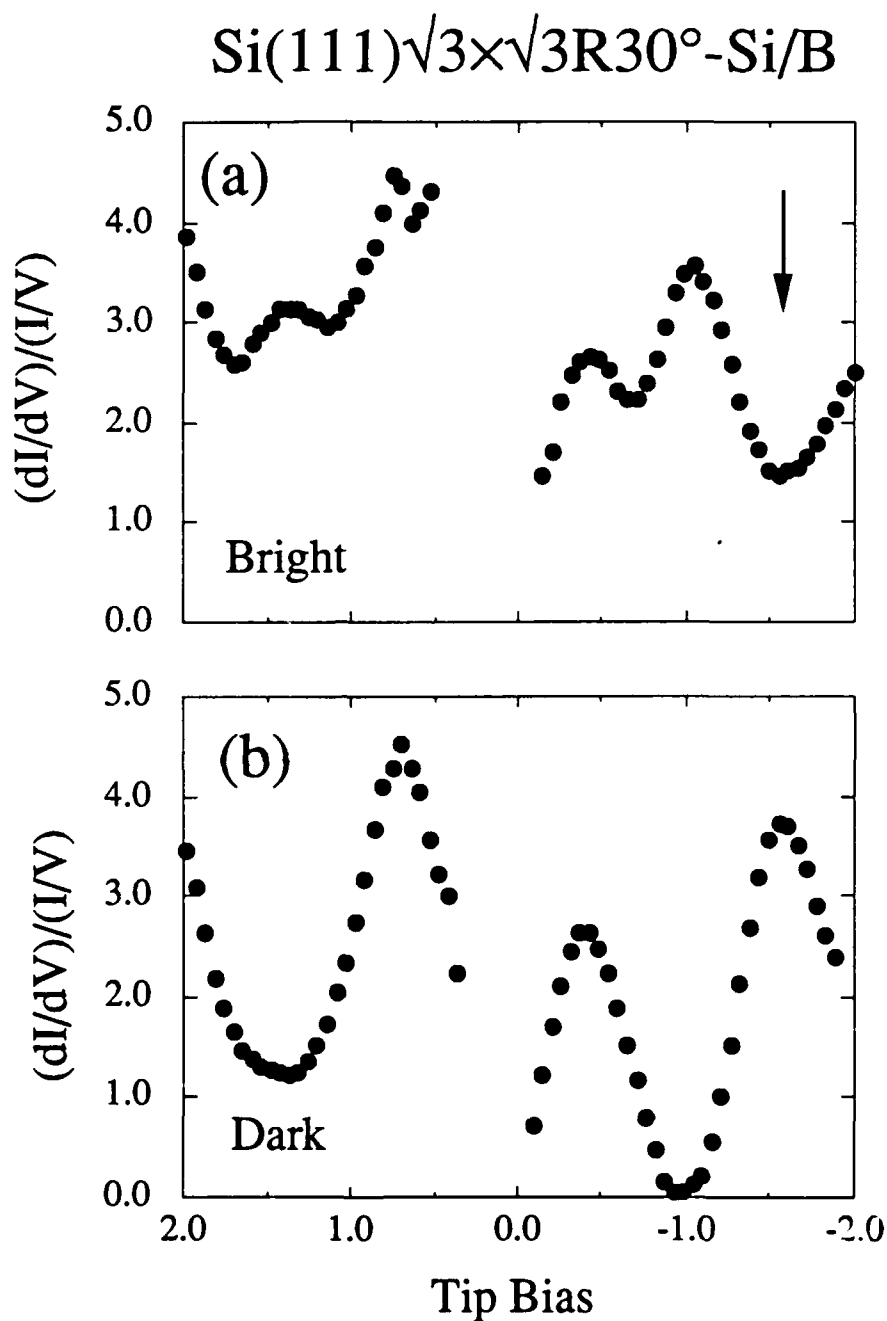


Fig. 5.19: Tunneling spectra recorded from a surface of the type in fig. 5.3, with predominantly, "bright" adatoms. The arrow indicates -1.55V tip bias.

of perturbing the tunneling spectra by adjusting boron doping levels. This surface, however, is not the ideal system with which to commence a study of surface band perturbations, for its preparation leaves the subsurface dopant distribution only poorly controlled. Furthermore, because clean Si(111) does not ordinarily reconstruct to the  $\sqrt{3}\times\sqrt{3}R30^\circ$  periodicity, the surface under examination here displays novel properties, which deserve closer investigation. The direction of the band movement is undoubtedly connected with the nature of this surface, which will be examined in §V.4 below.

Before speculating on the origin of the gross band movement and stabilization of an ordinarily unfavorable reconstruction, it is still worthwhile to investigate the possibility of perturbing the local band structure of Si(111) $\sqrt{3}\times\sqrt{3}R30^\circ$ -B through more modest, local variations in the surface doping environment. Returning to the surfaces that yielded spectra such as shown in fig. 5.15, we shall focus for the remainder of the section on the distinctive structures occurring 1.4eV above the fermi level, having now ascertained their origin.

### V.3.2 An atomic-scale tunnel diode

The surface boron doping level has been controlled in this work only in an average sense. The local dopant distribution resulting from the preparations employed here is a product of random diffusion processes. Still, the inhomogeneity engendered by this randomness offers a complete selection of local doping environments to be sampled by the STM's tip. In fig. 5.15, the differential conductivity measured above a boron-free site

reached a minimum at -1.4V tip bias, at which the value was near zero. In fact, we find that when a lone boron-free site is surrounded predominantly with boron-occupied sites, the differential conductivity measured above the boron-free site at -1.4V tip bias often becomes negative. The effect on a tunneling spectrum is illustrated in fig. 5.20.

The spatial distribution of the regions of negative differential conductivity may be revealed by recording both a constant-current topograph and a differential conductivity image at -1.4V tip bias, as in fig. 5.21. The method of acquisition and grey scale correspond to those described in the discussion of fig. 5.16, but the regions of negative differential conductivity are shown in white. The centers of negative differential conductivity appear to be independent and localized on isolated boron-free sites. We can therefore define a specific current-voltage characteristic of the STM's natural tunnel junction according to the presence of a particular atom on the surface underneath the tip. For example, fig. 5.22 displays I-V curves for adjacent boron-occupied and boron-free sites in the case of negative tip bias. The anomalous negative resistance in the latter curve is reminiscent of a tunnel diode.

The appearance of the conductance anomaly in this system apparently resulted from a small perturbation in the local dopant distribution, but the phenomenon itself is dramatic. From the standpoint of the interpretation of tunneling spectra, the conductance anomaly unambiguously demonstrates that the differential conductivity, normalized or not, is not simply a map of the surface density of states, but rather reflects the tip-sample-barrier system. More practically, the tunnel diode, which was the first practical

## Tunnel diode from surface doping

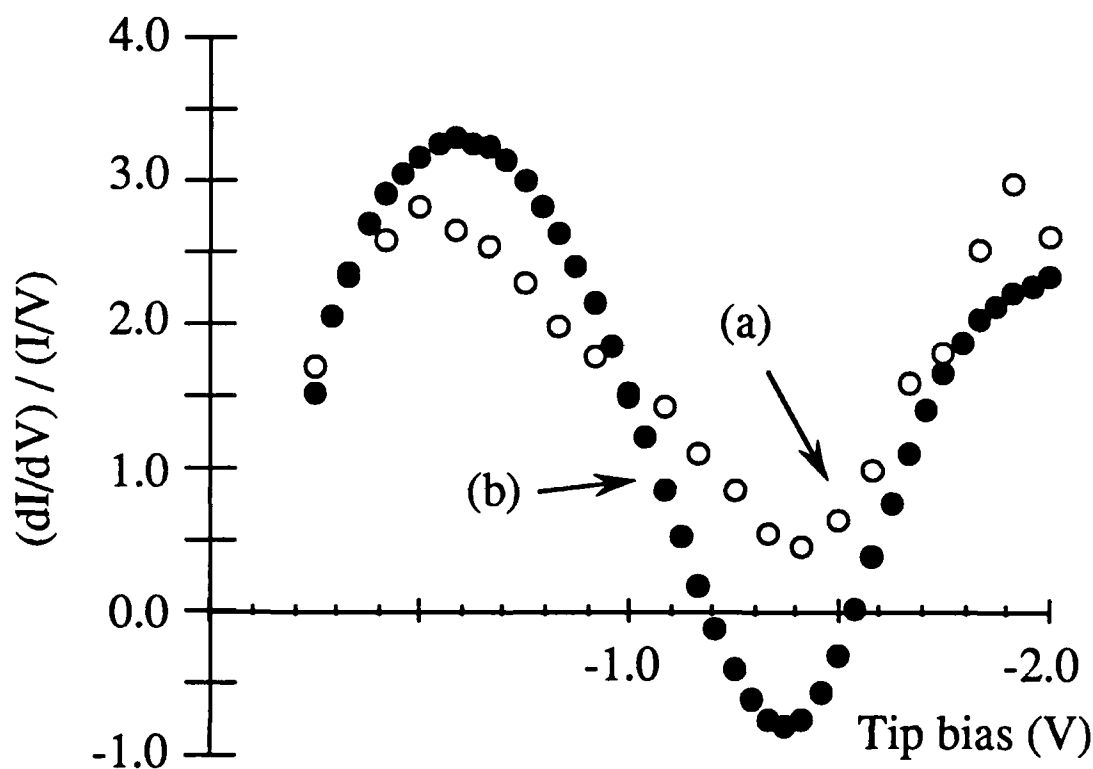


Fig. 5.20: Tunneling spectra acquired with the tip held over (a) contiguous and (b) isolated bright adatom sites on  $\text{Si}(111)\sqrt{3}\times\sqrt{3}\text{R}30^\circ\text{-B}$ , showing the transition to negative differential resistance in case (b) at -1.4V tip bias.



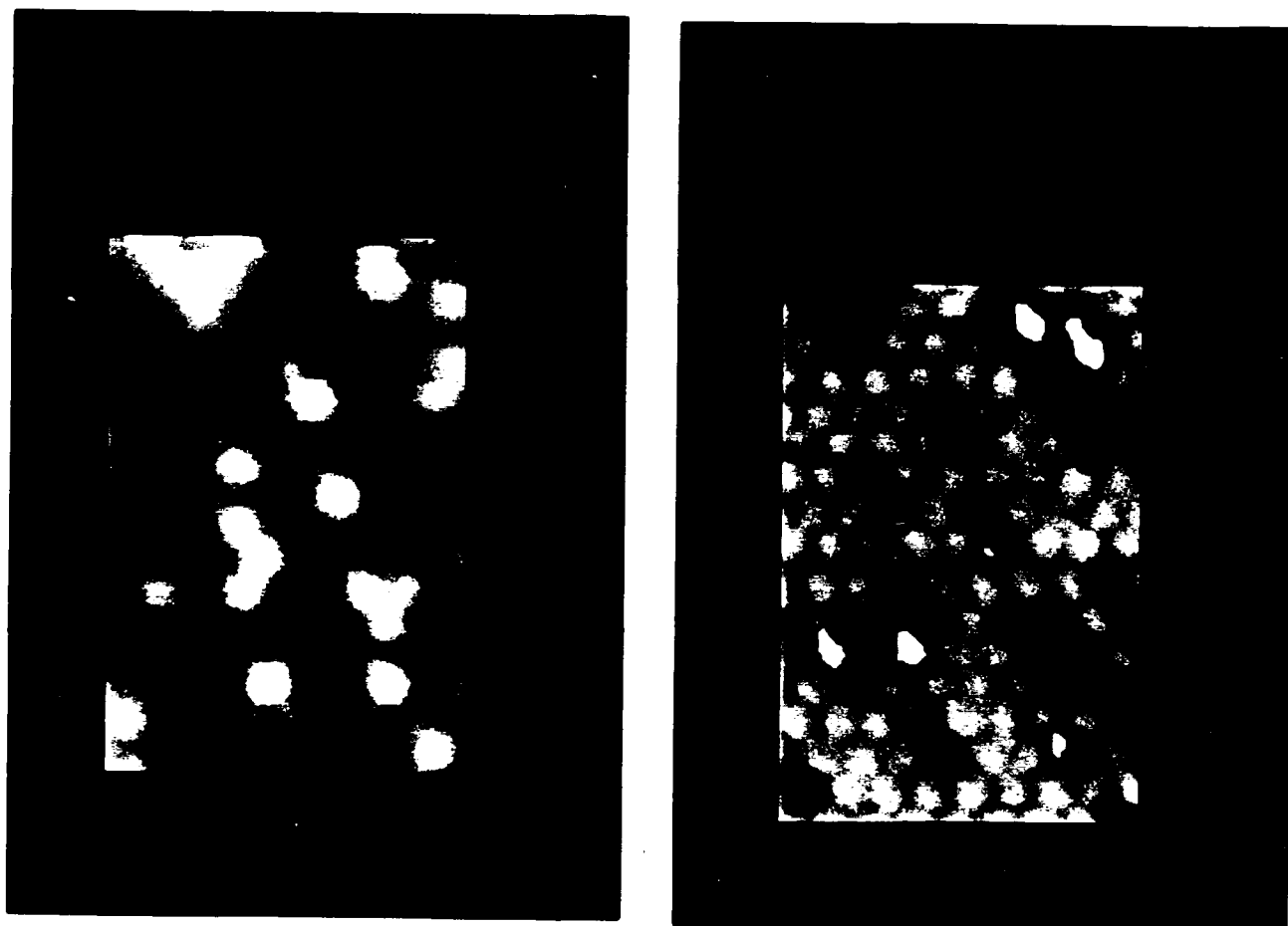


Fig. 5.21 STM topographic image (left) and  $dI/dV$  image (right) showing regions of negative differential conductivity (shaded solid white) at -1.4V tip bias.

## Negative Resistance

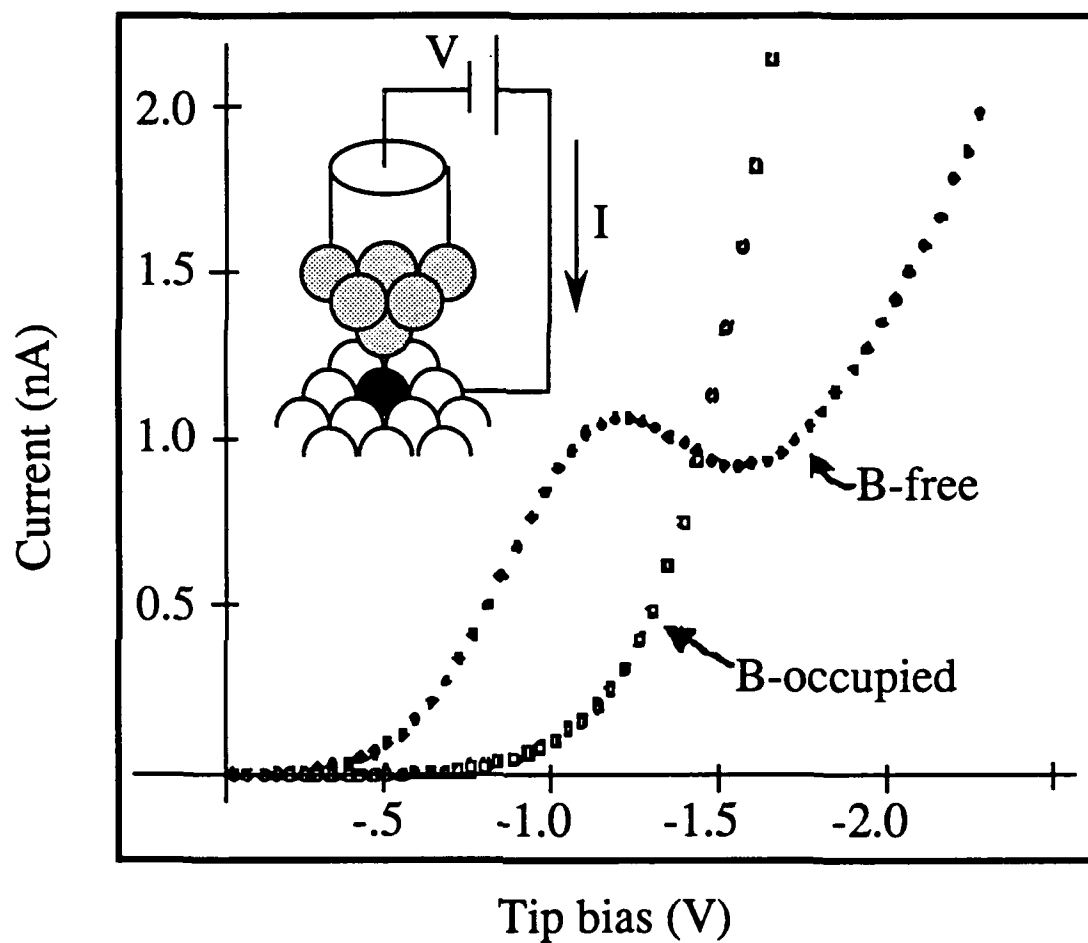


Fig. 5.22: Typical tunnel junction I-V characteristics for a dark, B-occupied site and for an isolated bright, B-free site exhibiting negative differential conductance. The two curves intersect at their common bias point.

solid state device to display and exploit negative differential conductivity, has found wide utility in high-speed electronic applications (Sz81) since its initial report by Esaki in 1958. (Es58) More recently, microfabrication techniques have enabled the realization of resonant tunneling diodes, which also display the conductance anomaly. (Ch74) Our data suggest that a similar atomic-scale version of such a device may be realized under the STM, and we propose that the underlying mechanism in the present case is similar to that of the two preceding, established devices.

In both tunnel diodes and resonant tunneling devices, the onset of negative differential conductivity has been shown to result from a sharp drop in the tunneling probability when the bias reaches an energy level at which tunneling is forbidden. In each case, one electrode, or the barrier, is characterized by a narrow energy level into which tunneling is permitted, and immediately above which is a forbidden band. When the bias on the counter-electrode lines up with the sharp energy level, tunneling can occur with substantial current. When the bias exceeds this point, the most energetic electrons in the counter-electrode cannot tunnel elastically, and those whose energies now line up with the sharp state must overcome a barrier that increases with bias voltage.

Figure 5.23 displays the concept schematically. In the tunnel diode, the narrow, "permitted" state of one electrode is the top of the valence band of a degenerate, p-type semiconductor. Negative differential conductivity appears as the bias passes this level into the band gap, which contains no channel for elastic tunneling. In resonant tunneling devices, tunneling is permitted only into the discretely quantized energy levels in a potential

## Tunnel Devices

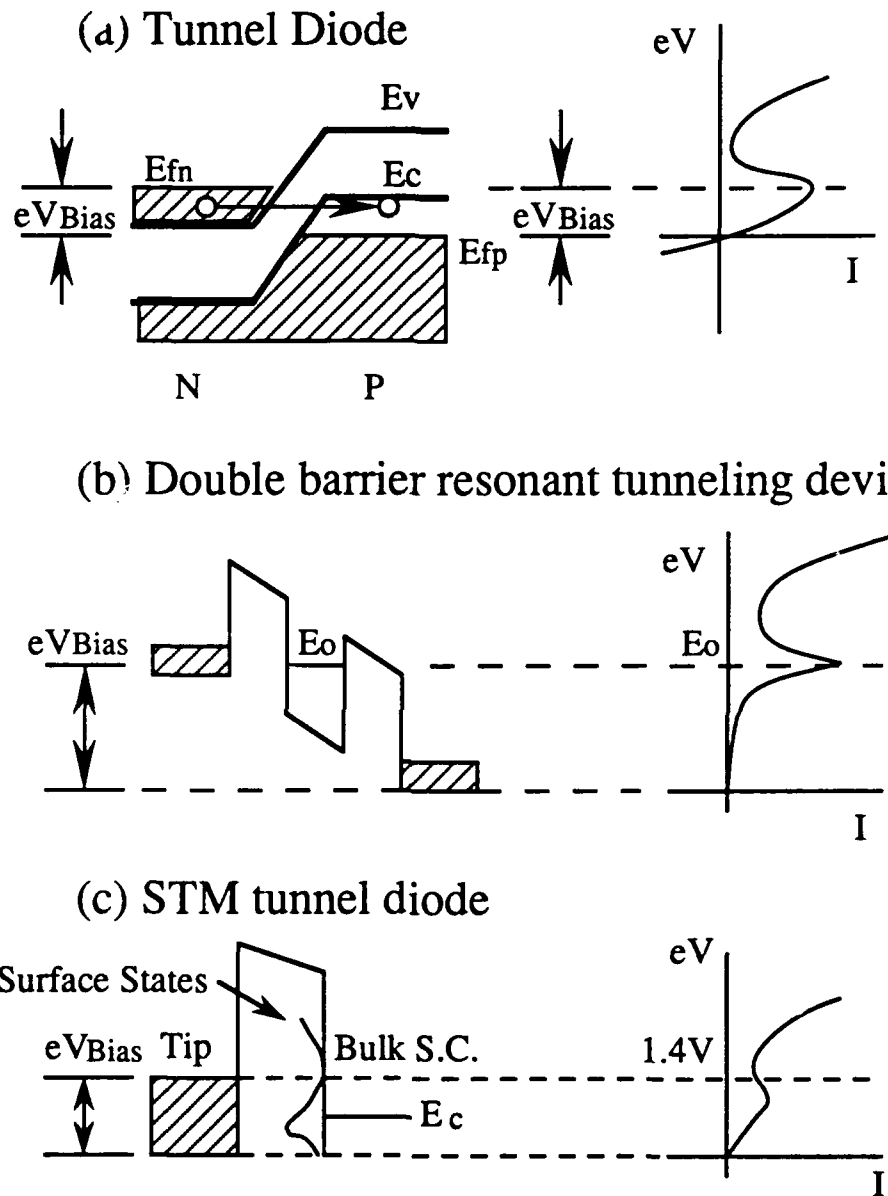


Fig. 5.23: Energy band diagrams illustrating the common principle of devices that exhibit negative differential conductivity. A peak in the junction I-V characteristic occurs when the bias energy of one electrode falls in a narrow range where tunneling is favored. (Sz81, Ch74)

well, so negative differential conductivity occurs when the bias falls between two levels.

Now consider figs. 2.2 and 5.15. We have seen that an unoccupied state localized on the boron-free sites lies within 0.6eV of the fermi level; above this energy, the local density of states on such sites falls off smoothly for 1eV thereafter. Even in the absence of boron, (figs. 5.19a,  $\sqrt{3}\times\sqrt{3}$ R30°, and 2.35, 7×7) the differential conductivity at -1.2 to -1.6V tip bias is low, but non-negative. The lateral isolation of a boron-free site surrounded by boron-occupied positions could be expected to shift and narrow the dispersion of this low-lying state, further reducing the tunneling probability at -1.4V bias and matching the condition for negative differential conductivity. Such sites then act as independent, separate tunnel diodes in concert with the STM's tip. Additional support for the applicability of this picture has come from calculations modeling tip and sample each as a single atom adsorbed on a jellium substrate. Negative differential conductivity was predicted in that case for certain tip biases falling between the perturbed atomic levels of the adsorbate atom. (La86)

#### V.4 Synthesis

In summary, we have identified two types of adatom sites on Si(111) $\sqrt{3}\times\sqrt{3}$ R30°-B according to the presence of a substitutional boron atom directly underneath the adatom. Employing three methods of surface preparation, we have been able to adjust the relative concentration of the two types of sites over a wide range. After associating each site with a distinct, local tunneling spectrum, we have identified the surface states

responsible for differences between the two spectra. The localized nature of these states within atomic dimensions has further enabled the assignment of a distinct I-V characteristic to the tunnel junction according to the tip's placement over one or the other type of site and the local doping environment of the site.

At one of these sites, the observation of negative differential conductivity well above the projected conduction band minimum underscores the surface sensitivity of STM. While the electronic characterization of macroscopic tunnel junctions is dominated by the bulk valence and conduction bands, the atomic-scale tunneling spectra presented above seem to reflect the energy band structure at the surface, with no features that clearly originate from bulk bands. This domination of the tunneling process by surface states seems reasonable in light of the theoretical picture of the adatom dangling orbitals protruding into the vacuum, normal to the surface, (Be89b, Ka89) and KRIPES measurements (Ka89) support the predicted surface state topology. At any rate, a more thorough understanding of carrier transport from surface dangling bond states to the bulk would certainly contribute to the exploitation of surface and interface electronic structure in practical devices.

Turning to the structural observations in this work, we may now address the microscopic causes of the differing macroscopic, physical properties of adsorbed gallium and boron on Si(111), which were presented in §III.2. We have seen that the prediction of different adsorption sites for boron and silicon in the  $\sqrt{3}\times\sqrt{3}R30^\circ$  structure is strongly supported by our spectroscopic and topographic observations. The relative instability of

Si(111) $\sqrt{3}\times\sqrt{3}$ R30°-Ga upon annealing, compared with Si(111) $\sqrt{3}\times\sqrt{3}$ R30°-B, follows from the far lower predicted stress induced by the subsurface substitutional adsorption on the latter surface. The preservation of the buried interface upon epitaxial silicon growth on Si(111) $\sqrt{3}\times\sqrt{3}$ R30°-B, and corresponding disruption when applied to Si(111) $\sqrt{3}\times\sqrt{3}$ R30°-Ga, also follows from this picture because in the former case, a silicon adatom layer is already exposed for further epitaxial growth. Above 1/3 ML local coverage, we have observed initial gallium nucleation that leads to the formation of an ordered overlayer. The same route to nucleation would not be available to boron that initially occupies subsurface sites; thus, we do not observe an analogous ordered overlayer for boron above 1/3 ML.

Finally, we return to that peculiar surface in which the boron-occupied sites were actually in the minority. As shown above, it is possible to prepare a Si(111) $\sqrt{3}\times\sqrt{3}$ R30° surface incorporating up to 80% boron-free sites, where silicon adatoms sit upon a silicon double layer. The fact that clean Si(111) does not normally reconstruct to this periodicity suggests that strong subsurface doping plays a role in the stabilization of this structure. While the  $\sqrt{3}\times\sqrt{3}$ R30° structure completely terminates dangling bonds, the Si(111)7 $\times$ 7 surface has a lower density of adatoms and therefore incorporates dangling bonds on rest atom sites. (§III.2 and fig. 3.1) Charge transfer from adatom dangling bonds to these rest atoms is believed to stabilize this surface relative to the  $\sqrt{3}\times\sqrt{3}$ R30° lattice, which has a lower dangling bond density but does not admit similar charge transfer. (Me89a)

On a surface with substantial subsurface boron accumulation, however, the  $\sqrt{3}\times\sqrt{3}$ R30° structure might be stabilized relative to the 7 $\times$ 7

reconstruction by charge transfer from the adatoms to subsurface acceptor levels. The surfaces prepared by evaporating Si on a boron-terminated wafer sample would have just such a subsurface accumulation in the vicinity of the interface between the original surface and the epi-layer. Eventually, however, arbitrary addition of deep, subsurface dopant would likely turn unfavorable, for the energetic profit of charge transfer saturates with a doping level of one B acceptor per adatom.

A consequence of this picture is that the heavy subsurface acceptor profile should induce a downward movement of the fermi level at the surface. This effect is actually observed in the upward shift by 0.2eV in both the dangling bond state energy on the boron-occupied sites and the corresponding minimum on the boron-free sites from fig. 5.15 to fig. 5.19. Our inability to measure the quantity of deposited silicon precisely in our process prevents a prediction of the magnitude of the energy shift, but the direction of motion in itself indicates that the band-bending effect of a buried interface can be observed by following the position of a particular feature of the surface state spectrum.

With more precise determination and control of the silicon epi-layer thickness and dopant distribution, quantitative prediction of the band bending at a similar surface should be possible. Surface bands might then be "fine-tuned" by adjusting the buried interface. In fact, the stability of boron's B<sub>5</sub> substitutional surface doping described above under both annealing and epitaxial silicon growth presents the possibility "δ-doping" with a single plane of boron atoms.



## VI. Conclusions

### VI.1 Summary

Using a home-made scanning tunneling microscope system, we have investigated the growth of two elemental adsorbates, gallium and boron, on Si(111) at the atomic scale. Our topographical observations of various growth phases assumed by these systems enabled the construction of models of each observed structure that unify previous results from diffraction and interferometric experiments with our own data. Analysis of our local tunneling spectroscopic data, and comparison with available photoemission measurements, further illuminates and supports these models. Moreover, the comparison of both topographic and local tunneling spectroscopic data from one system often reveals specific structural and electronic details that would not otherwise be apparent from consideration of one data set alone. We have also characterized local phenomena that would *not* be observed by a macroscopic, averaging probe. Two dramatic examples of the latter type are random impurity distributions and atomic centers of negative differential conductivity.

Boron and gallium were found to induce different surface structures upon adsorption on Si(111), and the observation of their contrasting behaviors has suggested the relative significance of various competing, microscopic processes that determine adsorption behavior in general. Our observations appear to support recent theoretical formulations of these

processes. Together, the observations and the theoretical picture account for the observed contrast in several physical properties of boron- and gallium-terminated Si(111) surfaces.

For the case of gallium adsorption, we have imaged the  $\sqrt{3}\times\sqrt{3}R30^\circ$  structure characteristic of  $<1/3$  ML coverage, and we have determined the lateral binding site of the adsorbed Ga atom. A complete determination of the Ga position in that structure followed from the combination of results from STM and X-ray standing-wave interferometry. Electronic contributions to tunneling images in this coverage range were found to correlate well with previous band structure measurements, permitting a differentiation of silicon and gallium adatoms.

At higher gallium coverage, we observed an incommensurate superlattice, in which the uppermost layer apparently formed a novel silicon-gallium alloy. While the diffraction patterns for this coverage range had previously been identified, no structure had been proposed, and our findings represented the first real-space observation of an incommensurate superlattice on Si(111). Examination of initial growth stages of the material led to a picture of incommensuration and misfit dislocations that arise as a result of competing electronic and steric forces that drive both a vertical compression and lateral expansion of the surface.

In contrast to the gallium-induced structures, adsorption of boron led to only one surface lattice, of  $\sqrt{3}\times\sqrt{3}R30^\circ$  periodicity. This lattice, however, accommodated a wide range of boron concentrations from as low as 20% up to 95% occupation of available sites. The contrast in atomic sites observed in the tunneling images, according to the presence or absence of a boron atom, enabled straightforward identification of boron-occupied sites

throughout the available surface doping range. While differing from data for the  $\text{Si}(111)\sqrt{3}\times\sqrt{3}\text{R}30^\circ\text{-Ga}$  surface, the spectroscopic and topographic data on  $\text{Si}(111)\sqrt{3}\times\sqrt{3}\text{R}30^\circ\text{-B}$  together were consistent with the predicted consequences of boron occupation of a site directly underneath the observed adatom. Our observations therefore corroborate the conceptual foundations of the surface energy and stress calculations in this case. Moreover, the subsurface substitutional boron occupation, and the relative stability of that structure over the Ga-adatom termination, together account qualitatively for several gross physical properties, such as desorption temperature and epitaxial behavior, that are known to distinguish the two surfaces dramatically.

We note that the appearance of a  $\sqrt{3}\times\sqrt{3}\text{R}30^\circ$  adatom-covered surface consisting primarily of silicon adatoms on a silicon substrate is a novel structure in itself. Both our electronic observations and sample preparation method are consistent with a picture for the stabilization of this surface by substantial boron doping at a buried interface, suggesting that a reconstruction may be altered by electronic forces that derive from a particular bulk doping profile.

Finally, we have reported the occurrence of negative differential conductivity in the tunnel junctions's I-V characteristic at particular atomic binding sites on  $\text{Si}(111)\sqrt{3}\times\sqrt{3}\text{R}30^\circ\text{-B}$ , and we identified the surface electronic characteristics responsible for the conductance anomaly on the basis of local tunneling spectra. This observation signifies the exploration of a new realm where an entirely microscopic phenomenon, here the occurrence of the anomaly on isolated sites of atomic dimensions, is not associated with a gross property or average observable of the surface. With the conviction that this realm will one day lie open for practical

exploitation, we do not hesitate to borrow the terms "device" and "tunnel-diode" from our familiar laboratory vocabulary to characterize the conductance anomaly in the STM.

## VI.2 Outlook

The dramatically contrasting adsorption behaviors observed for Ga and B, two chemically related elements, on the Si(111) surface alone suggests the richness of new materials that may be found to exist at surfaces and interfaces on systems as yet unexplored. In view of the promising correspondence of our observations with energy and stress computations, which identify the competing microscopic interactions that determine surface structure, it is not unreasonable to speculate that new surface structures and the conditions for their formation may soon be predictable. A "science" of interface formation at the atomic level will then support the "art" of epitaxy.

We have found a close interdependence of surface morphology and mid-gap band structure. Consequently, it will be possible to change the electronic properties of a surface by changing its reconstruction. The purposeful modification of a reconstruction with the introduction of surface stress has been observed in this work and previously, (Go85b) and has been predicted theoretically. (Va87a) Our finding that a reconstruction may be stabilized by the electronic influence of a buried interface suggests doping as a second means of altering surface structure. This second approach offers the possibility of smooth adjustment of surface bands by controlling the subsurface doping profile. Modification of the reconstruction alone, for example by stress introduction, would introduce only discrete changes in the surface band structure.

We have indicated the strong sensitivity of local tunneling spectroscopy to surface bands. A more thorough understanding of carrier transport at semiconductor surfaces is required if the measured I-V characteristics of the tunnel junction are to be understood and exploited practically. We have also seen that the uncontrollability of the tip hinders many useful measurements; thus, an ability to characterize, if not to control, the tip structure continuously would represent a significant contribution to STM technology.

Surely the more far-reaching suggestion of our observations is that some utility would accompany the development of a capability for systematic alteration of the semiconductor surfaces on the atomic scale. Techniques for the producing, pinning, or eliminating misfit dislocations, of the type we have observed on the gallium overlayer structure, would substantially extend the selection of materials available for heteroepitaxial growth. We have also demonstrated that the distribution of surface dopant atoms leads to measurable, local electronic consequences. The actual local dopant distribution, though a product of random processes, could still be determined and selected. When combined with the recently demonstrated ability to position individual atoms on a surface, (Be87) both the redistribution of misfit dislocations through local adsorbate nucleation and coverage, observed in gallium adsorption, and the isolation of device characteristics to individual surface atoms, prominently observed in boron adsorption, represent important steps towards the development of practical, atomic-scale electronics.

## Appendix

### Chemical Sample Preparation

Samples were initially cut under a diamond saw from wafers waxed to a stainless steel slab. The wax was then removed from the cut sample with the appropriate solvent, generally methanol. Degreasing was accomplished with 5 min. of ultrasonic agitation in trichloroethylene, acetone, and warm methanol, which was removed under clean nitrogen flow.

The Shiraki etch (Is82) below was applied to each sample immediately preceding placement in the vacuum chamber. Samples could be reused, but a new chemical treatment accompanied each replacement in vacuum. The principle of the preparation is the removal of the native oxide from the polished face of the wafer and replacement with a controlled oxide layer that would protect the surface through the bakeout. After a thorough outgassing in vacuum, the 7×7 reconstruction could then be obtained simply by removing the oxide with an 1100°C annealing.

Recipe:

Trichloroethylene	75°C	3-5 min.
Acetone	RT	1 min.
Methanol	RT	1 min.
3 × DI H <sub>2</sub> O		
H <sub>2</sub> O:NH <sub>4</sub> OH:H <sub>2</sub> O <sub>2</sub> 4:1:1	80° C	5 min.
3 × DI H <sub>2</sub> O		

At least 2 repetitions of the following cycle:

{		
H <sub>2</sub> O:HF 1:1	RT	30 sec.
3 × DI H <sub>2</sub> O		
H <sub>2</sub> O:H <sub>2</sub> O <sub>2</sub> :HCl 5:1:1	30° C	5 min.
3 × DI H <sub>2</sub> O		
}		
H <sub>2</sub> O:HF 1:1	RT	30 sec.
H <sub>2</sub> O:H <sub>2</sub> O <sub>2</sub> :HCl 1:1:3	90-100° C	10 min.

## References

- Av87 J. Avigad, Documentation for SCAN program, in the file "Scandocs.txt."
- Ba61 J. Bardeen, Phys. Rev. Lett. **6**, 57 (1961).
- Be85a R. S. Becker, J. A. Golovchenko, B. S. Swartzentruber, Phys. Rev. Lett. **55**, 987 (1985).
- Be85b R. S. Becker, J. A. Golovchenko, E. G. McRae, and B. S. Swartzentruber, Phys. Rev. Lett. **55**, 2028 (1985).
- Be85c R. S. Becker, J. A. Golovchenko, D. R. Hamann, B. S. Swartzentruber, Phys. Rev. Lett. **55**, 2032 (1985).
- Be86 R. S. Becker, J. A. Golovchenko, G. S. Higashi, B. S. Swartzentruber, Phys. Rev. Lett. **57**, 1020 (1986).
- Be87 R. S. Becker, J. A. Golovchenko, B. S. Swartzentruber, Nature **325**, 419 (1987).
- Be88 R. S. Becker, B. S. Swartzentruber, J. S. Vickers, M. S. Hybertsen, S. G. Louie, Phys. Rev. Lett **60**, 116 (1988).
- Be89a R. S. Becker, B. S. Swartzentruber, J. S. Vickers, T. Klitsner, Phys. Rev. B **39**, 1633 (1989).
- Be89b P. Bedrossian, R. Meade, K. Mortensen, D. M. Chen, J. A. Golovchenko, D. Vanderbilt, Phys. Rev. Lett. **63**, 1257 (1989).
- Be89c P. Bedrossian, K. Mortensen, D. M. Chen, J. A. Golovchenko, Submitted for publication.



- Bi83 G. Binnig, H. Rohrer, C. Gerber, E. Weibel, Phys. Rev. Lett **50**, 120 (1983).
- Bi86 G. Binnig and H. Rohrer, IBM J. Res. Develop. **30**, 355 (1986).
- Bi87 G. Binnig and H. Rohrer, Rev. Mod. Phys. **59**, 615 (1987).
- Ch74 L. L. Chang, L. Esaki, and R. Tsu, Appl. Phys. Lett. **24**, 593 (1974).
- Ch88 D. Chen, J. Golovchenko, P. Bedrossian, and K. Mortensen, Phys. Rev. Lett. **61**, 2867 (1988).
- Co82 S. N. Coppersmith, D. S. Fisher, B. I. Halperin, P. A. Lee, W. F. Brinkman, Phys. Rev. B **25**, 349 (1982).
- Co85 R. V. Coleman, B. Drake, P. K. Hansma, G. Slough, Phys. Rev. Lett. **55**, 394 (1985).
- Da76 L. E. Davis, N. C. MacDonald, P. W. Palmberg, G. E. Riach, R. E. Wever, *Handbook of Auger Electron Spectroscopy* (Physical Electronics Ind. Inc., Eden Prairie, MN, 1976).
- Es58 L. Esaki, Phys. Rev. **109**, 603 (1958).
- Fe86 L. C. Feldman and J. W. Mayer, *Fundamentals of Surface and Thin Film Analysis* (North Holland, N.Y., 1986), pp. 305-7.
- Fe87 R. M. Feenstra, J. A. Stroscio, A. P. Fein, Surf. Sci. **181**, 295 (1987).
- Go74 J. A. Golovchenko, B. W. Batterman, W. L. Brown, Phys. Rev. B **10**, 4239 (1974).
- Go85a J. A. Golovchenko, Bull. Am. Phys. Soc. **30**, 251 (1985).
- Go85b H.-J. Gossmann, J. C. Bean, L. C. Feldman, E. G. McRae, I. K. Robinson, Phys. Rev. Lett. **55**, 1106 (1985).
- Go86 J. A. Golovchenko, Science **232**, 48 (1986).

- Ha86 R. J. Hamers, R. M. Tromp, J. E. Demuth, Phys. Rev. Lett. **56**, 1972 (1986).
- Ha87 P. K. Hansma and J. Tersoff, J. Appl. Phys. **61**, R1 (1987).
- Ha88a R. J. Hamers and J. E. Demuth, J. Vac. Sci. Technol. A **6**, 512 (1988).
- Ha88b R. J. Hamers and J. E. Demuth, Phys. Rev. Lett. **60**, 2527 (1988).
- Ha88c R. J. Hamers, J. Vac. Sci. Technol. B **6**, 1462 (1988).
- He89 R. L. Headrick, L. C. Feldman, I. K. Robinson, Appl. Phys. Lett. **55**, 442 (1989).
- Hi88 H. Hirayama, T. Tatsumi, N. Aizaki, Surf. Sci. **193**, L47 (1988).
- Ho87 H. Hong, C. J. Peters, A. Mak, R. B. Birgeneau, P. M. Horn, H. Suematsu, Phys. Rev. B **36**, 7311 (1987).
- Is82 A. Ishizaka, N. Nakagawa, Y. Shiraki, in Proceedings of the Second International Symposium on Molecular Beam Epitaxy and Related Clean Surface Techniques (Japan Society of Applied Physics, Tokyo 1982), p. 182.
- Ka87 A. Kawazu, I. Yokohama, H. Suzuki, A. Ohsaki, K. Takeuchi, H. Sakama, Phys. Rev. B **36**, 9809 (1987).
- Ka88 A. Kawazu and H. Sakama, Phys. Rev. B **37**, 2704 (1988).
- Ka89 E. Kaxiras, K. Pandey, F. Himpsel, R. Tromp, submitted for publication.
- Ki86 C. Kittel, *Introduction to Solid State Physics* (Wiley, N.Y., 1986), chapter 19.
- Kl89 T. Klitsner, R. S. Becker, J. S. Vickers, Submitted for publication.

- Ko88a V. V. Korobtsov, V. G. Lifshits, A. V. Zotov, *Surf. Sci.* **195**, 466 (1988).
- Ko88b U. K. Kohler, J. E. Demuth, R. J. Hamers, *Phys. Rev. Lett.* **60**, 2499 (1988).
- Ku89 Y. Kuk and P. J. Silverman, *Rev. Sci. Instrum.* **60**, 165 (1989).
- La63 J. J. Lander and J. Morrison, *J. Appl. Phys.* **34**, 1403 (1963).
- La64 J. J. Lander and J. Morrison, *Surf. Sci.* **2**, 553 (1964).
- La86 N. D. Lang, *Phys. Rev. B* **34**, 5947 (1986).
- Ma75 B. Mahan, *University Chemistry* (Addison Wesley, Reading, MA, 1975), p. 580.
- Me88 R. D. Meade and D. Vanderbilt, in press.
- Me89a R. D. Meade and D. Vanderbilt, *Phys. Rev. B* **40**, 3905 (1989).
- Me89b R. D. Meade and D. Vanderbilt, submitted for publication.
- Mi87 H. A. Mizes, S. Park, W. Harrison, *Phys. Rev. B* **35**, 4491 (1987).
- Mu69 E. W. Müller and T. T. Tsong, *Field Ion Microscopy* (American Elsevier, N.Y., 1969), pp. 118-134.
- Mu89 J. E. Müller, W. Daum, H. Ibach, *Phys. Rev. Lett.* **62**, 2423 (1989).
- Ni85a J. M. Nicholls, P. Mårtensson, G. V. Hansson, J. E. Northrup, *Phys. Rev. B* **32**, 1333 (1985).
- Ni85b O. H. Nielsen and R. M. Martin, *Phys. Rev. B* **32**, 3792 (1985).
- Ni87a J. M. Nicholls, B. Reihl, and J. E. Northrup, *Phys. Rev. B* **35**, 4137 (1987).
- Ni87b J. M. Nicholls and B. Reihl, *Phys. Rev. B* **36**, 8071 (1987).
- No84 J. E. Northrup, *Phys. Rev. Lett.* **53**, 683 (1984).

- No86 J. E. Northrup, Phys. Rev. Lett. **57**, 154 (1986).
- No87 J. Nogami, S. Park, C. F. Quate, Phys Rev. B **36**, 6221 (1987).
- No88 J. Nogami, S. Park, C. F. Quate, Surf. Sci. **203**, L631 (1988).
- Ot85 M. Otsuka and T. Ichikawa, Jpn. J. Appl. Phys. **24**, 1103 (1985).
- Pa86 J. R. Patel, P. E. Freeland, J. A. Golovchenko, A. R. Kortan, D. J. Chadi, G. Qian, Phys. Rev. Lett. **57**, 3077 (1986).
- Pa87a S. Park, J. Nogami, C. F. Quate, Phys. Rev. B **36**, 2863 (1987).
- Fa87b S. Park and C. F. Quate, Rev. Sci. Instrum. **58**, 2010 (1987).
- Pa88 S. Park, J. Nogami, H. Mizes, C. F. Quate, Phys. Rev. B **38**, 4269 (1988).
- Pa89 M. C. Payne, N. Roberts, R. J. Needs, M. Needels, J. D. Joannopoulos, Surf. Sci. **211/212**,1 (1989).
- Pi87 D. Pinkowitz, Electronic Products, 15 June 1987, p. 61.
- Qu86 C. F. Quate, Phys. Today, August, 1986, p. 26.
- Ro88 I. K. Robinson, W. K. Waskiewicz, P. H. Fuoss, L. J. Norton, Phys. Rev. B **37**, 4325 (1988).
- Sl86 C. G. Slough, W. W. McNairy, R. V. Coleman, B. Drake, P. K. Hansma, Phys. Rev. B **34**, 994 (1986).
- St84 P. W. Stephens et. al., Phys. Rev. B **29**, 3512 (1984).
- St88 J. S. Strosio, R. M. Feenstra, D. M. News, A. P. Fein, J. Vac. Sci. Technol A **6**, 499 (1988).
- Sz81 S. M. Sze, *The Physics of Semiconductor Devices* (Wiley, N.Y., 1981), Chapter 9.
- Ta85 K. Takayanagi, Y. Tanishiro, M. Takahashi, S. Takahashi, J. Vac. Sci, Technol. A **3**, 1502 (1985).

- Th89 F. Thibaudau, Ph. Dumas, Ph. Mathiez, A. Humbert, D. Satti, F. Salvan, *Surf. Sci.* **211/212**, 148 (1989).
- To88 St. Tosch and H. Neddermeyer, *Phys. Rev. Lett.* **61**, 349 (1988).
- Tr85 R. M. Tromp, R. J. Hamers, J. E. Demuth, *Phys. Rev. Lett.* **55**, 1303 (1985).
- Tr86 R. M. Tromp, R. J. Hamers, J. E. Demuth, *Science* **234**, 304 (1986).
- Tr88 R. Tromp, E. van Loenen, J. Demuth, N. Lang, *Phys. Rev. B* **37**, 9042 (1988).
- Uh85 R. I. Uhrberg, G. B. Hansson, J. M. Nicholls, P. E. Persson, S. A. Flodström, *Phys. Rev. B* **31**, 3805.
- Va87a D. Vanderbilt, *Phys. Rev. Lett.* **59**, 1456 (1987).
- Va87b D. Vanderbilt, *Phys. Rev. B* **36**, 6209 (1987).
- Va88 D. Vanderbilt, in *The Structure of Surfaces II*, J. F. van der Veen and M. A. van Hove, eds. (Springer, N.Y., 1988), p. 276.
- We79 G. L. Weissler and R. W. Carlson, ed., *Vacuum Physics and Technology* (Academic Press, N.Y., 1979).
- Wi87 R. J. Wilson and S. Chiang, *Phys. Rev. Lett.* **59**, 2329 (1987).
- Yo71 R. Young, *Phys. Today* **24**, 42 (1971).
- Za88 A. Zangwill, *Physics at Surfaces* (Cambridge University Press, Cambridge, 1988), chapter 3 and pp. 91-104.
- Ze88 J. Zegenhagen, J. S. Hybertsen, P. E. Freeland, J. R. Patel, *Phys. Rev. B* **38**, 7885 (1988).
- Ze89 J. Zegenhagen, J. R. Patel, P. Freeland, D. M. Chen, J. A. Golovchenko, P. Bedrossian, J. E. Northrup, *Phys. Rev. B* **39**, 1298 (1989).

- Zi87a M. Zinke-Allmang, L. C. Feldman, S. Nakahara, Appl. Phys. Lett. **51**, 975 (1987).
- Zi87b M. Zinke-Allmang and L. C. Feldman, Surf. Sci. **191**, L749 (1987).
- Zi88a M. Zinke-Allmang, L. C. Feldman, S. Nakahara, Appl. Phys. Lett. **52**, 144 (1988).
- Zi88b M. Zinke-Allmang, L. C. Feldman, S. Nakahara, J. R. Patel, in *Epitaxy of Semiconductor Layered Structures*, edited by R. T. Tung, R. Dawson, and R. L. Gunshor, Mat. Res. Soc. Symp. Proc. **102**, 431 (1988).

## Acknowledgments

Though this author has had the privilege of recording the experiments described in this work, the STM program at Harvard is a product of indispensable contributions from many individuals. The following people played vital roles in this particular work.

Drs. Dongmin Chen, Jene Golovchenko, and Paul Horowitz supervised various aspects of the project, and the author worked closely with each. Their insights are found on every preceding page of this manuscript.

It was a pleasure to collaborate with the two other people in our lab. Jeremy Avigad produced a professional *and* friendly STM control program and also clever ideas for interfacing and instrumentation. Klaus Mortensen was a tireless confrere through many late nights of both data taking and vacuum/STM repair operations.

Much of the theoretical work referenced above was contributed by Bob Meade and David Vanderbilt, who always delighted in tackling large computations that illuminated our experimental results. Discussions with Dr. Franz Himpsel of IBM also proved invaluable.

Cliff Colby and Don Rogers of the Rowland Institute rapidly produced the finest STM replacement parts in the world on short order, while managing to keep up with our evolving specs.

Winfield Hill provided invaluable assistance with electronic matters, and Jon Segal produced software modifications on the fly. R. S. Becker and J. Vickers of AT&T Bell Laboratories generously donated software for the IRIS processor, with which the photographs in this work were all produced.

Pierre Crevoiserat, Chris Cyders, and Ralph Stanley of Jefferson Lab offered helpful advice on mechanical and electrical construction.

Mike Burns of the Rowland Institute provided the author with the software and helpful suggestions for preparing this manuscript on the Apple Macintosh. The text was written with Microsoft Word. Drawings were either prepared directly in MacDraw II or digitized by a Microtek Scanner and processed by Silicon Beach's Digital Darkroom and Superpaint. Certain graphs were prepared with the Abelbeck Kaleidagraph package.

The experiments described above were supported by the U.S. Office of Naval Research under Grant No. N00014-87-K-0511. The author was also supported under a National Science Foundation Graduate Fellowship.